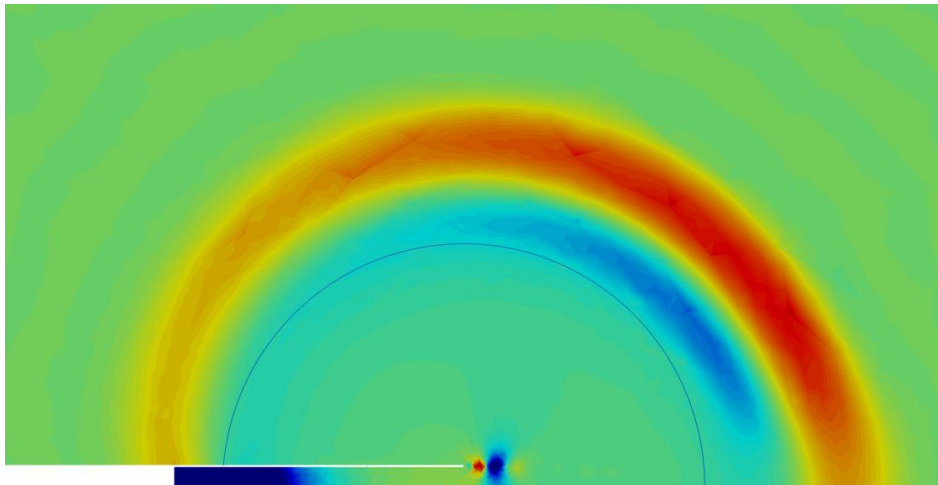


Drasko Masovic

Sound Radiation from an Open Pipe  
with a Mean Flow





# Sound Radiation from an Open Pipe with a Mean Flow

Dissertation by

**Drasko Masovic**

For the Degree  
Doktor der Naturwissenschaften

Committee:

Univ.Prof. Robert Höldrich, Chair (IEM, KU Graz)

Univ.Prof. Gerhard Eckel (IEM, KU Graz)

Priv.-Doz. Anton Fuchs (ViF, KU Graz)



Institute of Electronic Music and Acoustics  
University of Music and Performing Arts, Graz, Austria  
August 2017



# ABSTRACT

This work considers analytical and numerical approaches for estimation of sound radiation from an open pipe with a mean flow of fluid. It deals with the identification, characterisation, and assessment of the main flow and acoustic phenomena which influence sound propagation and the resulting far acoustic field outside the pipe. The analysis is focused on the case of low frequency (Helmholtz number) of the emitted sound and low Mach number of a subsonic jet, issued from a straight circular pipe with a sharp trailing edge at the opening. This allows a simpler theoretical treatment of the vortex-sound interaction at the edge of the pipe and the assessment of refraction of the sound wave inside the moving inhomogeneous medium introduced by the jet. The described procedures are aimed to be used primarily for automotive and musical applications, in which sound radiation can be appreciably affected by the mean flow of gas inside pipes. From the theoretical aspect, different sets of acoustic propagation equations and single-unknown wave equations are discussed in connection with more general equations of fluid dynamics. As a step towards more complex geometries and flows which are expected to occur in practice, several possible approaches for a numerical solution of the problem are investigated, based on the combination of acoustic solvers and computational fluid dynamics. Both theoretical and numerical results are validated through the comparison with the results obtained from the laboratory measurements. Ultimately, the thesis should provide an interpretation of the main physical phenomena which affect the far-field sound radiation from a pipe with a hot mean flow and point to the possible methods with which the sound field can be calculated in practice.



# KURZFASSUNG

Diese Arbeit betrachtet analytische und numerische Ansätze zur Abschätzung der Schallabstrahlung aus einem offenen Rohr mit Gasströmung. Sie befasst sich mit der Identifikation, Charakterisierung und Bewertung der wichtigsten Strömungs- und akustischen Phänomene, die die Schallausbreitung und das daraus resultierende akustische Fernfeld außerhalb des Rohres beeinflussen. Die Analyse konzentriert sich auf den tieffrequenten Fall (niedere Helmholtz-Nummer) des emittierten Schalls mit kleiner Mach-Zahl der subsonischen Strömung (Jet), die aus einem geraden Kreisrohr mit einer scharfen Hinterkante an der Öffnung austritt. Das ermöglicht eine einfachere theoretische Behandlung der Wirbel-Schall-Interaktion an der Kante und der Brechung der Schallwelle innerhalb des sich bewegenden inhomogenen Mediums, das durch den Jet eingeführt ist. Die beschriebenen Verfahren zielen darauf ab, vor allem für Automobil- und Musikanwendungen eingesetzt zu werden, bei denen die Schallabstrahlung durch die Strömung im Rohr erheblich beeinflusst werden kann. Aus der theoretischen Perspektive sind verschiedene Systeme der akustischen Ausbreitungsgleichungen und verwandter Wellengleichungen im Zusammenhang mit den allgemeineren Gleichungen der Fluidodynamik diskutiert. Als ein Schritt hin zu komplexeren Geometrien und Strömungen, die in der Praxis zu erwarten sind, werden mehrere mögliche Ansätze zur numerischen Lösung des Problems untersucht, die auf der Kombination von akustischen Solvern und Verfahren der numerischen Strömungsdynamik basieren. Sowohl theoretische als auch numerische Ergebnisse werden validiert durch den Vergleich mit den Ergebnissen von Labormessungen. Letztlich soll die Arbeit eine Erklärung der wichtigsten physikalischen Phänomene liefern, die die Fernfeldschallabstrahlung aus einem Rohr mit heißer Strömung beeinflussen, und auf mögliche Methoden hinweisen, mit denen das resultierende Schallfeld in der Praxis berechnet werden kann.



# ACKNOWLEDGEMENTS

Above all, I am grateful to my supervisors, Eugene Nijman and Dr. Jan Rejlek from the Virtual Vehicle Research Center (ViF) in Graz and Prof. Robert Höldrich from the Institute of Electronic Music and Acoustics (IEM), KU Graz. Their unreserved support since they gave me the opportunity to work in this exciting field, patience, and unselfishness in sharing their expertise were my driver throughout the research and the essential help, which ultimately lead to finishing the thesis. I can hardly thank them enough.

I would also like to thank Dr. Anton Fuchs, head of the NVH and Friction Area (ViF), Martin Wifling (ViF), the coordinator of the international “BATWOMAN” project, my colleagues, young researchers on the project, and their supervisors, with all of whom I had a great and inspiring time at every meeting.

Many thanks to Dr. Franz Zotter (IEM, KU Graz) for interesting talks, friendly and valuable suggestions during my work, as well as to Markus Polanz, Antonio Acri, Vittorio D’Ortona, Dr. Giorgio Veronesi, Rafael Veloso, Yasser Elnemr, and other colleagues from the NVH Group of Virtual Vehicle. It was a privilege to collaborate with all these young experts.

I am very grateful to Andreas Domaingo (ViF), for his indispensable help with (computational) fluid dynamics.

My deep thanks and appreciation go to Prof. Avraham Mico Hirschberg and Dr. Sjoerd Rienstra (TU Eindhoven), Prof. Manfred Kaltenbacher (TU Vienna), and Dr. Hadrien Beriot (Siemens PLM Software) for several fruitful discussions in the critical times for my research.

Special thanks to my wife Eva for her enormous tolerance and support in the last years. Together with our families, it has been a true joy...

The research work of Drasko Masovic has been funded by the European Commission within the ITN Marie Curie Action project BATWOMAN under the 7<sup>th</sup> Framework Programme (EC grant agreement no. 605867). The author acknowledges the financial support of the COMET K2 – Competence Centres for Excellent Technologies Programme of the Austrian Federal Ministry for Transport, Innovation and Technology (BMVIT), the Austrian Federal Ministry of Science, Research and Economy (BMWFW), the Austrian Research Promotion Agency (FFG), the Province of Styria and the Styrian Business Promotion Agency (SFG).

# Contents

<b>ABSTRACT</b> .....	iii
<b>KURZFASSUNG</b> .....	v
<b>ACKNOWLEDGEMENTS</b> .....	vii
<b>I INTRODUCTION</b> .....	3
1.1 Mean flow and sound wave properties .....	4
1.2 Organization of contents .....	6
<b>II EQUATIONS OF FLUID DYNAMICS AND ACOUSTICS</b> .....	9
2.1 Navier-Stokes equations .....	9
2.2 Steady flow .....	16
2.3 Reynolds-averaged Navier-Stokes equations .....	17
2.4 Linearized Euler Equations.....	20
2.5 Wave equation and convected wave equation .....	28
2.6 Aeroacoustic analogies .....	32
2.6.1 Lighthill's equation.....	32
2.6.2 Phillips' equation .....	35
2.6.3 Ffowcs Williams and Hawkins equation .....	38
2.7 Analytical solutions of sound radiation from an open pipe .....	42
<b>III LABORATORY MEASUREMENTS OF THE FAR-FIELD RADIATION PATTERN</b> .....	45
3.1 Measurement setup .....	45
3.2 Signal processing .....	50
3.3 Results.....	52
3.3.1 No-flow case .....	53
3.3.2 Mean flow velocity effects.....	56
3.3.3 Temperature effects .....	58
3.3.4 Frequency effects .....	61
3.4 Discussion .....	63

<b>IV SIMPLE MODEL OF THE FAR-FIELD RADIATION.....</b>	<b>67</b>
4.1 Incident sound.....	68
4.2 Vortex-sound interaction .....	70
4.3 Refraction.....	75
4.4 Estimation of the far-field radiation.....	78
<b>V EQUATION FOR A BODY IN AN INHOMOGENEOUS FLOW .....</b>	<b>85</b>
5.1 Derivation of the equation .....	86
5.2 A simple example of a point dipole in a non-uniform hot flow.....	89
5.3 Discussion .....	91
<b>VI NUMERICAL ESTIMATION OF THE SOUND FIELD.....</b>	<b>93</b>
6.1 Computational fluid dynamics .....	97
6.1.1 Calculations setup .....	97
6.1.2 Results.....	100
6.2 Computational acoustics .....	101
6.2.1 Solution of Linearized Euler Equations.....	102
6.2.2 Solution of convected wave equation .....	106
<b>VII CONCLUSIONS AND OUTLOOK.....</b>	<b>115</b>
<b>REFERENCES.....</b>	<b>119</b>

# Chapter I

## INTRODUCTION

Open pipe which exhausts a flow of hot or cold gas acts as a source of sound in many different circumstances. In such cases, the opening of the pipe is commonly regarded as an apparent sound source as observed by a potential listener in the exterior. The actual source of sound (which might be the source of the main flow, as well) is located inside the pipe, or inside more complex machinery which terminates with the pipe section. With regard to that, the main field of applications which is in the focus of this work are exhaust pipes in vehicles, such as tail-pipes of the exhaust systems, and outlets of HVAC (heating, ventilation, and air conditioning) systems, which are common in automotive industry. Apart from this, within the limitation of low mean flow velocities and temperatures of the flow close to the ambient value, the results of the research can also be applied in the context of musical acoustics, for the characterisation of wind instruments. In other words, the study should be relevant whenever the mean flow of the emitted gas affects appreciably the far-field sound propagation outside the pipe. Regardless of the character of the actual sound source inside the pipe or whether the generated sound presents an unwanted noise, which is typical in automotive applications, or a musical tone, the presented analytical and numerical procedures and the results derived with their implementation can be used for the estimation of sound propagation and the resulting far field. Particular applications may include the estimation of vehicle pass-by noise, excitation of the vehicle's body due to the noise coming from the exhaust system (for further prediction of the interior sound), as well as the directivity properties of wind instruments, for example, for prediction of sound fields in rooms for musical performances or spatial sound synthesis.

The majority of the work is concerned with an idealized case study, as depicted in Figure 1.1. The entire geometry of the case is axisymmetric. A straight circular pipe emits both steady mean flow in the form of a jet and an acoustic wave into the otherwise cold (say, at room temperature) and still environment. The pipe terminates with a simple straight-cut opening at one end and extends to infinity at the other end,

so that the interior of the pipe, apart from close to the opening, has no effect on either the mean flow or the sound radiation. The wall of the pipe is very thin and smooth and the pipe is unflanged, so that the trailing edge of the pipe at the opening is sharp. Nevertheless, the wall is considered to be rigid and non-vibrating, so only airborne acoustic phenomena are treated, while all fluid-structure interaction effects and vibrations of the solid body can be neglected. Taking into account the aimed applications, the study is limited to low Mach number values of the subsonic flow of cold or hot gas, and relatively low frequencies of the emitted sound.

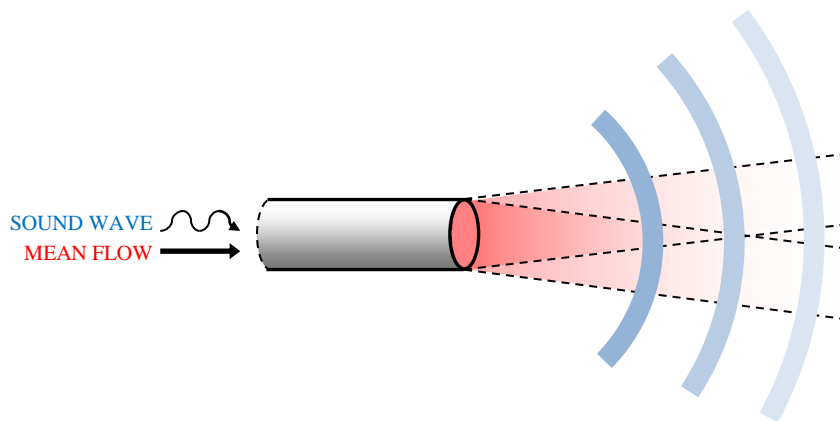


**Figure 1.1:** Sound radiation from a semi-infinite circular pipe with a mean flow.

## 1.1 Mean flow and sound wave properties

The analysis is concerned with low (below 0.3) Mach number values of the mean flow, where Mach number represents the ratio of the local mean flow ( $U$ ) and sound ( $c$ ) speeds:  $M = U/c$ . In this range of values, cold mean flow can be considered to be nearly incompressible. The temperatures of the flow which are considered here take values from the ambient value (say, 20°C) up to 300°C. The flows with temperatures which are close to the ambient one are here simply referred to as cold flows. These ranges of mean flow speeds and temperatures represent well common flow conditions inside exhaust systems of cars. On the other hand, for the sake of simplicity, the values of all thermodynamic quantities of the exhausted gas are taken to match the values for dry air, that is, no further details on the chemical content of the gas are taken into account.

Besides the source of the mean flow, the sound source of interest is assumed to be located deep inside the pipe, far from the opening. In practice, it can be an internal combustion engine of a vehicle or a mouthpiece or reed of a music instrument. Regardless of the mechanism of its generation, the sound is considered to have a low dominant frequency, or, more precisely, long wavelength compared to the inner radius of the pipe. In the classical theory of acoustics, this is expressed with low values of Helmholtz number  $He = 2\pi a/\lambda$ , which is proportional to the ratio of the characteristic length  $a$ , in this case the pipe radius, and the wavelength of the sound  $\lambda$ . For Helmholtz number values below 1, the sound wave inside the straight pipe can be approximated as a (one-dimensional) plane wave. Since such a non-dimensional quantity is defined relative to the pipe radius, the actual upper limit for the frequency of the sound depends on the actual geometry. Taking the sound speed in still air at the ambient temperature as the reference and the pipe radius of 1cm, the upper frequency limit is around 5kHz, which most frequently covers majority of the relevant part of the audible frequency range. Therefore, the introduced low frequency assumption is not critical limitation for many problems in practice, such as noise of low orders of internal combustion engines or sound of musical instruments with relatively narrow pipes or in relatively low registers.

Another assumption which is frequently adopted in practice and here, as well, is that the unsteady pressure perturbations of the mean flow which are due to the acoustic wave are much smaller compared to the static value of the pressure. If the static pressure value is taken to be approximately 101kPa, this implies that at the sound pressure levels below around 150dB, the amplitude of the acoustic wave makes less than 1% of the static pressure value. These values are satisfied in most of the practical circumstances, since the sound pressure levels inside tail-pipes of exhaust systems and bores of wind instruments rarely exceed 150dB. On the other hand, this, so-called “small perturbations” assumption allows the implementation of linearized equations of acoustics, as will be shown later, which drastically simplifies both analytical and numerical calculations.

Lastly, the source of the incident plane wave inside the pipe is assumed to be the dominant source of sound also for the listener outside the pipe. In general, this assumption has to be verified in the particular case, since the main flow of gas can itself be a source of additional aerodynamic noise. Such flow-induced noise is typically generated at the pipe opening, which can make its contribution to the far-field radiation comparable to the contribution of the initial source inside the pipe. However, the noise generated by the flow is usually more pronounced at higher frequencies (typically, hissing noise) and it rarely dominates at low frequencies which are considered here. With regard to this, the far-field sound pressure is assumed to be directly proportional to the square root of the acoustic power of the source inside the pipe and the exterior sound field can then be quantified relative to the total sound power which is emitted from the pipe. While this is sufficient for the characterization of the exterior sound propagation and the estimation of the directivity of the pipe opening as the apparent source of sound, the absolute sound levels depend on the source inside the pipe. For that reason, most of the results derived throughout this work will point to the distribution of sound pressure levels outside the pipe, in particular, its dependence on the angle to the pipe axis, rather than the actual sound pressure levels, which are case-dependent.

## **1.2 Organization of contents**

Airborne acoustics and acoustics of moving and inhomogeneous media constitute a part of the larger area of fluid dynamics and sound waves in fluids obey the governing physical laws for fluids. Following this, the second chapter of the work starts with the governing equations of fluid dynamics and contains the derivation of the main equations which will be used throughout the rest of the work. These involve the systems of non-linear equations for steady and time-averaged flows, as well as the linearized equations for small (acoustic) perturbations. The latter ones include the systems of coupled pressure, density, and velocity equations and different forms of wave equations for simpler scenarios. Although the emphasis of the work is on the estimation of sound propagation in the mean flow, an overview of relevant aeroacoustic analogies is also given, as the vortex-sound interaction at the trailing

edge and the presence of the solid body of the pipe turn out to have a crucial effect on the far-field sound radiation.

In order to identify and subsequently quantify the most relevant physical phenomena which affect the spatial distribution of sound pressure outside the pipe, Chapter III gives the results of the laboratory measurements of directivity, with the pipe opening as a compact source of sound. The measurements are conducted in free-space conditions, the anechoic chamber, and the efforts are made to keep the measurement setup as close as possible to the idealized scenario described above. Naturally, the obtained results are used for the validation of subsequent analytical and numerical results, as well as for comparisons with the existing models from the literature.

Chapter IV provides a simple physical model of the most relevant flow and acoustic phenomena which determine the far sound field. The main idea of this part of the work is to isolate and characterize these phenomena in a compact and physically-based manner. This is critical for deeper understanding of the given measurement results, but also for further consideration of possible approaches for prediction of the radiated sound. In addition to this, the derived model provides a very fast and crude approximation of the directivity pattern in the presence of a hot or cold mean flow, with the pipe opening as a sound source in free space.

Chapter V considers once more the aeroacoustic analogies, which are typically used for similar types of problems involving a solid body in an inhomogeneous flow, but in the context of sound propagation in moving and inhomogeneous media. It attempts to adapt the existing aeroacoustic equations to capture the propagation in complex flows more accurately. The resulting exact equation is non-linear and without explicit analytical solution, but suitable for numerical calculations of sound propagation. Alternatively, an approximate linearized version is derived, which is appropriate for the case studied here, that is, small-amplitude sound radiation from an open pipe in the presence of a jet.

Industrial studies generally involve more complex scenarios, geometries, and mean flows. In such cases, engineers necessarily refer to numerical simulations of the sound field. In order to tackle such problems of practical importance, Chapter VI considers

several approaches for solving the problem of sound propagation inside the jet numerically, in conjunction with computational fluid dynamics. The derived conclusions should point to the most appropriate methodologies in terms of accuracy and efficiency, when solving this type of sound radiation problems.

The last, seventh chapter gives conclusions and possible future extensions of the work.

# Chapter II

## EQUATIONS OF FLUID DYNAMICS AND ACOUSTICS

In this chapter, we introduce the equations which characterise both the main flow of fluid and acoustic waves. They will be then used throughout the rest of the work. For the sake of clarity and completeness, the derivations are given in details, with all the important intermediate steps. A special emphasis is put on the conditions for the validity of each resulting equation. This will be valuable for analytical and numerical solutions of the sound radiation problem, when a compromise between the complexity of the physical model (the equations which are to be solved) and its ability to capture the essential phenomena becomes critical. Since no structure-born sound is taken into account, the starting point are governing equations of fluid dynamics, also frequently called Navier-Stokes equations, which cover not only acoustic waves, but dynamics of fluids in general.

### 2.1 Navier-Stokes equations

Navier-Stokes equations represent a set of conservation laws in fluids and, therefore, govern the physical behaviour of fluids. In their general form and with the Eulerian specification of the flow field (the observer is fixed in space), they read:

- conservation of mass or continuity equation

$$\frac{\partial \rho}{\partial t} + \nabla \cdot (\rho \mathbf{v}) = m, \quad (2.1)$$

- conservation of momentum or motion equation

$$\frac{\partial (\rho \mathbf{v})}{\partial t} + \nabla \cdot (\rho \mathbf{v} \mathbf{v}) + \nabla p - \nabla \cdot \boldsymbol{\tau} = m \mathbf{v} + \mathbf{f}, \text{ and} \quad (2.2)$$

- conservation of energy

$$\frac{\partial (\rho e_t)}{\partial t} + \nabla \cdot (\rho e_t \mathbf{v}) + \nabla \cdot (p \mathbf{v}) + \nabla \cdot \mathbf{q} - \nabla \cdot (\boldsymbol{\tau} \cdot \mathbf{v}) = m e_t + \mathbf{f} \cdot \mathbf{v} + \mathcal{G}. \quad (2.3)$$

The left-hand sides of the equations contain the primitive unknown quantities (rather than the conserved ones, such as momentum, which will also be addressed and used later) to describe the fluid: density ( $\rho$ ), vector of velocity ( $\mathbf{v}$ ), pressure ( $p$ ), viscous stress tensor ( $\tau$ ), total energy ( $e_t$ ), and heat flux vector ( $\mathbf{q}$ ). The right-hand sides contain the general external sources of mass ( $m$ ), force ( $\mathbf{f}$ ) and heat ( $\mathcal{G}$ ), which should be *a priori* known. In practice, they can be introduced to model complicated effects rather than solving the explicitly, which might significantly add to the complexity of the problem and encumber the calculations. For example, a mass source can only be considered in this context, since strictly speaking, no true source of mass can exist. In many cases, we will omit all the external sources in the derivations.

Somewhat more compact primitive formulation of the equations can be derived using the definition of the total (also called material, substantial, convective or Lagrangian) derivative:

$$\frac{D}{Dt} = \frac{\partial}{\partial t} + \mathbf{v} \cdot \nabla. \quad (2.4)$$

Its name should point to the fact that it describes well motion of a particle, small element of the fluid, moving with the velocity  $\mathbf{v}$ . For example, the solution of a simple one-dimensional first-order transport (convection, advection) differential equation with constant velocity  $v$ :

$$\frac{Df}{Dt} = \frac{\partial f}{\partial t} + v \frac{\partial f}{\partial x} = 0 \quad (2.5)$$

is any function of time ( $t$ ) and space ( $x$ ) of the form  $f(vt - x)$ . In other words, the particle moving with velocity  $v = x/t$  “carries” the information on the solution of the equation.

Returning back to the conservation laws, in the case of the continuity equation (2.1) we simply obtain:

$$\frac{\partial \rho}{\partial t} + \nabla \cdot (\rho \mathbf{v}) = \frac{\partial \rho}{\partial t} + \mathbf{v} \cdot \nabla \rho + \rho \nabla \cdot \mathbf{v} = \frac{D\rho}{Dt} + \rho \nabla \cdot \mathbf{v} = m. \quad (2.6)$$

Similar form of the momentum equation can be obtained after the expansion of the first two terms on the left-hand side of the equation (2.2):

$$\frac{\partial (\rho \mathbf{v})}{\partial t} + \nabla \cdot (\rho \mathbf{v} \mathbf{v}) = \rho \frac{\partial \mathbf{v}}{\partial t} + \mathbf{v} \frac{\partial \rho}{\partial t} + \rho \mathbf{v} \cdot \nabla \mathbf{v} + \mathbf{v} \nabla \cdot (\rho \mathbf{v}) \quad (2.7)$$

and the subtraction of the mass equation (2.1) multiplied with  $\mathbf{v}$  from it, which then gives:

$$\rho \frac{D\mathbf{v}}{Dt} + \nabla p - \nabla \cdot \boldsymbol{\tau} = \mathbf{f}. \quad (2.8)$$

Lastly, the expansion of the first two terms on the left-hand side of the energy equation (2.3):

$$\frac{\partial(\rho e_t)}{\partial t} + \nabla \cdot (\rho e_t \mathbf{v}) = \rho \frac{\partial e_t}{\partial t} + e_t \frac{\partial \rho}{\partial t} + \rho \mathbf{v} \cdot \nabla e_t + e_t \nabla \cdot (\rho \mathbf{v}) \quad (2.9)$$

and the subtraction of the mass equation multiplied with  $e_t$  from it, result in the following primitive formulation of the energy equation:

$$\rho \frac{De_t}{Dt} + \nabla \cdot (\rho \mathbf{v}) + \nabla \cdot \mathbf{q} - \nabla \cdot (\boldsymbol{\tau} \cdot \mathbf{v}) = \mathbf{f} \cdot \mathbf{v} + \mathcal{G}. \quad (2.10)$$

Since there are much more unknowns (three scalars, two vectors, and one second-order tensor) than the equations (two scalar and one vector equation), additional relations between the unknowns are necessary. The second law of thermodynamics gives the following equality for small reversible changes of fluid's state [Bat02]:

$$T \delta s = \delta e + p \delta \left( \frac{1}{\rho} \right) = \delta e - \frac{p}{\rho^2} \delta \rho, \quad (2.11)$$

where  $\delta$  denotes differential (a small change of a quantity),  $T$  is temperature,  $s$  is entropy, and  $e$  is internal energy of the fluid, which is related to the total energy by the equality (total energy is the sum of internal and kinetic energy):

$$e_t = e + \frac{v^2}{2}. \quad (2.12)$$

In the most general case, when all the quantities which describe particles of the fluid are functions of space and time in the sense of classical mechanics, the differentials can be replaced with total derivatives to obtain the expression:

$$T \frac{Ds}{Dt} = \frac{De}{Dt} + p \frac{D}{Dt} \left( \frac{1}{\rho} \right) = \frac{De}{Dt} - \frac{p}{\rho^2} \frac{D\rho}{Dt}. \quad (2.13)$$

On the other hand, equations of state imply that the fluid is completely described with two independent parameters of state [Bat02], whereas any other parameter can be expressed as a function of these two parameters. These two basic parameters can be

chosen arbitrarily and in various ways. If we choose a thermodynamic equation of state which relates density to the pressure and entropy [Del14], this means that:

$$\delta\rho = \left(\frac{\delta\rho}{\delta p}\right)_s \delta p + \left(\frac{\delta\rho}{\delta s}\right)_p \delta s. \quad (2.14)$$

In other words, any change of density can be interpreted as a consequence of two superimposed effects – change of pressure at constant entropy and change of entropy at constant pressure. Since the increase of pressure always results in compression, that is increase of density,  $(\delta\rho/\delta p)_s$  is strictly positive and we can define a scalar  $c$ , such that:

$$\left(\frac{\delta\rho}{\delta p}\right)_s = \frac{1}{c^2}. \quad (2.15)$$

It will be shown later (when the classical wave equation is obtained) that the parameter  $c$  represents the speed of sound waves in the fluid. In addition to this, we can also define [Del14]:

$$\left(\frac{\delta\rho}{\delta s}\right)_p = -\sigma\rho, \quad (2.16)$$

where  $\sigma$  turns out to be reciprocal of (commonly constant) specific heat capacity at constant pressure ( $c_p$ ) in perfect gases (see equation (2.35)).

Therefore, after replacing all differentials with total derivatives, the equation of state (2.14) becomes:

$$\frac{D\rho}{Dt} = \frac{1}{c^2} \frac{Dp}{Dt} - \sigma\rho \frac{Ds}{Dt}. \quad (2.17)$$

Introducing the second law of thermodynamics (2.13) into this equality results in:

$$\frac{D\rho}{Dt} = \frac{1}{c^2} \frac{Dp}{Dt} - \frac{\sigma\rho}{T} \frac{De}{Dt} + \frac{\sigma p}{\rho T} \frac{D\rho}{Dt}, \quad (2.18)$$

or equivalently:

$$\frac{1}{c^2} \frac{Dp}{Dt} = \frac{\sigma\rho}{T} \frac{De}{Dt} + \left(1 - \frac{\sigma p}{\rho T}\right) \frac{D\rho}{Dt}. \quad (2.19)$$

In order to eliminate the internal energy from the equations, it is convenient to expand the primitive form of the energy equation (2.10) with equality (2.12) as:

$$\rho \frac{De}{Dt} + \rho \frac{D(v^2/2)}{Dt} + \nabla \cdot (p\mathbf{v}) + \nabla \cdot \mathbf{q} - \nabla \cdot (\boldsymbol{\tau} \cdot \mathbf{v}) = \mathbf{f} \cdot \mathbf{v} + \mathcal{G}. \quad (2.20)$$

The second term on the left-hand side can now be expressed using the scalar product of the momentum equation (2.8) with velocity. This gives:

$$\rho \mathbf{v} \cdot \frac{D\mathbf{v}}{Dt} + \mathbf{v} \cdot \nabla p - \mathbf{v} \cdot \nabla \cdot \boldsymbol{\tau} = \mathbf{f} \cdot \mathbf{v}. \quad (2.21)$$

After noticing that:

$$\begin{aligned} \rho \mathbf{v} \cdot \frac{D\mathbf{v}}{Dt} &= \rho \left( \mathbf{v} \cdot \frac{\partial \mathbf{v}}{\partial t} + \mathbf{v} \cdot (\mathbf{v} \cdot \nabla \mathbf{v}) \right) = \rho \left\{ \frac{1}{2} \frac{\partial (\mathbf{v} \cdot \mathbf{v})}{\partial t} + \mathbf{v} \cdot \left[ \nabla \frac{v^2}{2} + (\nabla \times \mathbf{v}) \times \mathbf{v} \right] \right\} \\ &= \rho \frac{D(v^2/2)}{Dt} + \underbrace{\rho \mathbf{v} \cdot [(\nabla \times \mathbf{v}) \times \mathbf{v}]}_{=0} = \rho \frac{D(v^2/2)}{Dt}, \end{aligned} \quad (2.22)$$

we can subtract (2.21) from the expanded energy equation (2.20) to obtain<sup>1</sup>:

$$\begin{aligned} \rho \frac{De}{Dt} + \nabla \cdot (p\mathbf{v}) + \nabla \cdot \mathbf{q} - \nabla \cdot (\boldsymbol{\tau} \cdot \mathbf{v}) - \mathbf{v} \cdot \nabla p + \mathbf{v} \cdot \nabla \cdot \boldsymbol{\tau} \\ = \rho \frac{De}{Dt} + p \nabla \cdot \mathbf{v} + \nabla \cdot \mathbf{q} - \boldsymbol{\tau} : \nabla \mathbf{v} = \mathcal{G}. \end{aligned} \quad (2.23)$$

We can now insert (2.23) and the mass equation (2.6) into the second law of thermodynamics (2.13) and obtain:

$$\frac{Ds}{Dt} = \frac{1}{\rho T} \left( -\frac{p}{\rho} m + \mathcal{G} - \nabla \cdot \mathbf{q} + \boldsymbol{\tau} : \nabla \mathbf{v} \right). \quad (2.24)$$

In other words, flows without mass and heat sources and with negligible effects of viscosity and heat conduction are isentropic ( $Ds/Dt = 0$ ). Moreover, if we insert the same equations, (2.23) and (2.6), into the combination of the equation of state and the second law of thermodynamics (2.13), we obtain the following expressions for pressure:

$$\frac{1}{c^2} \frac{Dp}{Dt} + \rho \nabla \cdot \mathbf{v} + \frac{\sigma}{T} (\nabla \cdot \mathbf{q} - \boldsymbol{\tau} : \nabla \mathbf{v}) = m \left( 1 - \frac{\sigma p}{\rho T} \right) + \frac{\sigma \mathcal{G}}{T}, \quad (2.25)$$

or, combining together with the equality (2.24):

$$\begin{aligned} \frac{1}{c^2} \frac{Dp}{Dt} &= -\rho \nabla \cdot \mathbf{v} + m \left( 1 - \frac{\sigma p}{\rho T} \right) + \frac{\sigma}{T} (\mathcal{G} - \nabla \cdot \mathbf{q} + \boldsymbol{\tau} : \nabla \mathbf{v}) \\ &= -\rho \nabla \cdot \mathbf{v} + m + \sigma \rho \frac{Ds}{Dt}. \end{aligned} \quad (2.26)$$

This important relation is frequently used as a substitute for the energy equation, since in the common case of isentropic flow, when heat conduction ( $\nabla \cdot \mathbf{q}$ ) and viscosity

---

<sup>1</sup>  $\nabla \cdot (\boldsymbol{\tau} \cdot \mathbf{v}) = \mathbf{v} \cdot \nabla \cdot \boldsymbol{\tau} + \boldsymbol{\tau} : \nabla \mathbf{v}$

effects ( $\tau : \nabla \mathbf{v}$ ) are negligible and no sources of mass or heat are present, it simplifies to:

$$\frac{1}{c^2} \frac{Dp}{Dt} = -\rho \nabla \cdot \mathbf{v}, \quad (2.27)$$

which then uses the same variables as the mass and momentum equations (with the exception of the sound speed  $c$ , which is commonly expressed with the equation (2.34) for a perfect gas, as discussed below). Hence, these three equations, one vector and two scalar equations, can close the system of equations with one vector and two scalar parameters, namely, velocity, pressure, and density.

Equation for the speed of sound is commonly derived using a perfect gas approximation, for which the thermal equation of state gives [Bat02]:

$$p = \rho RT, \quad (2.28)$$

where  $R = c_p - c_v$  is specific gas constant and  $c_p$  and  $c_v$  are specific heat capacities for constant pressure and volume, respectively. In dry air, these constants vary only slightly with temperature and in many circumstances can be considered to be constant:  $R = 287 \text{ J}/(\text{kgK})$ ,  $c_p = 1005 \text{ J}/(\text{kgK})$ , and  $c_v = 718 \text{ J}/(\text{kgK})$ . As a consequence:

$$\delta p = RT \delta \rho + \rho R \delta T. \quad (2.29)$$

On the other hand, the caloric equation of state of a perfect gas implies that internal energy is a function of temperature alone:

$$de = c_v dT. \quad (2.30)$$

Combining the last two equations:

$$de = \frac{c_v}{\rho R} (\delta p - RT \delta \rho). \quad (2.31)$$

Inserting this into the second law of thermodynamics, equation (2.11), gives:

$$T \delta s = \frac{c_v}{\rho R} \delta p - \left( \frac{c_v T}{\rho} + \frac{p}{\rho^2} \right) \delta \rho, \quad (2.32)$$

which together with the equation (2.28) gives:

$$\rho RT \delta s = c_v \delta p - (c_v RT + R^2 T) \delta \rho = c_v \delta p - c_p RT \delta \rho. \quad (2.33)$$

Now, it is easy to find that from the definitions (2.15) and (2.16):

$$c^2 = \left( \frac{\delta p}{\delta \rho} \right)_s = \frac{c_p RT}{c_v} = \gamma RT = \frac{\mathcal{P}}{\rho}, \quad (2.34)$$

where we introduced the heat capacity ratio:  $\gamma = c_p / c_v$ , and:

$$\sigma = -\frac{1}{\rho} \left( \frac{\delta \rho}{\delta s} \right)_p = \frac{1}{c_p}. \quad (2.35)$$

In conclusion, the system of equations:

$$\frac{D\rho}{Dt} + \rho \nabla \cdot \mathbf{v} = m, \quad (2.36)$$

$$\rho \frac{D\mathbf{v}}{Dt} + \nabla p = \mathbf{f}, \text{ and} \quad (2.37)$$

$$\frac{1}{c^2} \frac{Dp}{Dt} + \rho \nabla \cdot \mathbf{v} = m \left( 1 - \frac{\sigma p}{\rho T} \right) + \frac{\sigma \mathcal{G}}{T} \quad (2.38)$$

is closed in the case of a perfect gas with the relations:

$$p = \rho RT, \quad c^2 = \frac{\mathcal{P}}{\rho}, \text{ and } \sigma = \frac{1}{c_p}, \quad (2.39)$$

when heat conduction and viscous dissipation are negligible, without any further approximations. When the latter is not true, viscous stress tensor in equations (2.8) and (2.26) is frequently modelled by assuming a Newtonian fluid under Stokes' hypothesis of local thermodynamic equilibrium of the fluid<sup>2</sup> [RH16]:

$$\boldsymbol{\tau} = \mu \left( \nabla \mathbf{v} + (\nabla \mathbf{v})^T - \frac{2}{3} I \nabla \cdot \mathbf{v} \right), \quad (2.40)$$

where  $\mu$  is dynamic viscosity, which in general depends on temperature, and  $I$  denotes the unit tensor. The heat flux in equation (2.26) is most frequently expressed using Fourier's law:

$$\mathbf{q} = -K \nabla T, \quad (2.41)$$

where  $K = K(p, T)$  denotes heat conductivity, which is in general a function of pressure and temperature. In the following, however, the flows of a perfect gas (air) will always be considered to have negligible effects of viscosity (inviscid flows) and heat conduction, which is a very common approximation when acoustic (sound) waves are primarily considered.

---

<sup>2</sup>  $\nabla \mathbf{v} + (\nabla \mathbf{v})^T = \partial v_i / \partial x_j + \partial v_j / \partial x_i$

Still, it should be noted that the system of Navier-Stokes equations (and the equations derived from it above) includes all types of motion of fluids (both liquids and gases), such as vorticity, entropy, and acoustic modes, together with the effects such as convection and diffusion. This comprehensiveness makes them at the same time very difficult to solve, not only analytically, but with the aid of numerical solvers, as well. Hence, depending on the aspect of the fluid motion which is in the focus, additional approximations (modelling) of the flow have to be introduced in practice, in order to further simplify the governing equations and make their solution feasible. This will be the goal in the rest of this chapter, towards the specific case of sound radiation from an open pipe.

## 2.2 Steady flow

The first model which will be covered assumes a steady flow, that is, flow without any unsteady perturbations in which the variables change in time. Therefore, vary only spatial variations of flow properties are allowed. Such steady quantities we will denote with the subscript  $_0$ . The governing equations (2.1), (2.8), and (2.25) and the equations of a perfect gas (2.39) can be written accordingly as:

$$\nabla \cdot (\rho_0 \mathbf{v}_0) = m_0, \quad (2.42)$$

$$\rho_0 \mathbf{v}_0 \cdot \nabla \mathbf{v}_0 + \nabla p_0 - \nabla \cdot \boldsymbol{\tau}_0 = \mathbf{f}_0, \quad (2.43)$$

$$\frac{1}{c_0^2} \mathbf{v}_0 \cdot \nabla p_0 + \rho_0 \nabla \cdot \mathbf{v}_0 + \frac{\sigma}{T_0} (\nabla \cdot \mathbf{q}_0 - \boldsymbol{\tau}_0 : \nabla \mathbf{v}_0) = m_0 \left( 1 - \frac{\sigma p_0}{\rho_0 T_0} \right) + \frac{\sigma \mathcal{G}_0}{T_0}, \quad (2.44)$$

$$p_0 = \rho_0 R T_0, \quad c_0^2 = \frac{\mathcal{P}_0}{\rho_0}, \quad \text{and} \quad \sigma = \frac{1}{c_p}. \quad (2.45)$$

If we further assume an isentropic steady flow ( $Ds_0/Dt = 0$ , that is, according to the equation (2.24):  $m_0 = 0$ ,  $\mathcal{G}_0 = 0$ ,  $\nabla \cdot \mathbf{q}_0 = 0$ , and  $\boldsymbol{\tau}_0 : \nabla \mathbf{v}_0 = 0$ ) without external steady forces ( $\mathbf{f}_0 = 0$ ), the closed system of equations becomes:

$$\nabla \cdot (\rho_0 \mathbf{v}_0) = 0, \quad (2.46)$$

$$\rho_0 \mathbf{v}_0 \cdot \nabla \mathbf{v}_0 + \nabla p_0 = 0, \quad (2.47)$$

$$\mathbf{v}_0 \cdot \nabla p_0 + \rho_0 c_0^2 \nabla \cdot \mathbf{v}_0 = 0, \text{ and} \quad (2.48)$$

$$\rho_0 c_0^2 = \mathcal{P}_0. \quad (2.49)$$

According to its definition, steady flow cannot include any temporal variation of flow parameters. Still, steady flow parameters should not be confused with time averages of generally unsteady fluctuations of the flow. The reason is that the latter ones can also depend on the additional unsteady components of the flow within higher-order approximations. Therefore, the next subsection considers time-averaged values of generally time-dependent flow parameters. The averaging over time is done using the Reynolds technique.

## 2.3 Reynolds-averaged Navier-Stokes equations

The most frequently used procedure for deriving time-averaged properties of flows was introduced by Reynolds [Rey95]. When it is applied on the set of Navier-Stokes equations, the obtained system of equations is referred to as Reynolds-averaged Navier-Stokes equations (RANS). The entire procedure is based on the decomposition of an unsteady flow into the steady component, which is time independent (and, as before, denoted with the subscript  $_0$ ) and unsteady perturbations around them (denoted with prime  $'$ ), which have a zero mean value over time. Such perturbations can originate, for example, from turbulences of the flow or sound waves. Generic flow field  $f$  (holds also for vector fields) can, thus, be represented as the sum of the two components:

$$f(\mathbf{x}, t) = f_0(\mathbf{x}) + f'(\mathbf{x}, t), \quad (2.50)$$

with only the second one being dependent on time. The steady component is defined with:

$$f_0(\mathbf{x}) = \overline{f(\mathbf{x}, t)} = \lim_{T \rightarrow \infty} \frac{1}{T} \int_0^T f(\mathbf{x}, t) dt, \quad (2.51)$$

where  $t$  is time and  $T \rightarrow \infty$  is the interval of averaging, which theoretically expands to infinity. In practice, the interval of averaging has to be much larger than any

characteristic period of the fluctuations of the flow and this component of the flow is then considered to satisfy quasi steady conditions. The time-averaging operator  $\overline{\quad}$  is linear and obviously  $\overline{f_0} = f_0$  and  $\overline{f'} = 0$  hold.

The following properties of Reynolds time-averaging can also be obtained [Rey95] for any three functions of space and time  $f$ ,  $g$  and  $h$ :

$$\overline{f + g} = \overline{f_0} + \overline{f'} + \overline{g_0} + \overline{g'} = f_0 + g_0, \quad (2.52)$$

$$\begin{aligned} \overline{fg} &= \overline{(f_0 + f')(g_0 + g')} = \overline{f_0 g_0} + \overline{f_0 g'} + \overline{f' g_0} + \overline{f' g'} \\ &= f_0 g_0 + f_0 \overline{g'} + g_0 \overline{f'} + \overline{f' g'} = f_0 g_0 + \overline{f' g'}, \end{aligned} \quad (2.53)$$

$$\begin{aligned} \overline{fgh} &= \overline{(f_0 + f')(g_0 + g')(h_0 + h')} \\ &= \overline{f_0 g_0 h_0} + \overline{f' g_0 h_0} + \overline{f_0 g' h_0} + \overline{f_0 g_0 h'} + \overline{f' g' h_0} + \overline{f' g_0 h'} + \overline{f_0 g' h'} + \overline{f' g' h'} \\ &= f_0 g_0 h_0 + g_0 h_0 \overline{f'} + f_0 h_0 \overline{g'} + f_0 g_0 \overline{h'} + h_0 \overline{f' g'} + g_0 \overline{f' h'} + f_0 \overline{g' h'} + \overline{f' g' h'} \\ &= f_0 g_0 h_0 + h_0 \overline{f' g'} + g_0 \overline{f' h'} + f_0 \overline{g' h'} + \overline{f' g' h'}, \end{aligned} \quad (2.54)$$

$$\frac{\partial \overline{f}}{\partial t} = \frac{\partial \overline{f'}}{\partial t} = \frac{\partial \overline{f'}}{\partial t} = 0, \text{ and} \quad (2.55)$$

$$\overline{\nabla f} = \nabla \overline{f} = \nabla f_0. \quad (2.56)$$

The identities (2.53) and (2.54) show that the time average of a product of two or more variables is a sum of two contributions, a product of time averages and the covariance terms. The latter ones are equal to zero only if the involved variables are uncorrelated, which is rarely the case with the quantities which describe dynamics of fluids [FP02]. Otherwise, they can be neglected (to the first-order, linear accuracy) only if the amplitudes of unsteady perturbations are much smaller compared to the corresponding steady values. This is most frequently case with sound waves at reasonably small sound pressure levels, as will be discussed later. However, it does not necessarily hold for turbulences and the unsteady parameters associated with them, the amplitudes of which might be of the same order of magnitude as their steady counterparts.

For simplicity, we will again assume an isentropic flow without external sources. Time averaging of the three governing equations (2.1), (2.37), and (2.38) and implementation of the identities above give:

$$\overline{\frac{\partial \rho}{\partial t} + \nabla \cdot (\rho \mathbf{v})} = \underbrace{\overline{\frac{\partial \rho}{\partial t}}}_{=0} + \overline{\nabla \cdot (\rho \mathbf{v})} = \nabla \cdot \overline{(\rho \mathbf{v})} = \nabla \cdot (\rho_0 \mathbf{v}_0) + \nabla \cdot \overline{\rho' \mathbf{v}'} = 0, \quad (2.57)$$

$$\begin{aligned} \overline{\rho \frac{D\mathbf{v}}{Dt} + \nabla p} &= \overline{\rho \frac{\partial \mathbf{v}}{\partial t} + \rho \mathbf{v} \cdot \nabla \mathbf{v} + \nabla p} = \rho_0 \underbrace{\overline{\frac{\partial \mathbf{v}'}{\partial t}}}_{=0} + \overline{\rho' \frac{\partial \mathbf{v}'}{\partial t} + \rho \mathbf{v} \cdot \nabla \mathbf{v} + \nabla p} \\ &= \overline{\rho' \frac{\partial \mathbf{v}'}{\partial t} + \rho_0 \mathbf{v}_0 \cdot \nabla \mathbf{v}_0 + \rho' \mathbf{v}' \cdot \nabla \mathbf{v}_0 + \rho_0 \mathbf{v}' \cdot \nabla \mathbf{v}'} + \overline{\rho' \mathbf{v}_0 \cdot \nabla \mathbf{v}'} + \overline{\rho' \mathbf{v}' \cdot \nabla \mathbf{v}'} + \nabla p_0 \quad (2.58) \\ &= \overline{\rho' \frac{\partial \mathbf{v}'}{\partial t} + \rho_0 \mathbf{v}_0 \cdot \nabla \mathbf{v}_0 + \rho' \mathbf{v}' \cdot \nabla \mathbf{v}_0 + \rho_0 \mathbf{v}' \cdot \nabla \mathbf{v}'} + \mathbf{v}_0 \cdot \overline{\rho' \nabla \mathbf{v}'} + \overline{\rho' \mathbf{v}' \cdot \nabla \mathbf{v}'} + \nabla p_0 = 0, \end{aligned}$$

$$\begin{aligned} \overline{\frac{Dp}{Dt} + \rho c^2 \nabla \cdot \mathbf{v}} &= \underbrace{\overline{\frac{\partial p}{\partial t}}}_{=0} + \overline{\mathbf{v} \cdot \nabla p + \rho c^2 \nabla \cdot \mathbf{v}} = \mathbf{v}_0 \cdot \nabla p_0 + \overline{\mathbf{v}' \cdot \nabla p'} + \rho_0 c_0^2 \nabla \cdot \mathbf{v}_0 \\ &\quad + \overline{\rho' (c^2)' \nabla \cdot \mathbf{v}_0 + \rho' c_0^2 \nabla \cdot \mathbf{v}' + \rho_0 (c^2)' \nabla \cdot \mathbf{v}' + \rho' (c^2)' \nabla \cdot \mathbf{v}'} \quad (2.59) \\ &= \mathbf{v}_0 \cdot \nabla p_0 + \overline{\mathbf{v}' \cdot \nabla p'} + \rho_0 c_0^2 \nabla \cdot \mathbf{v}_0 + \overline{\rho' (c^2)' \nabla \cdot \mathbf{v}_0 + c_0^2 \overline{\rho' \nabla \cdot \mathbf{v}'}} \\ &\quad + \overline{\rho_0 (c^2)' \nabla \cdot \mathbf{v}'} + \overline{\rho' (c^2)' \nabla \cdot \mathbf{v}'} = 0. \end{aligned}$$

If we compare these equations with the equations for an isentropic steady flow (2.46)-(2.48), we notice that time-averaged unsteady flows obey different equations, as mentioned earlier. The additional perturbation terms involve covariance of different flow quantities and are essentially due to the non-linear character of the initial Navier-Stokes equations. Moreover, they introduce new unknowns which cannot be expressed only with steady quantities, as is the case with steady flows. In order to close the system of equations, the covariance terms have to be approximated. For turbulent flows, this is most commonly done using the so-called turbulence models, while for sound waves they are commonly neglected (see Linearized Euler Equations below). However, there is no exact set of equations which can be used generally to obtain time-averaged values of parameters for unsteady flows.

Neither steady nor Reynolds-averaged flows contain in their solutions acoustic waves, which are essentially time-varying, unsteady perturbations of the flow. The rest of the chapter is, therefore, focused on time dependent fluctuations of a flow, assuming that the mean flow properties are well known.

## 2.4 Linearized Euler Equations

Linearized Euler Equations (LEE) are derived in two steps. In the first step, the flow is, as before, split into its steady component and unsteady perturbation. The system of equations for the unsteady perturbations is obtained by subtracting the time-averaged terms derived in the previous subsection from the governing equations. In the second step, the linearization is done by assuming that the amplitudes of perturbations are much smaller than the corresponding steady values of the flow. This allows the non-linear terms involving the perturbations to be neglected. As a result, a system of linear partial differential equations is derived.

Introducing the split  $f(\mathbf{x},t) = f_0(\mathbf{x}) + f'(\mathbf{x},t)$  to all flow parameters (density, velocity, and pressure), the non-linear conservation equations (2.1), (2.37), and (2.38) become (with, as before,  $m = 0$ ,  $\mathbf{f} = 0$ ,  $\mathcal{G} = 0$ ,  $\nabla \cdot \mathbf{q} = 0$ ,  $\boldsymbol{\tau} : \nabla \mathbf{v} = 0$  and  $\nabla \cdot \boldsymbol{\tau} = 0$  in an isentropic flow without external sources):

$$\frac{\partial \rho}{\partial t} + \nabla \cdot (\rho \mathbf{v}) = \frac{\partial \rho'}{\partial t} + \nabla \cdot (\rho_0 \mathbf{v}_0) + \nabla \cdot (\rho_0 \mathbf{v}') + \nabla \cdot (\rho' \mathbf{v}_0) + \nabla \cdot (\rho' \mathbf{v}') = 0, \quad (2.60)$$

$$\begin{aligned} \rho \frac{D\mathbf{v}}{Dt} + \nabla p &= \rho_0 \frac{\partial \mathbf{v}'}{\partial t} + \rho' \frac{\partial \mathbf{v}'}{\partial t} + \rho_0 \mathbf{v}_0 \cdot \nabla \mathbf{v}_0 + \rho_0 \mathbf{v}_0 \cdot \nabla \mathbf{v}' + \rho_0 \mathbf{v}' \cdot \nabla \mathbf{v}_0 \\ &+ \rho' \mathbf{v}_0 \cdot \nabla \mathbf{v}_0 + \rho_0 \mathbf{v}' \cdot \nabla \mathbf{v}' + \rho' \mathbf{v}_0 \cdot \nabla \mathbf{v}' + \rho' \mathbf{v}' \cdot \nabla \mathbf{v}_0 + \rho' \mathbf{v}' \cdot \nabla \mathbf{v}' \\ &+ \nabla p_0 + \nabla p' = 0, \end{aligned} \quad (2.61)$$

$$\begin{aligned} \frac{Dp}{Dt} + \rho c^2 \nabla \cdot \mathbf{v} &= \frac{\partial p'}{\partial t} + \mathbf{v}_0 \cdot \nabla p_0 + \mathbf{v}_0 \cdot \nabla p' + \mathbf{v}' \cdot \nabla p_0 + \mathbf{v}' \cdot \nabla p' + \rho_0 c_0^2 \nabla \cdot \mathbf{v}_0 \\ &+ \rho_0 c_0^2 \nabla \cdot \mathbf{v}' + \rho_0 (c^2)' \nabla \cdot \mathbf{v}_0 + \rho' c_0^2 \nabla \cdot \mathbf{v}_0 + \rho_0 (c^2)' \nabla \cdot \mathbf{v}' + \rho' c_0^2 \nabla \cdot \mathbf{v}' \\ &+ \rho' (c^2)' \nabla \cdot \mathbf{v}_0 + \rho' (c^2)' \nabla \cdot \mathbf{v}' = 0. \end{aligned} \quad (2.62)$$

On the other hand, after noticing that  $\overline{(\cdot)} = (\cdot) - (\cdot)^p$ , where  $(\cdot)$  denotes any expression and  $(\cdot)^p$  its perturbation of any order, the time-averaged flow equations (2.57)-(2.59) can be recast to, respectively:

$$\nabla \cdot (\rho_0 \mathbf{v}_0) + \nabla \cdot \overline{\rho' \mathbf{v}'} = \nabla \cdot (\rho_0 \mathbf{v}_0) + \nabla \cdot (\rho' \mathbf{v}') - \nabla \cdot (\rho' \mathbf{v}')^p = 0, \quad (2.63)$$

$$\begin{aligned}
& \overline{\rho' \frac{\partial \mathbf{v}'}{\partial t}} + \rho_0 \mathbf{v}_0 \cdot \nabla \mathbf{v}_0 + \overline{\rho' \mathbf{v}'} \cdot \nabla \mathbf{v}_0 + \rho_0 \overline{\mathbf{v}' \cdot \nabla \mathbf{v}'} + \mathbf{v}_0 \cdot \overline{\rho' \nabla \mathbf{v}'} + \overline{\rho' \mathbf{v}' \cdot \nabla \mathbf{v}'} + \nabla p_0 \\
& = \rho' \frac{\partial \mathbf{v}'}{\partial t} - \left( \rho' \frac{\partial \mathbf{v}'}{\partial t} \right)^P + \rho_0 \mathbf{v}_0 \cdot \nabla \mathbf{v}_0 + \rho' \mathbf{v}' \cdot \nabla \mathbf{v}_0 - (\rho' \mathbf{v}')^P \cdot \nabla \mathbf{v}_0 \\
& \quad + \rho_0 \mathbf{v}' \cdot \nabla \mathbf{v}' - \rho_0 (\mathbf{v}' \cdot \nabla \mathbf{v}')^P + \mathbf{v}_0 \cdot \rho' \nabla \mathbf{v}' - \mathbf{v}_0 \cdot (\rho' \nabla \mathbf{v}')^P + \rho' \mathbf{v}' \cdot \nabla \mathbf{v}' \\
& \quad - (\rho' \mathbf{v}' \cdot \nabla \mathbf{v}')^P + \nabla p_0 = 0,
\end{aligned} \tag{2.64}$$

$$\begin{aligned}
& \mathbf{v}_0 \cdot \nabla p_0 + \overline{\mathbf{v}' \cdot \nabla p'} + \rho_0 c_0^2 \nabla \cdot \mathbf{v}_0 + \overline{\rho' (c^2)' \nabla \cdot \mathbf{v}_0} + c_0^2 \overline{\rho' \nabla \cdot \mathbf{v}'} \\
& \quad + \overline{\rho_0 (c^2)' \nabla \cdot \mathbf{v}'} + \overline{\rho' (c^2)' \nabla \cdot \mathbf{v}'} \\
& = \mathbf{v}_0 \cdot \nabla p_0 + \mathbf{v}' \cdot \nabla p' - (\mathbf{v}' \cdot \nabla p')^P + \rho_0 c_0^2 \nabla \cdot \mathbf{v}_0 + \rho' (c^2)' \nabla \cdot \mathbf{v}_0 \\
& \quad - (\rho' (c^2)')^P \nabla \cdot \mathbf{v}_0 + c_0^2 \rho' \nabla \cdot \mathbf{v}' - c_0^2 (\rho' \nabla \cdot \mathbf{v}')^P + \rho_0 (c^2)' \nabla \cdot \mathbf{v}' \\
& \quad - \rho_0 ((c^2)')^P \nabla \cdot \mathbf{v}' + \rho' (c^2)' \nabla \cdot \mathbf{v}' - (\rho' (c^2)' \nabla \cdot \mathbf{v}')^P = 0.
\end{aligned} \tag{2.65}$$

We can now subtract the last three equations of the time-averaged flow from the corresponding conservation equations (2.60)-(2.62), which represent the full flow (mean flow plus perturbations), to obtain the non-linear perturbation equations without the mean flow components:

$$\frac{\partial \rho'}{\partial t} + \nabla \cdot (\rho_0 \mathbf{v}') + \nabla \cdot (\rho' \mathbf{v}_0) + \nabla \cdot (\rho' \mathbf{v}')^P = 0, \tag{2.66}$$

$$\begin{aligned}
\rho_0 \frac{\partial \mathbf{v}'}{\partial t} + \left( \rho' \frac{\partial \mathbf{v}'}{\partial t} \right)^P + \rho_0 \mathbf{v}_0 \cdot \nabla \mathbf{v}' + \rho_0 \mathbf{v}' \cdot \nabla \mathbf{v}_0 + \rho' \mathbf{v}_0 \cdot \nabla \mathbf{v}_0 + (\rho' \mathbf{v}')^P \cdot \nabla \mathbf{v}_0 \\
+ \rho_0 (\mathbf{v}' \cdot \nabla \mathbf{v}')^P + \mathbf{v}_0 \cdot (\rho' \nabla \mathbf{v}')^P + (\rho' \mathbf{v}' \cdot \nabla \mathbf{v}')^P + \nabla p' = 0,
\end{aligned} \tag{2.67}$$

$$\begin{aligned}
\frac{\partial p'}{\partial t} + \mathbf{v}_0 \cdot \nabla p' + \mathbf{v}' \cdot \nabla p_0 + (\mathbf{v}' \cdot \nabla p')^P + \rho_0 c_0^2 \nabla \cdot \mathbf{v}' + \rho_0 (c^2)' \nabla \cdot \mathbf{v}_0 + \rho' c_0^2 \nabla \cdot \mathbf{v}_0 \\
+ (\rho' (c^2)')^P \nabla \cdot \mathbf{v}_0 + c_0^2 (\rho' \nabla \cdot \mathbf{v}')^P + \rho_0 ((c^2)')^P \nabla \cdot \mathbf{v}' + (\rho' (c^2)' \nabla \cdot \mathbf{v}')^P = 0.
\end{aligned} \tag{2.68}$$

Linearization (the first-order approximation) of the equations is accomplished by omitting the second- and third-order perturbation terms, which contain the products of two or more perturbation quantities. From the obtained equations (2.66)-(2.68), it follows that such higher-order terms can be neglected whenever the following conditions are satisfied:

$$\rho' \ll \rho_0, \tag{2.69}$$

$$\mathbf{v}' \ll \mathbf{v}_0 \text{ or } (\mathbf{v}' \cdot \nabla \mathbf{v}') \ll \frac{\partial \mathbf{v}'}{\partial t} \text{ and } \mathbf{v}' \cdot \nabla p' \ll \frac{\partial p'}{\partial t}, \tag{2.70}$$

$$(c^2)' \ll c_0^2. \tag{2.71}$$

If the unsteady perturbations of different flow quantities are assumed to have the same characteristic length scale (no matter if they originate from the turbulences or acoustic waves), then, for example,  $\nabla \cdot (\rho' \mathbf{v}')^p \ll \nabla \cdot (\rho_0 \mathbf{v}')$  always holds when  $\rho' \ll \rho_0$  is satisfied. The condition (2.70) implies that the particle velocity induced by the unsteady flow perturbations (e.g. turbulence) is much smaller than its propagation velocity (the steady flow velocity) or, in the special case when sound waves are the only perturbations of otherwise still medium, the amplitude of the particle velocity has to be much smaller than the speed of sound in the medium (since then the following scaling holds:  $\mathbf{v}' \cdot \nabla : \frac{\partial}{\partial t} \sim v' k : \omega \sim v' : c$  and  $c = \omega/k \approx c_0$ , where  $\omega$  and  $k$  denote angular frequency and wave number of the sound, respectively, and the condition (2.71) also applies). For brevity, the linearization is most often said to be justified in the case of small perturbations of the flow, the amplitudes of which are much smaller than the corresponding steady values. Thus, Linearized Euler Equations (sometimes also referred to as linearized equations of gas dynamics) read:

$$\frac{\partial \rho'}{\partial t} + \nabla \cdot (\rho_0 \mathbf{v}') + \nabla \cdot (\rho' \mathbf{v}_0) = \frac{D_0 \rho'}{Dt} + \rho' \nabla \cdot \mathbf{v}_0 + \nabla \cdot (\rho_0 \mathbf{v}') = 0, \quad (2.72)$$

$$\begin{aligned} \rho_0 \frac{\partial \mathbf{v}'}{\partial t} + \rho_0 \mathbf{v}_0 \cdot \nabla \mathbf{v}' + \rho_0 \mathbf{v}' \cdot \nabla \mathbf{v}_0 + \rho' \mathbf{v}_0 \cdot \nabla \mathbf{v}_0 + \nabla p' \\ = \rho_0 \frac{D_0 \mathbf{v}'}{Dt} + \rho_0 \mathbf{v}' \cdot \nabla \mathbf{v}_0 + \rho' \mathbf{v}_0 \cdot \nabla \mathbf{v}_0 + \nabla p' = 0, \end{aligned} \quad (2.73)$$

$$\begin{aligned} \frac{\partial p'}{\partial t} + \mathbf{v}_0 \cdot \nabla p' + \mathbf{v}' \cdot \nabla p_0 + \rho_0 c_0^2 \nabla \cdot \mathbf{v}' + \rho_0 (c^2)' \nabla \cdot \mathbf{v}_0 + \rho' c_0^2 \nabla \cdot \mathbf{v}_0 \\ = \frac{D_0 p'}{Dt} + \mathbf{v}' \cdot \nabla p_0 + \rho_0 c_0^2 \nabla \cdot \mathbf{v}' + \rho_0 (c^2)' \nabla \cdot \mathbf{v}_0 + \rho' c_0^2 \nabla \cdot \mathbf{v}_0 = 0, \end{aligned} \quad (2.74)$$

where  $D_0/Dt = \partial/\partial t + \mathbf{v}_0 \cdot \nabla$  is the total derivative with regard to the mean flow velocity<sup>3</sup>.

The last equation can be further simplified for a perfect gas. In such a case, the equation (2.34) reads:

$$\mathcal{p} = \rho c^2, \quad (2.75)$$

or, after the introduction of the steady flow and perturbation split:

---

<sup>3</sup> After the linearization is applied, the mean flow quantities become entirely equal to the corresponding quantities of the steady flow component. Therefore, for velocity:  $\mathbf{v}_0(\mathbf{x}) = \overline{\mathbf{v}(\mathbf{x}, t)}$ .

$$\gamma p_0 + \gamma p' = \rho_0 c_0^2 + \rho_0 (c^2)' + \rho' c_0^2 + \rho' (c^2)'. \quad (2.76)$$

Subtracting the steady flow equation (2.45),  $\rho_0 c_0^2 = \gamma p_0$ , and omitting the last term (linearization) gives:

$$\gamma p' = \rho_0 (c^2)' + \rho' c_0^2. \quad (2.77)$$

Inserting this into the equation (2.74) gives:

$$\begin{aligned} \frac{\partial p'}{\partial t} + \mathbf{v}_0 \cdot \nabla p' + \mathbf{v}' \cdot \nabla p_0 + \gamma p_0 \nabla \cdot \mathbf{v}' + \gamma p' \nabla \cdot \mathbf{v}_0 \\ = \frac{D_0 p'}{Dt} + \mathbf{v}' \cdot \nabla p_0 + \gamma p_0 \nabla \cdot \mathbf{v}' + \gamma p' \nabla \cdot \mathbf{v}_0 = 0. \end{aligned} \quad (2.78)$$

The obtained Linearized Euler Equations, (2.72)-(2.74) or for a perfect gas (2.72), (2.73), and (2.78), are in the primitive form and contain the classical, not necessarily conserved quantities (density, velocity, and pressure). The conservative form of the equations can also be obtained, such as in [Ham16, HGB16]. The advantage of using the conserved quantities<sup>4</sup> (mass, momentum, and energy), rather than the primitive ones is that the obtained Linearized Euler Equations do not contain spatial derivatives of the steady quantities, which is not the case with the equations derived above. This allows more efficient and accurate numerical algorithms, since no particular calculation over the mean flow quantities is necessary within the acoustic calculations. In particular, the momentum equation involves the first-order momentum perturbation as its main unknown, which equals:  $(\rho \mathbf{v})' = \rho_0 \mathbf{v}' + \rho' \mathbf{v}_0$ . With regard to that, the mass equation (2.72) can be written straightforwardly as:

$$\frac{\partial \rho'}{\partial t} + \nabla \cdot (\rho \mathbf{v})' = 0, \quad (2.79)$$

with the unknowns  $\rho'$  and  $(\rho \mathbf{v})'$ .

Next, we want to turn the pressure equation for a perfect gas (2.78) into the form of a conservation law:

$$\begin{aligned} \frac{\partial p_c'}{\partial t} + \nabla \cdot (\mathbf{v} p_c)' &= \frac{\partial p_c'}{\partial t} + \nabla \cdot (\mathbf{v}_0 p_c' + \mathbf{v}' p_{c0}) \\ &= \frac{\partial p_c'}{\partial t} + \mathbf{v}_0 \cdot \nabla p_c' + \mathbf{v}' \cdot \nabla p_{c0} + p_{c0} \nabla \cdot \mathbf{v}' + p_c' \nabla \cdot \mathbf{v}_0 = 0, \end{aligned} \quad (2.80)$$

---

<sup>4</sup> In fact, their volume densities in the differential form of the equations.

with the main pressure-related variable split into its steady and unsteady component as  $p_c = p_{c0}(p_0) + p_c'(p_0, p')$ . We also assume small unsteady perturbations around

the steady value, that is,  $p_c' \ll p_{c0}$ . Since the following also hold:  $\frac{\partial p_c'}{\partial t} = \frac{\partial p_c'}{\partial p'} \frac{\partial p'}{\partial t}$ ,

$\nabla p_{c0} = \frac{dp_{c0}}{dp_0} \nabla p_0$ , and  $\nabla p_c' = \frac{\partial p_c'}{\partial p_0} \nabla p_0 + \frac{\partial p_c'}{\partial p'} \nabla p'$ , according to the chain rule, the

equation (2.80) becomes:

$$\begin{aligned} \frac{\partial p_c'}{\partial p'} \frac{\partial p'}{\partial t} + \frac{\partial p_c'}{\partial p_0} \mathbf{v}_0 \cdot \nabla p_0 + \frac{\partial p_c'}{\partial p'} \mathbf{v}_0 \cdot \nabla p' + \frac{dp_{c0}}{dp_0} \mathbf{v}' \cdot \nabla p_0 + p_{c0} \nabla \cdot \mathbf{v}' \\ + p_c' \nabla \cdot \mathbf{v}_0 = 0. \end{aligned} \quad (2.81)$$

Conservation of energy of an inviscid perfect gas without heat conduction or sources of mass or heat (equations (2.48) and (2.49) for an isentropic steady flow) gives the following relation between the steady quantities:

$$\mathbf{v}_0 \cdot \nabla p_0 = -c_0^2 \rho_0 \nabla \cdot \mathbf{v}_0 = -\mathcal{P}_0 \nabla \cdot \mathbf{v}_0. \quad (2.82)$$

Inserting this into the equation (2.81) gives:

$$\frac{\partial p_c'}{\partial p'} \frac{\partial p'}{\partial t} + \left( p_c' - \mathcal{P}_0 \frac{\partial p_c'}{\partial p_0} \right) \nabla \cdot \mathbf{v}_0 + \frac{\partial p_c'}{\partial p'} \mathbf{v}_0 \cdot \nabla p' + \frac{dp_{c0}}{dp_0} \mathbf{v}' \cdot \nabla p_0 + p_{c0} \nabla \cdot \mathbf{v}' = 0. \quad (2.83)$$

Comparison of the last equation with the corresponding one, equation (2.78), multiplied with  $\partial p_c' / \partial p'$ :

$$\frac{\partial p_c'}{\partial p'} \frac{\partial p'}{\partial t} + \frac{\partial p_c'}{\partial p'} \mathbf{v}_0 \cdot \nabla p' + \frac{\partial p_c'}{\partial p'} \mathbf{v}' \cdot \nabla p_0 + \mathcal{P}_0 \frac{\partial p_c'}{\partial p'} \nabla \cdot \mathbf{v}' + \mathcal{P}' \frac{\partial p_c'}{\partial p'} \nabla \cdot \mathbf{v}_0 = 0, \quad (2.84)$$

implies that the following expressions have to be satisfied<sup>5</sup>:

$$p_c' - \mathcal{P}_0 \frac{\partial p_c'}{\partial p_0} = \mathcal{P}' \frac{\partial p_c'}{\partial p'}, \quad (2.85)$$

$$\frac{dp_{c0}}{dp_0} = \frac{\partial p_c'}{\partial p'}, \text{ and} \quad (2.86)$$

$$p_{c0} = \mathcal{P}_0 \frac{\partial p_c'}{\partial p'}. \quad (2.87)$$

---

<sup>5</sup> It is interesting to note that small perturbation of Phillips' quantity [Phi60], which will be introduced later,  $\Pi' = p' / (\mathcal{P}_0)$  does not satisfy the last expression whenever the steady value

$\Pi_0 = \frac{1}{\gamma} \ln \left( \frac{p_0}{p_\infty} \right) \neq 1$ , that is, whenever  $p_0 \neq e^\gamma p_\infty$ , which is in general true.

From the last expression, we find:

$$p_c' = \frac{P_{c0}}{\mathcal{P}_0} p' + f(p_0) \quad (2.88)$$

and inserting this into the expression (2.85):

$$\begin{aligned} \frac{P_{c0}}{P_0} p' &= p_c' - \mathcal{P}_0 \frac{\partial p_c'}{\partial p_0} = \frac{P_{c0}}{\mathcal{P}_0} p' + f(p_0) \\ &\quad - \mathcal{P}_0 \left( \frac{P_{c0}}{\mathcal{P}_0} \underbrace{\frac{\partial p'}{\partial p_0}}_{=0} + \frac{p'}{\gamma} \frac{d}{dp_0} \left( \frac{P_{c0}}{P_0} \right) + \frac{df(p_0)}{dp_0} \right) \\ &= \frac{P_{c0}}{\mathcal{P}_0} p' + f(p_0) - P_0 p' \frac{d}{dp_0} \left( \frac{P_{c0}}{P_0} \right) - \mathcal{P}_0 \frac{df(p_0)}{dp_0}, \end{aligned} \quad (2.89)$$

which leads to the further two expressions:

$$f(p_0) - \mathcal{P}_0 \frac{df(p_0)}{dp_0} = 0 \quad \text{and} \quad (2.90)$$

$$\frac{P_{c0}}{P_0} = \frac{P_{c0}}{\mathcal{P}_0} - P_0 \frac{d}{dp_0} \left( \frac{P_{c0}}{P_0} \right) = \frac{P_{c0}}{\mathcal{P}_0} - \frac{dp_{c0}}{dp_0} + \frac{P_{c0}}{P_0} \Rightarrow \frac{dp_{c0}}{dp_0} = \frac{P_{c0}}{\mathcal{P}_0}. \quad (2.91)$$

Incidentally, the latter expression of the two also follows from the expressions (2.86) and (2.87) combined. In fact, it is a first-order ordinary differential equation, which can be solved with the separation of variables to obtain:

$$\int \frac{dp_{c0}}{P_{c0}} = \int \frac{dp_0}{\mathcal{P}_0} \Rightarrow p_{c0} = (C_1 p_0)^{1/\gamma}, \quad (2.92)$$

with an arbitrary constant  $C_1$ . If we set  $C_1 = 1/p_\infty$ , where  $p_\infty$  is some constant reference value of pressure (for example, static pressure in still air,  $p_\infty \approx 101\text{kPa}$ ), non-dimensional quantity  $p_c$  can be interpreted as normalized pressure.

On the other hand, the former expression gives the same type of the ordinary differential equation:

$$f(p_0) - \mathcal{P}_0 \frac{df(p_0)}{dp_0} = 0 \Rightarrow \frac{df(p_0)}{f(p_0)} = \frac{dp_0}{\mathcal{P}_0}, \quad (2.93)$$

with the solution  $f(p_0) = (C_2 p_0)^{1/\gamma}$ , with an arbitrary constant  $C_2$ .

Therefore, from the equations (2.92) and (2.88) it follows:  $p_{c0} = (C_1 p_0)^{1/\gamma}$  and

$p_c' = \frac{P_{c0}}{\mathcal{P}_0} p' + (C_2 p_0)^{1/\gamma}$ , which determines the total quantity  $p_c = p_{c0} + p_c'$ . Since we

want the perturbation part  $p_c'$  to have a zero time-averaged value, we choose  $C_2 = 0$ .

Finally, we can also confirm that  $p_c' = \frac{p_{c0}}{\mathcal{P}_0} p' \ll p_{c0}$  for any  $p_{c0} \neq 0$  and  $p' \ll p_0$ ,

which is satisfied for small pressure perturbations, as assumed within the derivation of the linearized equations.

The momentum equation in the conservative form follows from the sum of its primitive form (2.73) and the product of the mass equation (2.79) with the steady component of the velocity vector  $\mathbf{v}_0$ :

$$\begin{aligned}
& \rho_0 \frac{\partial \mathbf{v}'}{\partial t} + \rho_0 \mathbf{v}_0 \cdot \nabla \mathbf{v}' + \rho_0 \mathbf{v}' \cdot \nabla \mathbf{v}_0 + \rho' \mathbf{v}_0 \cdot \nabla \mathbf{v}_0 + \nabla p' + \mathbf{v}_0 \frac{\partial \rho'}{\partial t} + \mathbf{v}_0 \nabla \cdot (\rho \mathbf{v})' \\
&= \frac{\partial (\rho \mathbf{v})'}{\partial t} + \rho_0 \mathbf{v}_0 \cdot \nabla \mathbf{v}' + (\rho \mathbf{v})' \cdot \nabla \mathbf{v}_0 + \nabla p' + \mathbf{v}_0 \nabla \cdot (\rho \mathbf{v})' \\
&= \frac{\partial (\rho \mathbf{v})'}{\partial t} + \nabla \cdot (\rho_0 \mathbf{v}_0 \mathbf{v}') - \underbrace{\mathbf{v}' \cdot \nabla \cdot (\rho_0 \mathbf{v}_0)}_{=0} + \nabla \cdot [(\rho \mathbf{v})' \mathbf{v}_0] + \nabla \left( \frac{\mathcal{P}_0}{p_{c0}} \frac{p_{c0}}{\mathcal{P}_0} p' \right) \\
&= \frac{\partial (\rho \mathbf{v})'}{\partial t} + \nabla \cdot (\rho \mathbf{v} \mathbf{v})' + \nabla \left( \frac{\mathcal{P}_0}{p_{c0}} p_c' \right) = 0,
\end{aligned} \tag{2.94}$$

where the last equality follows from the mass equation of a steady isentropic flow, equation (2.46), and the fact that  $(\rho \mathbf{v} \mathbf{v})' = \rho_0 \mathbf{v}_0 \mathbf{v}' + \rho_0 \mathbf{v}' \mathbf{v}_0 + \rho' \mathbf{v}_0 \mathbf{v}_0 = \rho_0 \mathbf{v}_0 \mathbf{v}' + (\rho \mathbf{v})' \mathbf{v}_0$ .

The linearized conservative forms of the mass and momentum equations could also be obtained directly from the conservation laws (2.1) and (2.2), respectively, simply by choosing the first-order perturbations of all the terms in the equations and suppressing viscosity and the external sources. This is due to the fact that within the linear approximation, time-averaged (mean) flow is equal to the steady flow.

Therefore, the full system of Linearized Euler Equations in the conservative form reads:

$$\frac{\partial \rho'}{\partial t} + \nabla \cdot (\rho \mathbf{v})' = 0, \tag{2.95}$$

$$\frac{\partial (\rho \mathbf{v})'}{\partial t} + \nabla \cdot (\rho \mathbf{v} \mathbf{v})' + \nabla \left( \frac{\mathcal{P}_0}{p_{c0}} p_c' \right) = 0, \text{ and} \tag{2.96}$$

$$\frac{\partial p_c'}{\partial t} + \nabla \cdot (p_c \mathbf{v})' = 0. \tag{2.97}$$

It should be underlined once again that the derived Linearized Euler Equations describe any small and inviscid unsteady perturbation of the mean flow of a perfect gas, when heat conduction is negligible and no external sources are present. This statement has several further implications. Firstly, the solution of the equations can involve any type of the flow perturbations, acoustic (sound waves), as well as non-acoustic (vorticity and entropy) modes. As a result, the separation between acoustic and non-acoustic perturbations can be difficult in turbulent flows, as well as when sound waves interact with the vortical flow established at the trailing edge of an open unflanged pipe. Inability to distinguish between different modes of perturbations means that the estimation of actual sound field can be considerably distorted (amplified or cancelled) by the localized unsteady, but essentially incompressible non-acoustic (often called “pseudo-sound”) fluctuations, which do not contribute to the far-field radiation, nor propagate at the speed of sound. This problem will be further treated in the following.

Secondly, the linearization is based on the assumption that all the perturbations have small amplitudes compared to the steady values. This is most often the case with sound waves at reasonably high sound pressure levels, below 150dB, when the amplitudes of acoustic pressure perturbations are at least two orders of magnitude smaller than the static value of pressure in motionless air, since  $SPL = 20 \log_{10}(0.01 \cdot 101000 \text{Pa} / 2 \cdot 10^{-5} \text{Pa}) \approx 154 \text{dB}$ . The equations are, therefore, very well-suited for solving the problems of acoustic propagation [HRD11, DIA12, HGB16], but not necessarily for other types of perturbations, such as in essentially non-linear turbulent flows. In the latter case, the amplitudes of unsteady components can be of the same order of magnitude as the values of the corresponding steady components. Consequently, Linearized Euler Equations are well suited for estimation of (low amplitude) sound propagation, but not for the characterization of non-linear flow-induced (aeroacoustic) sources. However, such sources of sound are not considered in this work.

Lastly, neglecting viscosity effects means that the derived equations are not suitable for viscosity-dominated problems, such as within boundary layers or very narrow tubes. Moreover, the vorticity modes, which are undamped due to the lack of

viscosity, although linear, can grow to infinity and present potential instability of the solution. This issue can be dealt with, for example, by using more general linearized Navier-Stokes equations or, more frequently, by adding an artificial damping or filtering out the growing instabilities from the solution. The latter approach will be taken in Chapter VI for the numerical solution of Linearized Euler Equations.

Further simplification of Linearized Euler Equations towards more accurate and efficient extraction of sound field necessarily involves additional approximations or models of the flow. Some common steps in this direction are discussed below.

## 2.5 Wave equation and convected wave equation

Two approximations commonly adopted in classical acoustics are those of a uniform flow and motionless, still medium (no-flow case). If the flow is uniform,  $\rho_0$ ,  $\mathbf{v}_0$ ,  $p_0$ , and  $c_0^2$  are constants in both space and time and the Linearized Euler Equations (2.72)-(2.74) simplify to:

$$\frac{D_0 \rho'}{Dt} + \rho_0 \nabla \cdot \mathbf{v}' = 0, \quad (2.98)$$

$$\rho_0 \frac{D_0 \mathbf{v}'}{Dt} + \nabla p' = 0, \text{ and} \quad (2.99)$$

$$\frac{D_0 p'}{Dt} + \rho_0 c_0^2 \nabla \cdot \mathbf{v}' = 0. \quad (2.100)$$

We can multiply the first equation with  $c_0^2$  and compare it with the last one to conclude that in such flows:

$$\frac{D_0}{Dt} (p' - c_0^2 \rho') = 0. \quad (2.101)$$

Moreover, we can take the total derivative  $D_0/Dt$  of the equation (2.100) divided with  $c_0^2$  and subtract the divergence of the equation (2.99) from it to obtain:

$$\begin{aligned}
& \frac{1}{c_0^2} \frac{D_0^2 p'}{Dt^2} + \rho_0 \frac{D_0}{Dt} \nabla \cdot \mathbf{v}' - \rho_0 \nabla \cdot \frac{D_0 \mathbf{v}'}{Dt} - \underbrace{\nabla \cdot \nabla p'}_{=\nabla^2 p' = \Delta p} \\
&= \frac{1}{c_0^2} \frac{D_0^2 p'}{Dt^2} + \rho_0 \frac{\partial}{\partial t} \nabla \cdot \mathbf{v}' + \rho_0 \mathbf{v}_0 \cdot \nabla \nabla \cdot \mathbf{v}' - \rho_0 \nabla \cdot \frac{\partial \mathbf{v}'}{\partial t} - \rho_0 \nabla \cdot (\mathbf{v}_0 \cdot \nabla \mathbf{v}') - \nabla \cdot \nabla p' \quad (2.102) \\
&= \frac{1}{c_0^2} \frac{D_0^2 p'}{Dt^2} + \rho_0 \mathbf{v}_0 \cdot \nabla \nabla \cdot \mathbf{v}' - \rho_0 \nabla \cdot (\mathbf{v}_0 \cdot \nabla \mathbf{v}') - \nabla \cdot \nabla p' = 0.
\end{aligned}$$

After noticing that:

$$\begin{aligned}
\nabla \cdot (\mathbf{v}_0 \cdot \nabla \mathbf{v}') &= \frac{\partial}{\partial x_i} v_{0j} \frac{\partial v'_i}{\partial x_j} = v_{0j} \frac{\partial}{\partial x_i} \frac{\partial v'_i}{\partial x_j} \\
&= \mathbf{v}_0 \cdot \nabla \cdot \nabla \mathbf{v}' = \mathbf{v}_0 \cdot (\nabla \nabla \cdot \mathbf{v}' - \nabla \times \nabla \times \mathbf{v}'), \quad (2.103)
\end{aligned}$$

the equation (2.102) becomes:

$$\frac{1}{c_0^2} \frac{D_0^2 p'}{Dt^2} + \rho_0 \mathbf{v}_0 \cdot \nabla \times \nabla \times \mathbf{v}' - \nabla \cdot \nabla p' = 0. \quad (2.104)$$

According to the Helmholtz theorem, all sufficiently smooth vector fields can be represented as a sum of a zero-divergence (solenoidal) component and a zero-curl (irrotational) component. The velocity perturbation vector can then be decomposed as:  $\mathbf{v}' = \mathbf{v}'_{sol} + \mathbf{v}'_{irr}$ , with  $\nabla \cdot \mathbf{v}'_{sol} = 0$  and  $\nabla \times \mathbf{v}'_{irr} = 0$ . Correspondingly, we can conveniently introduce two components of the pressure perturbation which are attributed to the two velocity components, that is:  $p' = p'_{sol} + p'_{irr}$ . The last equation is, thus, split into two:

$$\frac{1}{c_0^2} \frac{D_0^2 p'_{sol}}{Dt^2} + \rho_0 \mathbf{v}_0 \cdot \nabla \times \nabla \times \mathbf{v}'_{sol} - \nabla \cdot \nabla p'_{sol} = 0 \quad \text{and} \quad (2.105)$$

$$\frac{1}{c_0^2} \frac{D_0^2 p'_{irr}}{Dt^2} - \nabla \cdot \nabla p'_{irr} = 0. \quad (2.106)$$

On the other hand, we can split the equation (2.98) and the density perturbation to obtain:

$$\frac{D_0 \rho'_{sol}}{Dt} = 0 \quad \text{and} \quad (2.107)$$

$$\frac{D_0 \rho'_{irr}}{Dt} + \rho_0 \nabla \cdot \mathbf{v}'_{irr} = 0, \quad (2.108)$$

where  $\rho'_{sol}$  and  $\rho'_{irr}$  correspond also to  $p'_{sol}$  and  $p'_{irr}$ , respectively due to the equation (2.101).

Similarly as the equation (2.5), the equation (2.107) is a transport partial differential equation (of an incompressible flow, since the unknown is density), with the general solution in the form of a plane wave propagating in the direction  $\mathbf{n}$ , with the velocity  $\mathbf{v}_0 = v_0 \mathbf{n}$ . Obviously, this solution cannot represent an acoustic wave, which propagates with the speed  $c_0$  and acoustic waves have to be associated with compressible irrotational velocity perturbations<sup>6</sup>, that is,  $p'_{ac} = p'_{irr}$ . The acoustic convected wave equation, therefore, has the same form as the equation (2.106):

$$\frac{1}{c_0^2} \frac{D_0^2 p'_{ac}}{Dt^2} - \nabla \cdot \nabla p'_{ac} = 0. \quad (2.109)$$

Moreover, since the following scaling holds for acoustic waves:  $\partial/\partial t \sim \omega$  and  $\nabla \sim k = \omega/c_0$ , the equation (2.101) will be satisfied in subsonic flows with  $v_0 \ll c_0$  only if  $p' - c_0^2 \rho' = 0$ .

In the no-flow case, that is, in a quiescent fluid (uniform and stagnant fluid in which  $\mathbf{v}_0 = 0$  and  $D_0/Dt = \partial/\partial t$ ), the convected wave equation simplifies to the classical acoustic wave equation:

$$\frac{1}{c_0^2} \frac{\partial^2 p'_{ac}}{\partial t^2} - \nabla \cdot \nabla p'_{ac} = 0. \quad (2.110)$$

The relation (2.101) also simplifies to:

$$\frac{\partial}{\partial t} (p' - c_0^2 \rho') = 0, \quad (2.111)$$

from which it follows again:

$$p' = c_0^2 \rho'. \quad (2.112)$$

Moreover, Linearized Euler Equations (2.98)-(2.100) are simplified to:

$$\frac{\partial \rho'}{\partial t} + \rho_0 \nabla \cdot \mathbf{v}' = 0, \quad (2.113)$$

$$\rho_0 \frac{\partial \mathbf{v}'}{\partial t} + \nabla p' = 0, \text{ and} \quad (2.114)$$

---

<sup>6</sup> The incompressible solenoidal component of the pressure perturbation,  $p'_{sol}$ , is often called “pseudo-sound”.

$$\frac{\partial p'}{\partial t} + \rho_0 c_0^2 \nabla \cdot \mathbf{v}' = 0, \quad (2.115)$$

where the first and the third equations are related through the equation (2.112). If we again apply Helmholtz decomposition, we see that  $\frac{\partial \rho'_{sol}}{\partial t} = 0$ ,  $\frac{\partial p'_{sol}}{\partial t} = 0$ , and, therefore,  $\frac{\partial \mathbf{v}'_{sol}}{\partial t} = 0$ , so the solenoidal perturbations vanish and the acoustic waves constitute the only unsteady (compressible) perturbations of otherwise still fluid. In other words, Linearized Euler Equations in a quiescent fluid describe only the acoustic propagation.

Both acoustic wave and convected wave equation have an analytical solution in the form of Green's functions [Del14]. However, in more general, non-uniform flows, when the relation (2.101) does not hold, the split between acoustic and non-acoustic perturbations is not straightforward. This becomes especially important whenever an unsteady solenoidal flow interacts with the irrotational acoustic field. One such example, which will be in the focus of this work, is the interaction between the incoming acoustic wave and the vorticity at the trailing edge of an open pipe. Nevertheless, since low-amplitude sound propagation is to be considered, linearized equations suffice. Another field of acoustics which particularly deals with sound generation due to essentially non-linear flows is aeroacoustics. Its main goal is to identify and quantify the physical mechanisms of sound generation in unsteady flows, accompanied by the estimation of acoustic wave propagation. In an ideal case, a so-called aeroacoustic analogy results in a single equation, the left-hand side of which contains a single acoustic unknown (for example,  $p'_{ac}$  from above) and the right-hand side contains only the flow-related source terms, which are considered to be known prior to the estimation of acoustic propagation. In the following, we will consider several important aeroacoustic analogies, which can also be relevant for the problem of sound radiation outside an open pipe with a sharp trailing edge in an inhomogeneous medium.

## 2.6 Aeroacoustic analogies

In this chapter, several aeroacoustic analogies are considered, which might be relevant for the estimation of sound radiation from an open pipe with a non-uniform mean flow. Although this work primarily deals with the sound propagation outside the pipe, the main concepts and results of aeroacoustic analogies should shed more light on the vortex-sound interaction which takes place at the pipe's trailing edge. Conversely, accurate aeroacoustic calculations should also capture the propagation effects, in order to provide a good estimation of the resulting acoustic field. Therefore, the conclusions derived in this chapter and the rest of the work might as well be suitable for efficient calculations in a more general case when aeroacoustic sources are present inside the flow.

### 2.6.1 Lighthill's equation

Chronologically the first, most important, and easiest to derive is Lighthill's aeroacoustic analogy. The key idea of Lighthill's celebrated work [Lig52] is to start with the governing equations of fluid dynamics and derive a single equation which should describe the acoustic field in an arbitrary flow of fluid. The differential operator on the left-hand side of this equation is analogous to the classical wave equation (therefore, the equation is called analogy), while its right-hand side is interpreted to describe aeroacoustic sources of sound (hence, the aeroacoustic analogy).

Lighthill's aeroacoustic analogy is easily derived in the following way. We subtract the divergence of the momentum equation (2.2) from the time derivative of the mass equation (2.1) to obtain:

$$\frac{\partial^2 \rho}{\partial t^2} - \nabla \cdot \nabla \cdot (\rho \mathbf{v} \mathbf{v}) - \nabla \cdot \nabla p + \nabla \cdot \nabla \cdot \boldsymbol{\tau} = \frac{\partial m}{\partial t} - \nabla \cdot (m \mathbf{v} + \mathbf{f}). \quad (2.116)$$

In order to come up with the classical wave equation operator on the left-hand side of the equation with pressure as the unknown, we add  $\partial^2 p / c_\infty^2 \partial t^2$  to the both sides of the equation and rearrange the terms:

$$\frac{1}{c_\infty^2} \frac{\partial^2 p}{\partial t^2} - \nabla \cdot \nabla p = \frac{\partial m}{\partial t} - \nabla \cdot (m\mathbf{v} + \mathbf{f}) + \nabla \cdot \nabla \cdot (\rho\mathbf{v}\mathbf{v} - \tau) + \frac{\partial^2}{\partial t^2} \left( \frac{p}{c_\infty^2} - \rho \right). \quad (2.117)$$

Here,  $c_\infty^2$  is a constant reference value, which, for convenience, can be equal to  $c_0^2$  at infinity, where the mean flow is assumed to be uniform. In a similar way, the wave equation for density as the unknown can be derived by subtracting  $c_\infty^2 \nabla \cdot \nabla \rho$  from the two sides of the equation (2.116) and rearranging the terms as:

$$\frac{\partial^2 \rho}{\partial t^2} - c_\infty^2 \nabla \cdot \nabla \rho = \frac{\partial m}{\partial t} - \nabla \cdot (m\mathbf{v} + \mathbf{f}) + \nabla \cdot \nabla \cdot (\rho\mathbf{v}\mathbf{v} - \tau) + \nabla \cdot \nabla (p - c_\infty^2 \rho). \quad (2.118)$$

For the corresponding perturbations around the constant reference values,  $p' = p - p_\infty$  and  $\rho' = \rho - \rho_\infty$ , the equations become, respectively:

$$\frac{1}{c_\infty^2} \frac{\partial^2 p'}{\partial t^2} - \nabla \cdot \nabla p' = \frac{\partial m}{\partial t} - \nabla \cdot (m\mathbf{v} + \mathbf{f}) + \nabla \cdot \nabla \cdot (\rho\mathbf{v}\mathbf{v} - \tau) + \frac{\partial^2}{\partial t^2} \left( \frac{p'}{c_\infty^2} - \rho' \right) \text{ and} \quad (2.119)$$

$$\frac{\partial^2 \rho'}{\partial t^2} - c_\infty^2 \nabla \cdot \nabla \rho' = \frac{\partial m}{\partial t} - \nabla \cdot (m\mathbf{v} + \mathbf{f}) + \nabla \cdot \nabla \cdot (\rho\mathbf{v}\mathbf{v} - \tau) + \nabla \cdot \nabla (p' - c_\infty^2 \rho'). \quad (2.120)$$

However, such perturbations represent pure acoustic waves only in a quiescent fluid, when  $p_0 = p_\infty$  and  $\rho_0 = \rho_\infty$  everywhere. In other words, Lighthill's aeroacoustic analogy assumes quiescent fluid as a "reference flow" in which acoustic perturbations occur. Consequently, the equation is not suitable for the extraction of the sound field in any part of the fluid which is not quiescent.

The derived equations (2.117)-(2.120) are exact and hold for an arbitrary flow, but, consequently, they are not easier to solve than any other governing equation of the flow. Nevertheless, their forms allow very elegant solution of the acoustic field if some additional approximations of the source terms on the right-hand side can be utilized, that is, if the (aero)acoustic sources can be modelled. One such example is a free jet (jet in a free space filled with a quiescent fluid), which was treated by Lighthill himself and which indicates the quadrupole nature of the aeroacoustic sources [Lig52]. However, it is well known from experience that a solid body inside an unsteady flow can substantially amplify the aerodynamically generated noise. With regard to that, different generalizations of the analogy appeared soon after Lighthill introduced his equation, with the aim to take into account the usual presence of a solid

body inside the flow and its effects on both the efficiency of the aerodynamic noise generation and the far-field propagation and the directivity of such sources. The most prominent formulations were proposed by Curle [Cur55], for a motionless body, and Ffowcs Williams and Hawkings [FH69], for a body in motion. Both generalizations have found many engineering applications, especially in aerospace industry [Loc00, BF03, RRV14, PKJ+11]. Still, the applications are most often limited to low Mach number flows, since the estimation of aeroacoustic sources at higher flow velocities becomes increasingly involved.

Another important limitation of Lighthill's analogy, which is in the basis of both later generalizations, is in the physical mistreatment of all sound propagation phenomena which take place in moving and inhomogeneous media [De14], that is, in all non-quiescent fluids. By forcing the wave operator on the left-hand side of the equation to match the one in the classical wave equation in quiescent fluids, Lighthill's analogy treats all propagation terms as artificial, spatially distributed sources contained on the right-hand side of the equation. These additional sources should also be resolved in order to estimate the far-field sound radiation accurately. This has lead several authors to propose different formulations of the aeroacoustic analogy, within the attempts to separate true aeroacoustic sources and sound propagation terms. Among the most notable ones are Phillips' [Phi60] and Lilley's [Li74] equations. Both equations inevitably contain more complex wave operators compared to the Lighthill's one, without associated Green's functions, apart from some highly idealized cases, such as a uniform mean flow. In particular, Lilley's equation involves the third-order wave operator, which also supports unstable, purely hydrodynamic vortical modes as a part of the solution [Mus07]. Nevertheless, both formulations are nowadays quite easily solved numerically [ASL96, IKP06], with the required computational efforts much smaller than for the calculation of the distributed artificial sources in Lighthill's equation.

Since the problem of sound radiation from a pipe with a hot mean flow involves both a solid body inside the flow and an inhomogeneous medium, the rest of the chapter briefly describes free-space Phillips' equation suitable for inhomogeneous flows, as well as Ffowcs Williams and Hawkings equation for a body in a flow. It should be mentioned that Lilley's equation is exact aeroacoustic analogy, which ideally

separates the aeroacoustic sources and propagation terms for parallel (shear) mean flows, such as jets exhausted from circular pipes [Gol76]. Nevertheless, due to the complexity of the third-order differential operator, which is commonly accepted only in the particular case of shear flows, Lilley's equation will not be treated in this work. The emphasis will rather be on simpler, computationally less demanding and more robust second-order (convected) wave equations, bearing in mind the possibilities for their applications beyond the case study of this work.

### 2.6.2 Phillips' equation

The starting equations are the conservation of momentum (2.8):

$$\frac{D\mathbf{v}}{Dt} + \frac{\nabla p}{\rho} - \frac{\nabla \cdot \boldsymbol{\tau}}{\rho} = \frac{\mathbf{f}}{\rho} \quad (2.121)$$

and the combination of the energy equation and the equation of state, (2.26):

$$\frac{1}{\rho c^2} \frac{Dp}{Dt} + \nabla \cdot \mathbf{v} = \frac{m}{\rho} + \sigma \frac{Ds}{Dt}. \quad (2.122)$$

For convenience, a new variable is introduced, defined with:

$$\Pi = \ln \left( \frac{p}{p_\infty} \right)^{1/\gamma}, \quad (2.123)$$

where  $\gamma$  is the heat capacity ratio. In a perfect gas, the equation (2.34) holds,  $\gamma p = \rho c^2$ , so the variable  $\Pi$  satisfies the following relations:

$$\nabla \Pi = \frac{1}{\gamma} \nabla \ln \left( \frac{p}{p_\infty} \right) = \frac{1}{\gamma} \frac{p_\infty}{p} \frac{1}{p_\infty} \nabla p = \frac{1}{\rho c^2} \nabla p \quad (2.124)$$

and similarly

$$\frac{D\Pi}{Dt} = \frac{1}{\rho c^2} \frac{Dp}{Dt}. \quad (2.125)$$

Therefore, we can write the equations (2.121) and (2.122) in a slightly more compact form as, respectively:

$$c^2 \nabla \Pi = \frac{\mathbf{f}}{\rho} - \frac{D\mathbf{v}}{Dt} + \frac{\nabla \cdot \boldsymbol{\tau}}{\rho} \quad \text{and} \quad (2.126)$$

$$\frac{D\Pi}{Dt} = \frac{m}{\rho} + \sigma \frac{Ds}{Dt} - \nabla \cdot \mathbf{v}. \quad (2.127)$$

We subtract the divergence of the first equation from the total derivative of the second equation and obtain:

$$\frac{D^2\Pi}{Dt^2} - \nabla \cdot (c^2 \nabla \Pi) = \frac{D}{Dt} \left( \frac{m}{\rho} + \sigma \frac{Ds}{Dt} - \nabla \cdot \mathbf{v} \right) - \nabla \cdot \left( \frac{\mathbf{f}}{\rho} - \frac{D\mathbf{v}}{Dt} + \frac{\nabla \cdot \boldsymbol{\tau}}{\rho} \right). \quad (2.128)$$

After noticing that:

$$\begin{aligned} \nabla \cdot \left( \frac{D\mathbf{v}}{Dt} \right) - \frac{D}{Dt} (\nabla \cdot \mathbf{v}) &= \nabla \cdot \frac{\partial \mathbf{v}}{\partial t} + \nabla \cdot (\mathbf{v} \cdot \nabla \mathbf{v}) - \frac{\partial}{\partial t} (\nabla \cdot \mathbf{v}) - \mathbf{v} \cdot \nabla \nabla \cdot \mathbf{v} \\ &= \nabla \cdot (\mathbf{v} \cdot \nabla \mathbf{v}) - \mathbf{v} \cdot \nabla \nabla \cdot \mathbf{v}, \end{aligned} \quad (2.129)$$

the equation becomes:

$$\begin{aligned} \frac{D^2\Pi}{Dt^2} - \nabla \cdot (c^2 \nabla \Pi) &= \frac{D}{Dt} \left( \frac{m}{\rho} \right) - \nabla \cdot \left( \frac{\mathbf{f} + \nabla \cdot \boldsymbol{\tau}}{\rho} \right) + \sigma \frac{D^2 s}{Dt^2} \\ &\quad + \nabla \cdot (\mathbf{v} \cdot \nabla \mathbf{v}) - \mathbf{v} \cdot \nabla \nabla \cdot \mathbf{v} \end{aligned} \quad (2.130)$$

In the absence of mass and force sources and with negligible viscosity, the right-hand side of the equation contains purely kinematic sources (the last two terms) and the sources due to the change of entropy. The latter ones vanish in isentropic flows, if there are no heat sources and if heat conduction is negligible, according to the equation (2.24).

The variable  $\Pi$  can be associated with small pressure perturbations in the following way. As before, we represent pressure as the sum of the mean value and the unsteady perturbations:  $p = p_0 + p'$  and expand  $\Pi$  as a series around  $p_0$ , which gives:

$$\begin{aligned} \Pi &= \frac{1}{\gamma} \left[ \ln \left( \frac{p_0}{p_\infty} \right) + \frac{p'}{p_0} - \frac{1}{2} \left( \frac{p'}{p_0} \right)^2 + \frac{1}{3} \left( \frac{p'}{p_0} \right)^3 - \dots \right] \\ &= \underbrace{\frac{1}{\gamma} \ln \left( \frac{p_0}{p_\infty} \right)}_{=\Pi_0} + \frac{1}{\gamma} \left[ \frac{p'}{p_0} - \frac{1}{2} \left( \frac{p'}{p_0} \right)^2 + \frac{1}{3} \left( \frac{p'}{p_0} \right)^3 - \dots \right]. \end{aligned} \quad (2.131)$$

If  $p' \ll p_0$ , such as for small-amplitude acoustic waves, we can neglect the higher order terms. Hence, the perturbation of  $\Pi$  becomes:

$$\Pi' \approx \frac{1}{\gamma} \frac{p'}{p_0}. \quad (2.132)$$

If we further assume constant static pressure  $p_0 = p_\infty$ , such as in a shear flow exhausted from a pipe:

$$\Pi' \approx \frac{1}{\gamma} \frac{p'}{p_\infty} = \frac{p'}{\rho_\infty c_\infty^2} = \frac{p'}{\rho_0 c_0^2}, \quad (2.133)$$

and

$$\Pi_0 = \Pi_\infty = 0, \quad (2.134)$$

and, therefore,  $\Pi \approx \frac{p'}{\rho_\infty c_\infty^2}$ . Phillips' equation (2.130) becomes then:

$$\begin{aligned} & \frac{D_0^2 p'}{Dt^2} - \nabla \cdot (c_0^2 \nabla p') \\ & = \rho_\infty c_\infty^2 \left[ \frac{D}{Dt} \left( \frac{m}{\rho} \right) - \nabla \cdot \left( \frac{\mathbf{f} + \nabla \cdot \boldsymbol{\tau}}{\rho} \right) + \sigma \frac{D^2 s}{Dt^2} + \nabla \cdot (\mathbf{v} \cdot \nabla \mathbf{v}) - \mathbf{v} \cdot \nabla \nabla \cdot \mathbf{v} \right]. \end{aligned} \quad (2.135)$$

The last equation for shear flows could have been obtained also from the starting equations (2.121) and (2.122) in the following way, without introducing Phillips' variable. From

$$\frac{\nabla p}{\rho} = \frac{\mathbf{f} + \nabla \cdot \boldsymbol{\tau}}{\rho} - \frac{D\mathbf{v}}{Dt} \quad \text{and} \quad (2.136)$$

$$\frac{1}{\rho c^2} \frac{Dp}{Dt} = \frac{m}{\rho} + \sigma \frac{Ds}{Dt} - \nabla \cdot \mathbf{v}, \quad (2.137)$$

with the similar procedure as above, that is subtracting the divergence of the first equation from the total derivative of the second one, it follows:

$$\begin{aligned} & \frac{D}{Dt} \left( \frac{1}{\rho c^2} \frac{Dp}{Dt} \right) - \nabla \cdot \left( \frac{1}{\rho} \nabla p \right) = \frac{D}{Dt} \left( \frac{m}{\rho} \right) - \nabla \cdot \left( \frac{\mathbf{f} + \nabla \cdot \boldsymbol{\tau}}{\rho} \right) + \sigma \frac{D^2 s}{Dt^2} \\ & \quad + \nabla \cdot (\mathbf{v} \cdot \nabla \mathbf{v}) - \mathbf{v} \cdot \nabla \nabla \cdot \mathbf{v}. \end{aligned} \quad (2.138)$$

For small perturbations  $p' = p - p_0$  around constant  $p_0 = p_\infty$ , this becomes:

$$\begin{aligned} & \frac{D_0}{Dt} \left( \frac{1}{\rho_0 c_0^2} \frac{D_0 p'}{Dt} \right) - \nabla \cdot \left( \frac{1}{\rho_0} \nabla p' \right) = \frac{D}{Dt} \left( \frac{m}{\rho} \right) - \nabla \cdot \left( \frac{\mathbf{f} + \nabla \cdot \boldsymbol{\tau}}{\rho} \right) + \sigma \frac{D^2 s}{Dt^2} \\ & \quad + \nabla \cdot (\mathbf{v} \cdot \nabla \mathbf{v}) - \mathbf{v} \cdot \nabla \nabla \cdot \mathbf{v} \end{aligned} \quad (2.139)$$

which can be multiplied with constant  $\rho_0 c_0^2 = \rho_\infty c_\infty^2$  to give the same equality as (2.135).

Unlike Lighthill's equation or classical convected wave equation for a uniform flow, the left-hand side operator of the equation (2.135) is capable of capturing sound propagation effects due to spatially varying, non-uniform mean flow velocity (inside

the total derivative of the first term) and sound speed (the second term on the left-hand side). Unfortunately, part of the sound propagation is still contained inside the kinetic terms on the right-hand side of the equation, as proven by Doak [Doa72] for shear flows. This is due to the fact that the velocity vector still contains the acoustic perturbations. In low Mach number flows, these terms become especially important in the regions of abrupt changes of the mean flow velocity, such as at the trailing edge of a pipe exhausting a jet. These terms then describe acoustically-induced vorticity modes which occur at the edge. Somewhat more involved, third-order Lilley's equation [Lil74] addresses this problem. However, it will not be considered here, mostly due to its limitation to parallel shear flows, the computationally more demanding third-order total derivative in its left-hand side differential operator, as well as its inherent instability due to the inclusion of vorticity modes (in the same manner as Linearized Euler Equations, as discussed above).

### 2.6.3 Ffowcs Williams and Hawkings equation

All the equations derived so far describe flows and sound fields in free space. If they are present, the effects of solid bodies in the flow have to be included in the solution of the equations through appropriate boundary conditions at their surfaces. Still, due to the significance of solid bodies for aeroacoustic sound generation in most of the cases in practice, certain aeroacoustic analogies attempt to treat the contribution of the bodies more explicitly. Among such analogies, probably the most common one is introduced by Ffowcs Williams and Hawkings [FH69]. Classical Ffowcs Williams and Hawkings equation can be derived in the following way [DFW83]. Similarly as with the derivation of Lighthill's equation, we start with the mass equation (2.1) and momentum equation (2.2) in a fluid without source terms on the right-hand sides and with neglected viscosity (inviscid flow):

$$\frac{\partial \rho'}{\partial t} + \nabla \cdot (\rho \mathbf{v}) = 0 \quad \text{and} \quad (2.140)$$

$$\frac{\partial (\rho \mathbf{v})}{\partial t} + \nabla \cdot (\rho \mathbf{v} \mathbf{v}) + \nabla p' = 0, \quad (2.141)$$

where  $\rho' = \rho - \rho_0$  and  $p' = p - p_0$ , the unsteady perturbations of density and pressure, respectively, are already introduced and the static pressure  $p_0$  is assumed to be

constant in space. We suppose that the body inside the flow is in general moving with velocity  $\mathbf{v}_B$  (which will be equal to zero if the body is stationary) and that it is surrounded (not necessarily at its own surface) by a control surface moving with it. Since we are only interested in the sound field outside this control surface, we can formally introduce the Heaviside function  $H(f)$ , which equals one outside the control surface and zero inside it, for any function  $f(\mathbf{x}, t)$ , which is negative inside the control surface, positive in the surrounding fluid, and zero at the control surface. Then we multiply the two conservation equations with  $H(f)$  and rearrange the terms to obtain, respectively:

$$\frac{\partial(H\rho')}{\partial t} + \nabla \cdot (H\rho\mathbf{v}) = \rho' \frac{\partial H}{\partial t} + \rho\mathbf{v} \cdot \nabla H \quad \text{and} \quad (2.142)$$

$$\frac{\partial(H\rho\mathbf{v})}{\partial t} + \nabla(Hp') = \rho\mathbf{v} \frac{\partial H}{\partial t} + \rho\mathbf{v}\mathbf{v} \cdot \nabla H + p'\nabla H - \nabla \cdot (H\rho\mathbf{v}\mathbf{v}). \quad (2.143)$$

Taking the time derivative of the mass equation and subtracting the divergence of the momentum equation from it gives:

$$\begin{aligned} \frac{\partial^2(H\rho')}{\partial t^2} - \nabla^2(Hp') &= \frac{\partial}{\partial t} \left( \rho' \frac{\partial H}{\partial t} \right) + \frac{\partial}{\partial t} (\rho\mathbf{v} \cdot \nabla H) - \nabla \cdot \left( \rho\mathbf{v} \frac{\partial H}{\partial t} \right) \\ &\quad - \nabla \cdot (\rho\mathbf{v}\mathbf{v} \cdot \nabla H) - \nabla \cdot (p'\nabla H) + \nabla \cdot \nabla \cdot (H\rho\mathbf{v}\mathbf{v}). \end{aligned} \quad (2.144)$$

A wave equation for density perturbations can be derived by subtracting  $c_0^2 \nabla^2(H\rho')$  from both sides of the equation, with  $c_0$  denoting the steady value of the speed of sound:

$$\begin{aligned} \frac{\partial^2(H\rho')}{\partial t^2} - c_0^2 \nabla^2(H\rho') &= \nabla \cdot \nabla \cdot (H\rho\mathbf{v}\mathbf{v}) + \nabla^2(Hp') - c_0^2 \nabla^2(H\rho') \\ &\quad - \nabla \cdot \left( \rho\mathbf{v} \frac{\partial H}{\partial t} \right) - \nabla \cdot (\rho\mathbf{v}\mathbf{v} \cdot \nabla H) - \nabla \cdot (p'\nabla H) \\ &\quad + \frac{\partial}{\partial t} \left( \rho' \frac{\partial H}{\partial t} \right) + \frac{\partial}{\partial t} (\rho\mathbf{v} \cdot \nabla H). \end{aligned} \quad (2.145)$$

If, in addition, we assume that  $c_0$  is constant in space, such as, for example, in a quiescent (stagnant and uniform) fluid at infinity, when  $c_0 = c_\infty$  is constant, the equation becomes:

$$\begin{aligned}
\frac{\partial^2(H\rho')}{\partial t^2} - c_\infty^2 \nabla^2(H\rho') &= \nabla \cdot \nabla \cdot \{H[\rho\mathbf{v}\mathbf{v} + (p' - c_\infty^2 \rho')\mathbf{I}]\} \\
&- \nabla \cdot \left( \rho\mathbf{v} \frac{\partial H}{\partial t} \right) - \nabla \cdot (\rho\mathbf{v}\mathbf{v} \cdot \nabla H) - \nabla \cdot (p'\nabla H) \\
&+ \frac{\partial}{\partial t} \left( \rho' \frac{\partial H}{\partial t} \right) + \frac{\partial}{\partial t} (\rho\mathbf{v} \cdot \nabla H),
\end{aligned} \tag{2.146}$$

with  $\mathbf{I}$  denoting a unit tensor. The first source term on the right hand side of the equation contains the inviscid Lighthill's tensor:  $\rho\mathbf{v}\mathbf{v} + (p' - c_\infty^2 \rho')\mathbf{I}$ , which characterizes flow-induced noise sources in free space. The two terms in it represent the sound sources due to the unsteady Reynolds stress ( $\rho\mathbf{v}\mathbf{v}$ ) and the deviations from adiabatic changes of state (entropy sources) ( $p' - c_\infty^2 \rho'$ ), which typically appear in unsteady turbulent flows, such as free jets, and sudden heat releases, as in combustions. In such a formulation, both sources behave as free space quadrupoles, when they are located outside the control surface where  $H(f) = 1$ , which exist even in the absence of any solid body inside the flow.

The rest of the source terms are due to the foreign body inside the flow and are non-zero only at the control surface, since  $\frac{\partial H}{\partial t} = -\mathbf{v}_B \cdot \nabla H$  and  $\nabla H(f) = \nabla f \delta(f)$ , with  $\delta(f)$  representing the  $\delta$ -function, which is zero everywhere except at the control surface where  $f = 0$ . After noticing this, the three ‘‘divergence’’ source terms of dipole nature can also be recast into:

$$\begin{aligned}
& -\nabla \cdot [-\rho\mathbf{v}(\mathbf{v}_B \cdot \nabla H) + \rho\mathbf{v}\mathbf{v} \cdot \nabla H + p'\nabla H] \\
&= -\nabla \cdot [-(\rho\mathbf{v}\mathbf{v}_B) \cdot \nabla H + \rho\mathbf{v}\mathbf{v} \cdot \nabla H + p'\mathbf{I} \cdot \nabla H] \\
&= -\nabla \cdot \{[\rho\mathbf{v}(\mathbf{v} - \mathbf{v}_B) + p'\mathbf{I}] \cdot \nabla H\}
\end{aligned} \tag{2.147}$$

and the two monopole sources into:

$$\begin{aligned}
\frac{\partial}{\partial t} \left( \rho' \frac{\partial H}{\partial t} + \rho\mathbf{v} \cdot \nabla H \right) &= \frac{\partial}{\partial t} [-(\rho - \rho_0)\mathbf{v}_B \cdot \nabla H + \rho\mathbf{v} \cdot \nabla H] \\
&= \frac{\partial}{\partial t} \{[\rho(\mathbf{v} - \mathbf{v}_B) + \rho_0\mathbf{v}_B] \cdot \nabla H\}.
\end{aligned} \tag{2.148}$$

The former ones are associated with the so-called loading noise due to the aerodynamic forces acting on the surface of the body, and the latter ones with the so-called thickness noise, that is, volume displacement of the body. It should be mentioned here that it has been discussed in literature [Pow60] that the loading noise

can also be directly attributed to the scattering of sound originating from the free-space sources from the body, that is, due to the “secondary” sources at the surface of the body. In fact, the introduction of the Heaviside function eventually leads to the same result as Kirchhoff’s integral solution in the presence of a solid body, with the flow of fluid.

Equation (2.146) together with equalities (2.147) and (2.148) is the famous Ffowcs Williams and Hawkings wave equation [FH69], which is frequently used to calculate the noise of fan blades, such as the ones of helicopters or in jet engines of aircrafts. It has a didactic significance, as it points to the contributions of monopole and dipole sources, which are due to the presence of the solid body and which radiate more efficiently than free space quadrupoles in low Mach number flows. Major advantage of this formulation is its simple left-hand side, which outside the control surface matches the left-hand side of the classical wave equation, with a simple analytical Green’s function. However, like Lighthill’s analogy which lies in its basis, Ffowcs Williams and Hawkings equation inherits certain drawbacks, namely, difficult calculation of the source terms, especially at high flow velocities [DFW83] and the mistreatment of sound propagation effects as artificial sources of sound. The former problem is commonly approached with the aid of numerical simulations, for example, by the combination of computational fluid dynamics and aeroacoustic solvers. Nevertheless, the implementations of the equation are still most often limited to low Mach number flows, in order to keep the satisfactory accuracy of the solution.

The second problem, however, is in the physical interpretation of the free-space source terms on the right-hand side of the equation (2.146). In order to keep the left-hand side of the resulting wave equation simple as in a quiescent fluid, all other terms had to be shifted to the right-hand side, which left them to be interpreted as sound sources in the same manner as in Lighthill’s analogy. This means that the acoustic perturbations, which constitute a part of the unsteady flow, can (and in all moving or inhomogeneous flows do) appear inside these “source” terms. This is problematic from both physical and computational aspects, since the sought for solution of the acoustic field becomes part of the sources inside the equation which is to be solved. Two pronounced examples of this are acoustic feedback (resonance), when the acoustic perturbation is the source of growing instability and the flow-acoustic

coupling is strong, as well as the sound propagation phenomena – convection and refraction. In fact, all the propagation effects inside moving and inhomogeneous media are entirely contained in the right-hand side of the equation and, thus, appear as artificial sources. These sources are then difficult to model, both because they involve acoustic perturbations and because they are in general spatially distributed through the entire flow region where the propagation phenomena take place.

With regard to that, the main idea of Chapter V will be to combine the procedure for deriving Phillips' free-space aeroacoustic equation with the effects of the foreign body as in Ffowcs Williams and Hawkings formulation. The outcome could be then interpreted as a form of convected Ffowcs Williams and Hawkings equation with Phillips' aeroacoustic analogy in its basis rather than Lighthill's equation. As a consequence, the resulting equation should capture better propagation effects inside inhomogeneous and moving media, separating them from true aeroacoustic sources, while keeping the computational efforts low. It will also inherit some downsides of both approaches of Phillips and Ffowcs Williams and Hawkings, which will also be discussed there.

## **2.7 Analytical solutions of sound radiation from an open pipe**

Sound radiation from an open pipe belongs to the classical problems in acoustics. The first analytical solutions of the problem with a flanged pipe, that is, pipe with the opening embedded in a rigid plane, are attributed to Lord Rayleigh [Ray78], already in the second half of the 19<sup>th</sup> century. However, the first solution for an unflanged circular pipe with a thin wall and a simple straight-cut opening was developed not before the middle of the 20<sup>th</sup> century. This celebrated solution was introduced by Levine and Schwinger [LS48] and included only the acoustic perturbation with a zero mean flow inside the pipe. Therefore, the starting wave equation has the same form as the equation (2.110), although with scalar potential as the unknown quantity rather than sound pressure and in frequency domain. The equation is solved within the low frequency approximation of the plane incident sound wave using the Fourier

transform and the Wiener-Hopf technique. Apart from the far-field directivity, the solution allowed an accurate calculation of reflection coefficient at the pipe opening, including the end-correction.

Increased interest in aircraft noise in the following decades lead to the occurrence of more general solutions, which included the mean flow of gas exhausted from the pipe. The most prominent one is probably derived by Munt [Mun77, Mun90], which included not only hot interior and/or exterior flows with any subsonic value of Mach number, but also higher acoustic modes inside the pipe. The starting equation in this case was a form of the convected wave equation (2.109) in frequency domain and with velocity potential as the unknown. In order to be able to implement the Wiener-Hopf technique, a fairly simple uniform mean flow profile had to be introduced, as shown in Figure 2.1. The regions of the uniform jet with constant sound speed  $c_j$  and the exterior with constant sound speed  $c_\infty$  are separated by an infinitely thin shear (vortex) layer in the extension of the pipe wall. Additional constraint is added to this shear layer by imposing the Kutta condition at the edge of the pipe.

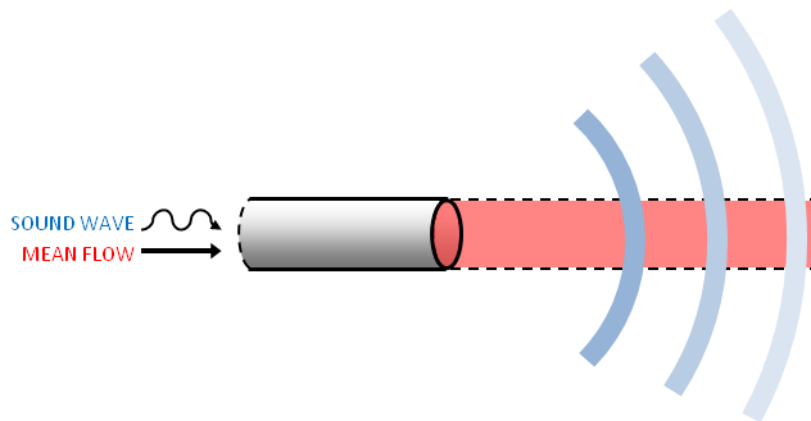


**Figure 2.1:** Geometry and mean flow profile considered by Munt [Mun77].

Similarly as Levine and Schwinger's solution for the no-flow case, Munt's solution allows both exterior sound field (radiation pattern) and the reflection coefficient at the opening of the pipe. Furthermore, the solution has been tested and confirmed several times since its appearance, both experimentally [PB76, TLR+14, MZN+16] and numerically [HGB16, DIA12]. Nevertheless, it has several drawbacks. The complex mathematical apparatus used for its derivation remains to a great extent

incomprehensible and difficult for application by the broader engineering community. Moreover, very few physical interpretations of the results are given with respect to the key acoustic phenomena, which hinders a physical explanation of the obtained result. On the other hand, due to the highly idealized uniform mean flow, the accuracy of the solution is questionable for more realistic jets (for example, in Figure 1.1), especially for capturing refraction effects in the mixing region of the jet. Finally, although the solution is generally referred to as analytical, it requires numerical calculations of several functions and complex integrals, which are needed for its derivation. Certain attempts are made to simplify or approximate Munt's solution and give more physical meaning, at least for some special cases, such as low Mach number values of the flow or low Helmholtz number value [Car82, Rie83]. These solutions will, however, not be treated further in this work and we will refer to Munt's solution as the analytical solution of the problem of sound radiation from a pipe with a mean flow. In the absence of the flow, the solution derived by Levine and Schwinger can be used, or Munt's solution in the limiting case when Mach number of both exterior flow and the jet approaches zero.

## Chapter III

# LABORATORY MEASUREMENTS OF THE FAR-FIELD RADIATION PATTERN

Reports on laboratory measurements of sound radiation from an open pipe with a flow are still rare in literature [ASG+65, Moo77]. Moreover, the measurement scenarios vary and cover a wide range of different flow and acoustic conditions – jet velocities (low subsonic to supersonic) and temperatures (cooled jets, jets at the ambient temperature, or heated jets), as well as the frequencies of the emitted sound. Certain data on the directivity of musical instruments, in particular woodwind and brass instruments can be found in [Mey09]. The goal of this part of the work is to experimentally determine the effect of the jet on the exterior propagation of the incident plane sound wave and the resulting acoustic far-field outside the pipe. On the other hand, all the phenomena which take place inside the pipe, as well as the attenuation of the low frequency sound at the trailing edge, which is due to the shed vortices [How79], are not considered here, as only the shapes of the radiation patterns are measured.

### 3.1 Measurement setup

Measurements are done on a 160cm long steel end-pipe with smooth walls. The thickness of the wall is 2mm, while the inner diameter of the pipe is 40mm. In order to approach the assumption of an infinitely thin trailing edge, the last 5cm of the pipe's downstream end are sharpened to gradually decrease the thickness of the wall to 0.5mm at the very opening. The opening is a straight cut. The acquisition of the sound radiated outside the pipe is performed inside a fully anechoic chamber (see Figure 3.2), with the inner dimensions between the tips of the porous absorbing wedges: 7.2m  $\times$  4.9m  $\times$  5m. The length of the sound absorbing wedges is around 90cm and they are placed over all boundary surfaces of the room – walls, ceiling, and

the floor below the metal grid. The anechoic allows provides fairly accurate free-field conditions at all frequencies above 100 Hz.

The entire equipment used for the measurements can be divided into the mean flow and acoustic part. The mean flow equipment is shown in Figure 3.1. It is entirely placed outside the anechoic chamber and consists of two main components:

- Elektroror SD 900 blower with the maximum volume flow  $14.5\text{m}^3/\text{min}$  and the maximum power 11kW and
- 6 heaters placed within a 4m long expanded pipe section, with the total power of 110kW.

The blower is connected to the heaters with 80mm-diameter pipes with the total length of around 2m. Following the section with the heaters and before entering the anechoic chamber, the pipe is gradually contracted to the final diameter of 40mm.

The mean flow speed is measured after a stable steady state is established and prior to each acoustic measurement, by means of a pitot tube placed at the centre of the end-pipe opening. Hence, the maximum Mach number value ( $M_{max}$ ) of the fully developed mean flow inside the pipe is measured. With regard to that, all Mach number values of the jet given in this chapter refer to the maximum value at the pipe axis ( $M = M_{max}$ ), if not specified otherwise. The jet temperature is measured continuously inside the pipe with a thermocouple type K with the thickness 1mm. The thermocouple is placed 60cm from the pipe opening and fixed around the centre of the pipe's cross section. Therefore, the measured temperature values should closely represent the average temperature of the flow inside the pipe. All the Mach number values refer to the local sound speed inside the jet, which is calculated using the equations (2.39) for a perfect gas, that is:

$$c = \sqrt{\gamma RT} , \quad (3.1)$$

where  $\gamma = 1.4$  is the specific heat ratio for air,  $R = 287.058 \text{ J}/(\text{kgK})$  is the specific gas constant, and  $T$  is the absolute temperature in Kelvin degrees.

The Mach number value of the mean flow inside the end-pipe is increased in the steps of 0.05, starting from the no-flow case with  $M = 0$  up to the maximum value  $M = 0.25$ . Maximum temperature of the jet is  $300^\circ\text{C}$  and it is reached in  $100^\circ\text{C}$  steps,

namely: cold jet (close to the ambient temperature inside the anechoic chamber), 100°C, 200°C and 300°C. In order to prevent the heaters from overheating, the minimum Mach number of the flow 0.08 has to be introduced in all the cases of the heated jet, with the temperature 100°C or above. The ambient temperature inside the anechoic chamber is continuously controlled and kept between 24°C and 29°C. Due to the self heating of the jet, though, the temperature of the cold jet is somewhat higher and varies between 38°C and 41°C.

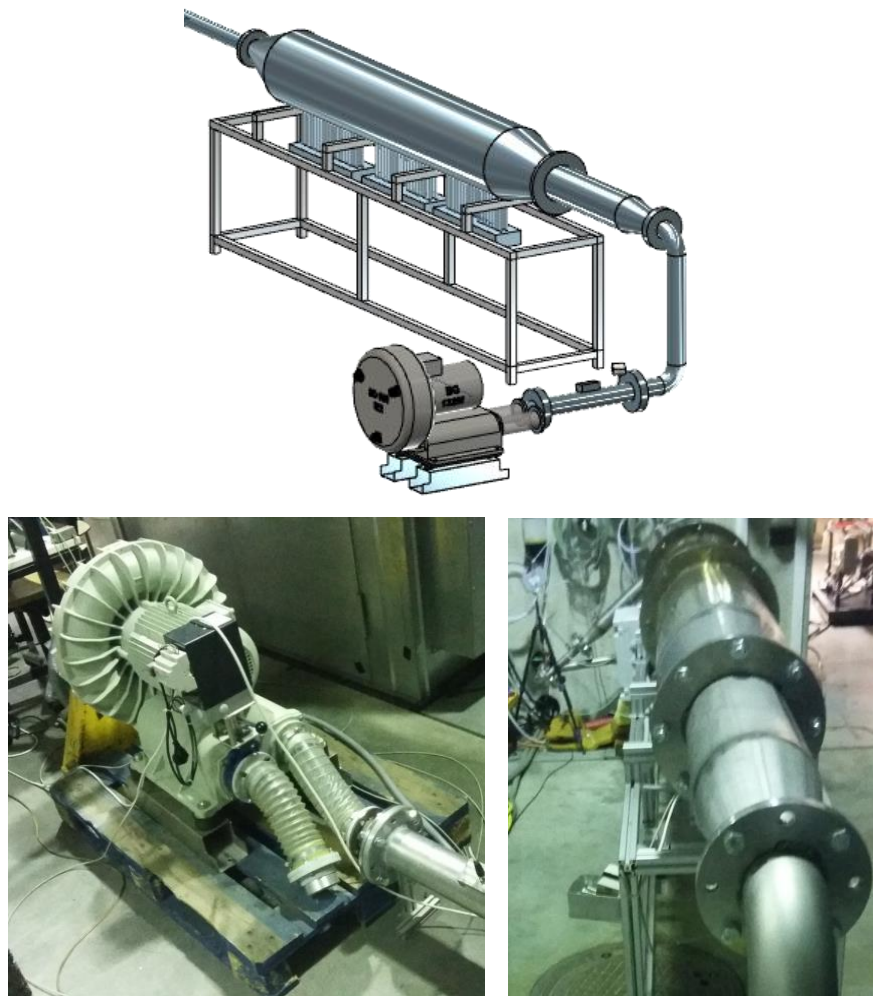


**Figure 3.1:** The mean flow equipment: (above) sketch of the setup, (below left) the blower, (below right) the pipe section with the heaters.

The equipment which is used for the acoustic measurements of the radiated sound field includes the following:

- DAP audio AB-12 loudspeaker with the impedance  $8\Omega$ , diameter of the driver 30cm, nominal frequency range 55-2500Hz, and the RMS power 300W; the

loudspeaker is placed inside a specially designed sealed metal box (Figure 3.2 above); the side of the box which is facing the driver contracts gradually and ends into a 0.5m long 40mm-diameter side-branch pipe; together with the mean flow equipment, the box with the loudspeaker is placed outside the anechoic chamber; the termination of the branch pipe makes a junction with the pipe containing the mean flow around 1.5m after the heaters and 4.5m before the entrance of the end-pipe inside the anechoic chamber,

- 18 NTi Audio M2230 ½-inch omnidirectional free-field microphones with the equivalent noise level 16dB(A), accuracy within  $\pm 1$ dB at frequencies 20-4000Hz, and the temperature coefficient less than  $-0.01$ dB/°C within the temperature range  $-10^{\circ}\text{C}$  to  $50^{\circ}\text{C}$ ; the microphones are clamped to the upper half of a 5cm-diameter metal tube construction in the form of a circle positioned in a vertical plane which contains the end-pipe (Figure 3.2 below); the circle has the radius 1.5m with the opening of the end-pipe in its centre; the angles to the pipe axis of the 18 microphones in the semi-circular array are:  $0^{\circ}$ ,  $5.625^{\circ}$ ,  $11.25^{\circ}$ ,  $16.875^{\circ}$ ,  $22.5^{\circ}$ ,  $33.75^{\circ}$ ,  $45^{\circ}$ ,  $56.25^{\circ}$ ,  $67.5^{\circ}$ ,  $78.75^{\circ}$ ,  $90^{\circ}$ ,  $101.25^{\circ}$ ,  $112.5^{\circ}$ ,  $123.75^{\circ}$ ,  $135^{\circ}$ ,  $146.25^{\circ}$ ,  $157.5^{\circ}$ , and  $168.75^{\circ}$ , where the zero-angle corresponds to the end-pipe axis in front of the opening, in the positive (downstream) direction; therefore, axial symmetry of the sound field is assumed; all the microphones are calibrated prior to the measurements, using a standard sine-wave calibrator at the frequency 1kHz,
- 2 additional reference microphones of the same type as the microphones in the microphone array are placed close to the pipe opening, one of which is ultimately used for the extraction of the radiation patterns; this microphone is positioned in the horizontal plane of the pipe, 2cm behind the plane of the pipe opening and at the distance 22cm from the pipe, in the region where the effects of the mean flow are negligible; the signals recorded using this reference microphone are used in the post-processing for additional normalization with the direct sound coming from the pipe;
- DirectOut Andiamo.MC microphone preamplifier with an integrated A/D converter,
- RME MADiface USB audio interface, and
- PC supplied with the routines for multichannel signal acquisition; the routines are created using Pure Data [Pur17].



**Figure 3.2:** The acoustic measurements setup: (above) the loudspeaker box placed at the end of a side-branch pipe, (below) the semi-circular microphone array placed around the opening of the end-pipe and the two reference microphones inside the anechoic chamber.

The excitation signal which is emitted from the loudspeaker is swept-sine with the duration 3s. Signals are simultaneously recorded with all the microphones, with the duration of each recording 4s. The sampling frequency of the multichannel recording is 44100 Hz and the resolution is 32 bit/sample. 10 successive measurements are carried out for each measurement scenario, that is, for a particular mean flow speed and temperature values. The signals recorded during the 10 repetitions are then averaged, in order to improve the overall signal-to-noise ratio of the measurements, by averaging out the random noise components, for example flow-induced noise. The following subsection describes the signal processing procedures in more details.

## 3.2 Signal processing

In order to obtain accurate frequency dependent radiation patterns, different signal processing steps are applied on the swept-sine signals recorded with the 18 microphones in the semi-circular array, as well as the reference microphone. The steps are done in the following order:

- time domain averaging of 10 repeated measurements with the same mean flow properties (Mach number and temperature);
- spectral division with the input swept-sine signal emitted from the loudspeaker, which results in the impulse responses at the microphone locations;
- time windowing of the impulse responses in order to suppress the late reflections generated inside the system of pipes and the flow equipment, as well as the possible spurious reflections due to the non-linearity of the loudspeaker;
- spectral division of the 18 impulse responses from the microphone array with the impulse response acquired with the reference microphone, in order to normalize the former responses with the actual sound radiated from the pipe opening;
- band-pass filtering using a combination of the 4<sup>th</sup>-order low-pass Butterworth filter with the cutoff frequency 5kHz and the 4<sup>th</sup>-order high-pass Butterworth filter with the cutoff frequency 100Hz, in order to remove the low- and high-frequency noise components outside the frequency range of interest;
- time windowing of the direct sound from the filtered impulse responses, which removes the remaining reflections inside the anechoic chamber and from the pieces of equipment; the rectangular time window with the duration 4ms is supplied with the raised cosine fade in and fade out parts, each 10 samples long, and
- spectral analysis of the extracted direct sounds obtained at the array microphones located at different angles to the pipe axis, with the frequency resolution 0.67Hz; this results in the frequency dependent radiation patterns.

Figure 3.3 shows the block diagram of the entire signal processing procedure. The radiation patterns obtained in the presence of the mean flow are additionally corrected

for the bias error, which is estimated from the no-flow measurements, as described in the following subsection with the measurement results.

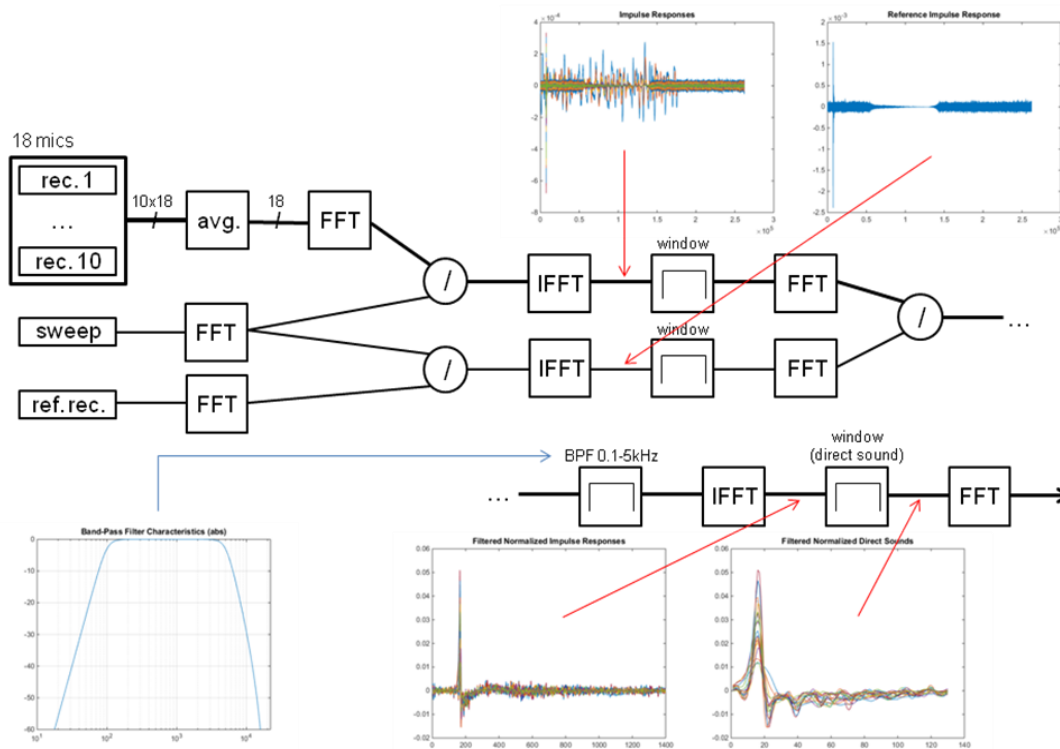


**Figure 3.3:** Post-processing of the recorded signals.

Implementation of the swept-sine technique and the appropriate signal processing procedures allows efficient suppression of flow-generated and background noise (time averaging and spectral division), non-linearity of the source (time windowing of the impulse responses), as well as the additional reflections inside the chamber (extraction of the direct sound). It is worth mentioning that the preliminary measurements are done using pure sine waves as the excitation signals and they show much lower accuracy of the results together with more limited possibilities for the post-processing of the recorded signals and further improvement of the overall signal-to-noise ratio. In addition to this, the swept-sine measurements allow accurate estimation of the radiation patterns at any particular frequency within the frequency range of the swept-sine (with the resolution of the spectral analysis), even without further averaging over several frequencies or frequency ranges, as done in [ASG+65].

### 3.3 Results

This subsection presents the results of the laboratory measurements of the radiation patterns and compares them with the analytical solution derived by Munt [Mun77, Bie02]. Since the focus is on the effect of the mean flow on the sound propagation outside the pipe, only the shapes of the radiation patterns are studied, while the total radiated power is neglected. The results are, therefore, given as normalized radiation patterns, which show the angular distribution of the far-field sound pressure level. In the results shown in this chapter, all measured and calculated (analytical) radiation patterns are normalized so that the total sound energy estimated from the total range of the angles to the pipe axis equals 0dB. In other words, the obtained radiation patterns represent the power-gain functions of the angle, relative to the omnidirectional radiation. Another normalization, which is often utilized in literature and will be used later throughout the work is based on the sound pressure level at the angle to the pipe axis  $\theta = 90^\circ$ . However, the normalization according to the total energy removes the contribution of the source. This seems to be more appropriate for comparison of the radiation patterns at different frequencies or with different mean flow conditions, when the acoustic power radiated by the source, the radiation impedance at the pipe opening, and the attenuation of the sound inside the vortices which are shed from the pipe edge [How79] can vary, depending on the frequency of the incident sound or the mean flow properties.

Since Mach number values of the flow are measured at the centre of the pipe opening and, therefore, represent the maximum values inside the flow ( $M_{max}$ ), the estimated average value over the pipe's cross-section area is approximated as  $M_{avg} \approx 0.8M_{max}$  [Rus11]. This relation is derived based on the estimated Reynolds numbers, which for all non-zero Mach numbers covered by the measurements vary between  $2.5 \cdot 10^4$  and  $1.6 \cdot 10^5$ , with the pipe inner radius as the reference length. This scaling proves to be necessary in order to compare the results with Munt's analytical solution, which assumes a uniform top-hat mean flow profile, in which  $M_{avg} = M_{max}$ . It should be noted that a lot of discussion in the literature has been dedicated to the issue which Mach number value should be considered when the flow inside the pipe is fully developed ( $M_{avg} < M_{max}$ ) and Munt's solution is to be used for the analytical

estimation [TLR+14, PHR+93]. In this analysis, the estimated average value  $M_{avg}$  is used for the calculations using Munt's solution, as it lead to the best match between the analytical and measured radiation pattern shapes. Nevertheless, it should be underlined once again that in the rest of this chapter and on the diagrams with the measurement results,  $M$  denotes the maximum Mach number value, as it is measured at the pipe axis, while the additional scaling factor of 0.8 is assumed for the results based on the Munt's model.

### 3.3.1 No-flow case

The first set of measurements is done in the absence of the mean flow. The flow equipment is switched off and the only unsteady field inside and outside the pipe is expected to originate from the loudspeaker located in the side-branch pipe. Hence, the far-field radiation patterns depend only on the frequency of the emitted sound, or, more precisely, the dimensionless Helmholtz number  $ka$ , where  $k$  is the wave number of the sound and  $a$  is the inner pipe radius. The no-flow case can also be considered as the reference case, with the analytical solution of the problem well established both by Levine and Schwinger [LS48] or Munt [Mun77] in the limiting case when  $M \rightarrow 0$ . Therefore, it is also used here for the validation of the measurement procedure and the assessment of the measurement error. The obtained radiation patterns are shown in Figure 3.4 for three values of low Helmholtz number, which will also be used in the following for expressing the results in the presence of the mean flow. These are  $ka = 0.1$ ,  $0.5$ , and  $0.9$ , which, with the estimated speed of sound  $c = 343\text{m/s}$  and the inner pipe radius  $a = 0.02\text{m}$ , correspond to the frequencies  $f = 281\text{Hz}$ ,  $1407\text{Hz}$ , and  $2533\text{Hz}$ , respectively.

The measured radiation patterns for the lower two values of Helmholtz number,  $ka = 0.1$  and  $ka = 0.5$ , are fairly omnidirectional, with the deviations from the theoretical values less than  $\pm 0.6\text{dB}$ . Somewhat larger deviations from the analytical curve are noticeable for the highest Helmholtz number  $ka = 0.9$ , although the measured radiation pattern exhibits the same overall shape as the analytical one. This means a slightly pronounced directivity in the positive direction along the pipe axis (around  $\theta = 0^\circ$ ), and a drop of radiation at higher angles to the axis. The deviations

between the two sets of curves can, thus, be attributed to the measurement error. The measurement accuracy estimated from these results is given in Table 3.1 for all three values of Helmholtz number, in terms of the maximum positive ( $L_{max}$ ) and negative ( $L_{min}$ ) excursions of the measured values at all 18 microphones compared to the analytical ones, as well as the standard deviations of the differences ( $\sigma$ ).

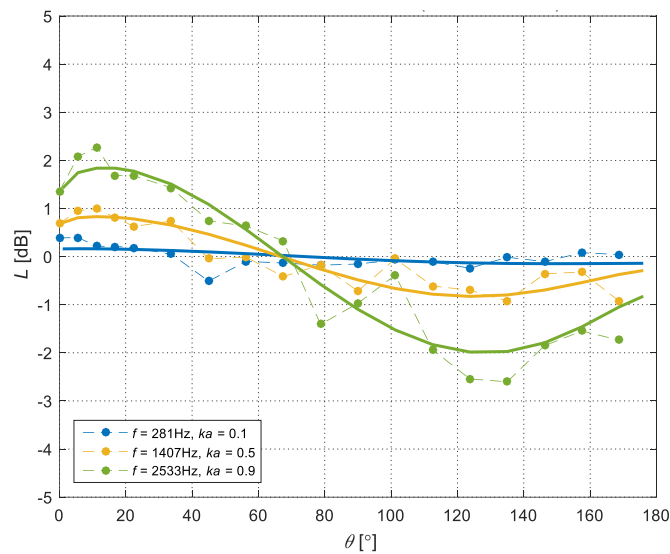


**Figure 3.4:** Radiation patterns in the no-flow case for different values of Helmholtz number; dots – measured, lines – calculated according to [Mun77].

**Table 3.1:** Estimated measurement accuracy for different values of Helmholtz number, based on the measurements without the mean flow.

$f$ [Hz]	$ka$	$\sigma$	$L_{min}$ [dB]	$L_{max}$ [dB]
281	0.1	0.20	-0.60	0.24
1407	0.5	0.30	-0.54	0.63
2533	0.9	0.47	-0.79	1.18

The inaccuracies of the radiation patterns measured in the no-flow case with very low level of ambient noise are expected to occur mainly due to the lack of free-space conditions inside the anechoic chamber, at the locations of the measurement microphones. Critical are the very early reflections, which reach the microphones within the introduced 4ms-long time window of the direct sound. They possibly originate from the pieces of the equipment located close to the pipe opening or the microphones in the array, such as the metal construction which holds the

microphones. As such, these reflections are the source of a systematic error, which appears also in all the subsequent measurements with the mean flow.

In order to further cancel the error, the radiation pattern curves shown in the rest of the chapter include an additional correction, which is applied by subtracting the differences between the measured and the analytical curves in the reference no-flow case (for the corresponding Helmholtz number) from the results obtained in the presence of the mean flow, for each angle to the axis. This correction is justified assuming that the analytical curves are accurate in the absence of the mean flow and that the deviations of the measured values are systematic and, thus, do not change in the presence of the flow. The first assumption seems to be reasonable after noticing that the overall shapes of the theoretical and measured curves in Figure 3.4 are similar for all Helmholtz numbers considered. The second assumption, however, holds only if the laboratory conditions which lead to the inaccuracies in the no-flow case do not change significantly when the mean flow is introduced, so that the correction remains appropriate in latter cases, as well. In fact, change of the directivity of the pipe opening as a sound source due to the mean flow, will naturally affect the amount of the reflected sound energy which reaches different microphones in the array. However, this is considered to be of the secondary importance for the overall accuracy and, indeed, the introduced correction leads to the smooth radiation pattern curves in most of the cases and a much better match with the analytical curves, as will be demonstrated in the following.

The following results point to the effects of the mean flow velocity (expressed with the Mach number value at the pipe axis,  $M$ ) and temperature ( $T$ ), as well as the Helmholtz number ( $ka$ ) on the shape of the far-field radiation patterns. The effects of the mean flow velocity are inspected for the cold jet ( $T \approx 40^\circ\text{C}$ ), while the temperature effects are analyzed for low but finite Mach number value ( $M \approx 0.1$ ). Both contributions are analyzed for the three values of Helmholtz number which are listed in Table 3.1. Lastly, the effect of the varying Helmholtz number value are analyzed for the hot flow ( $T = 300^\circ\text{C}$ ) and the two Mach number values,  $M = 0.1$  and  $M = 0.25$ .

### 3.3.2 Mean flow velocity effects

The influence of the mean flow velocity of a cold jet on the overall shape of the far-field radiation pattern is visible in Figure 3.5. The graphs are given for the three different values of Helmholtz number. The Mach number value varies between 0 and 0.25 in equal steps of 0.05 and the flow temperature inside the end-pipe is negligibly higher than the ambient value, around 40°C. The analytical solutions and the measured values show a very good match at all angles to the pipe axis<sup>7</sup>. From Figure 3.5 (above) it follows that the influence of the mean flow on the directivity can be significant even at very low frequencies ( $ka = 0.1$ ). Thus, although the radius of the pipe opening is much smaller than the wavelength of the sound, it cannot be considered as a simple, omnidirectional monopole source. The directivity increases with the mean flow velocity, in a way that the sound pressure levels in the front half-space (downstream) increase, while the levels in the rear half-space drop as the Mach number value increases. This resembles the effect of convective amplification, which is well-known and mathematically described inside uniform flows [Del14]. In both cases, the angularly dependent factor, sound pressure gain in the far field, is for low Mach number values approximately equal to  $1 + M \cos(\theta)$ . However, the similarity of the two phenomena is only apparent. It will be discussed in the next chapter that the actual cause of the far-field directivity in the case of an open unflanged pipe with a mean wall has little to do with the convection by the flow. It is mainly due to the effect of the vortices which are induced by the incoming plane acoustic wave and shed at the sharp trailing edge of the pipe.

---

<sup>7</sup> It should be mentioned that only in the diagram for  $ka = 0.1$  and only in the curve for  $M = 0.25$ , the measured value at  $\theta = 0^\circ$  is omitted from the figure due to the obvious measurement error of several decibels. This is most probably due to the strong action of the jet on the on-axis microphone. All other measured values are kept on the graphs shown below.

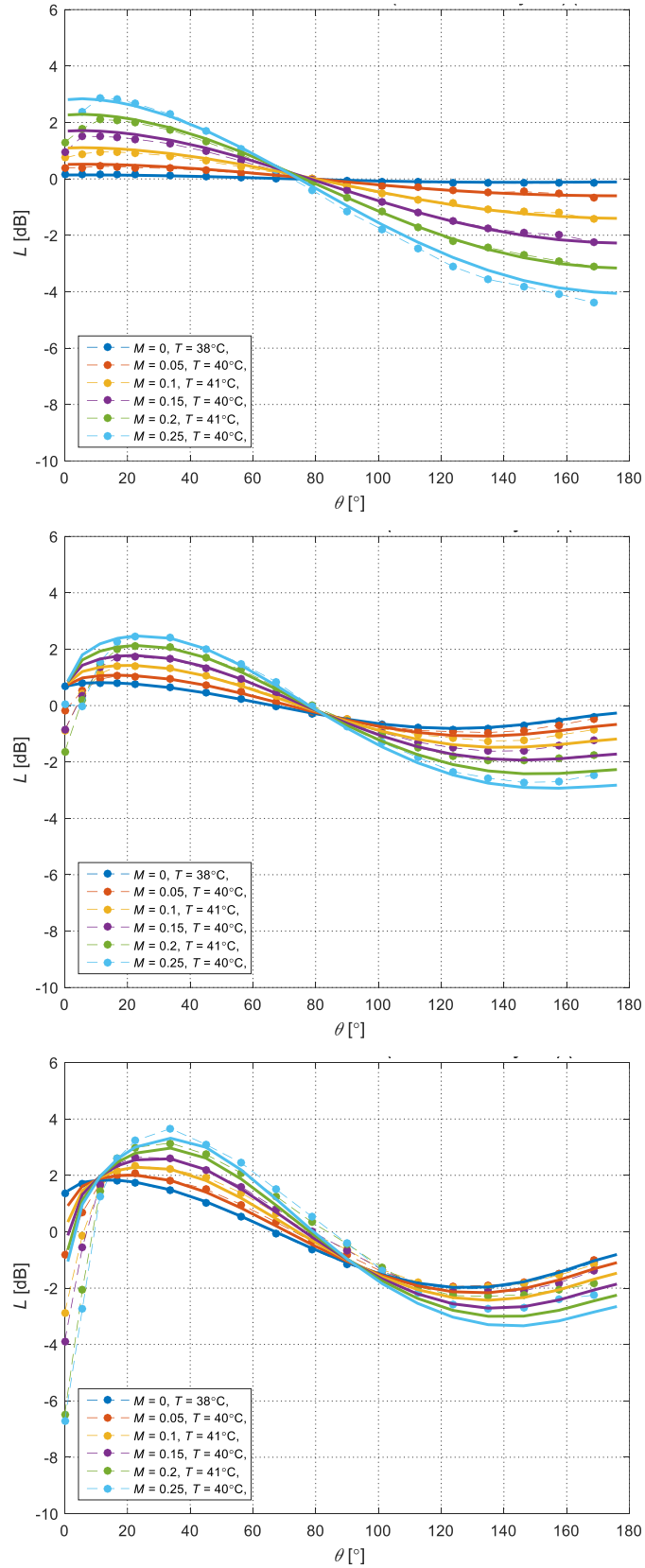


**Figure 3.5:** Radiation patterns in the cold-jet case ( $T \approx 40^\circ\text{C}$ ) for different values of Mach number and (above)  $ka = 0.1$ , (middle)  $ka = 0.5$ , and (below)  $ka = 0.9$ ; dots – measured, lines – calculated values according to [Mun77].

Contribution of the refraction at the very low frequencies is negligible. However, already at  $ka = 0.5$  (the middle diagram in Figure 3.5), refraction due to the spatially decaying mean flow speed becomes noticeable at low angles to the pipe axis, where it adds to the overall radiation pattern shape determined by the jet velocity value. This leads to the formation of the so-called “zone of relative silence” or “cone of silence” at the pipe axis downstream. This effect visible even in the cold mean flow is only partly captured by Munt’s analytical solution, as the measured curves show more pronounced drop towards the pipe axis. Furthermore, the differences between the measured and the analytical curves at low angles to the axis increase with the Helmholtz number value, up to almost 6dB for  $ka = 0.9$ . Since the applied normalization is based on the total radiated energy in all directions, the energy in this narrow region can affect the general position of the radiation pattern curve along the vertical axis on the diagrams. The overestimation of sound energy in this region of attenuated sound makes the analytical curves stand slightly lower compared to the measured curves after the normalization. This explains the apparent displacements between the two sets of curves at higher frequencies ( $ka = 0.9$ ) outside the zone of relative silence.

### 3.3.3 Temperature effects

Main contribution of the hot jet to the far-field directivity is illustrated in Figure 3.6, for a relatively low Mach number value of around 0.1. As already mentioned, this minimum value of the mean flow velocity is dictated by the practical reasons, that is, to protect the heaters from overheating. The temperature range considered is between 41°C and 300°C. Unlike mean flow velocity, temperature has practically negligible effect on the directivity at the lowest frequencies and it is less than  $\pm 0.5$  dB at all angles to the axis. This is due to the fact that the sound wavelength is much larger than the characteristic length scale over which both the temperature and the mean flow velocity decay. The mixing region of the jet, in which the values of its physical parameters spatially decay to meet the ambient values far from the pipe opening, is too small even along the pipe axis for refraction to make any significant effect. On the other hand, the small increase of the directivity with temperature, which is noticeable

in Figure 3.6 (above), is actually due to the increase of the mean flow velocity, which is for the same Mach number value higher in the case of a hot jet, as the reference local sound speed inside the jet is larger compared to the cold jet. In any case, since the refraction is negligible, the theoretical and measured curves again show a good match.

The refraction effects for Helmholtz number value  $ka = 0.5$  are even more pronounced than in the case of the cold jet (middle diagram in Figure 3.5). The non-uniform temperature profile in the mixing region of the hot jet outside the pipe is added to the non-uniform mean flow speed profile to further support the refraction. The measured curves for high temperature values in Figure 3.6 (middle) show up to around 7dB lower minimum values at the pipe axis, compared to the analytical curves. The differences are largest at the pipe axis downstream, where the mixing region is the thickest and comparable or even larger than the sound wavelength. The differences increase further in the lowest diagram (note the changed scale of the vertical axis), for  $ka = 0.9$ , particularly at  $\theta = 0^\circ$ , where the measurement results show a drop more than 20dB lower than the one obtained by the analytical solution. In this extreme case of a hot jet and high frequency of the sound, sound pressure levels inside the zone of relative silence can be more than 30dB lower than at the maximum of radiation at the angle around  $55^\circ$ . In conclusion, refraction should be taken into account only in the cases of highly inhomogeneous flows involving at least moderately high Helmholtz number values of the sound. Even then, its influence in round jets is limited to very low angles to the pipe axis.

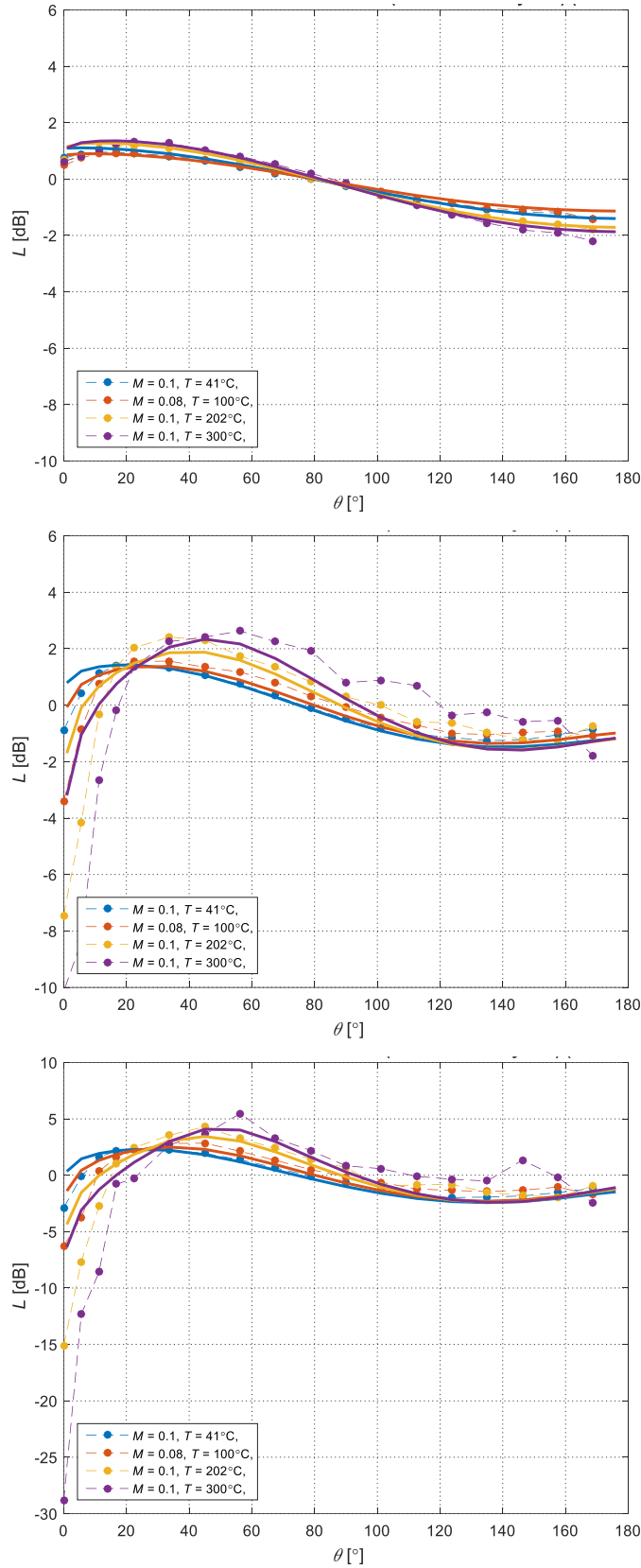


**Figure 3.6:** Radiation patterns for different values of temperature,  $M \approx 0.1$ , and (above)  $ka = 0.1$ , (middle)  $ka = 0.5$ , and (below)  $ka = 0.9$ ; dots – measured, lines – calculated values according to [Mun77].

### 3.3.4 Frequency effects

From the results given above, it follows that the ratio between the pipe radius (or diameter) and the sound wavelength, which is usually expressed with Helmholtz number, is critical for the assessment of far-field sound radiation at low angles to the pipe axis. On the other hand, the thickness of the mixing region along the pipe axis is directly proportional to the radius of the round jet [Wit74]. When the former one becomes comparable to the sound wavelength, as the sound frequency increases, the mean flow speed and temperature gradients inside the flow have a much larger effect on the sound propagation than in the case of much larger wavelengths of the sound. This is clearly demonstrated in Figure 3.7 for a hot jet ( $T = 300^{\circ}\text{C}$ ) and for two different Mach number values,  $M = 0.1$  and  $M = 0.25$ . The increasing value of the Helmholtz number  $ka$  takes values from 0.1 to 0.9 in the steps of 0.2.

The measured curves have much faster decay at the angles below  $20^{\circ}$  compared to the analytical ones in both diagrams, when the frequency is increasing. This discrepancy is largely due to the adopted uniform mean flow profile (Figure 2.1) as used by the analytical solution, which assumes constant temperature and mean flow velocity profiles within the extension of the pipe opening to infinity, together with an infinitely thin shear layer. Consequently, such a model cannot capture accurately the influence of the spatial decay of temperature and mean flow velocity, as well as the finiteness of the characteristic length scale of the mixing region. These effects become important at higher frequencies of the radiated sound, when the wavelength is comparable to the characteristic length scale of the mean flow, and for higher values of Mach number and temperature. Since this is most easily satisfied along the pipe axis downstream, due to the narrowness of the jet, the inaccuracy of the analytical solution is high at low angles to the axis. It is interesting to note that similar discrepancies at angles to the axis below  $30^{\circ}$  are also reported in [SSS13], where the analytical solution is compared with the numerical results obtained using the two-dimensional lattice Boltzmann method.

In general, the radiation minimum at the zero-angle is becoming lower as any one of the values  $ka$ ,  $M$ , or  $T$  increases. The only significant exception to this rule is found in the lower graph in Figure 3.7, where the zero-angle value for the highest value of

Helmholtz number  $ka = 0.9$  is larger than for  $ka = 0.7$ . However, this is probably due to the low signal-to-noise ratio at the corresponding on-axis microphone, owing to the low level of the emitted signal and high noise induced by the flow at the microphone. Moreover, for  $T = 300^\circ\text{C}$ , the sound frequency which corresponds to the value  $ka = 0.9$  is around 3.5kHz, which is actually beyond the nominal frequency range of the used loudspeaker.

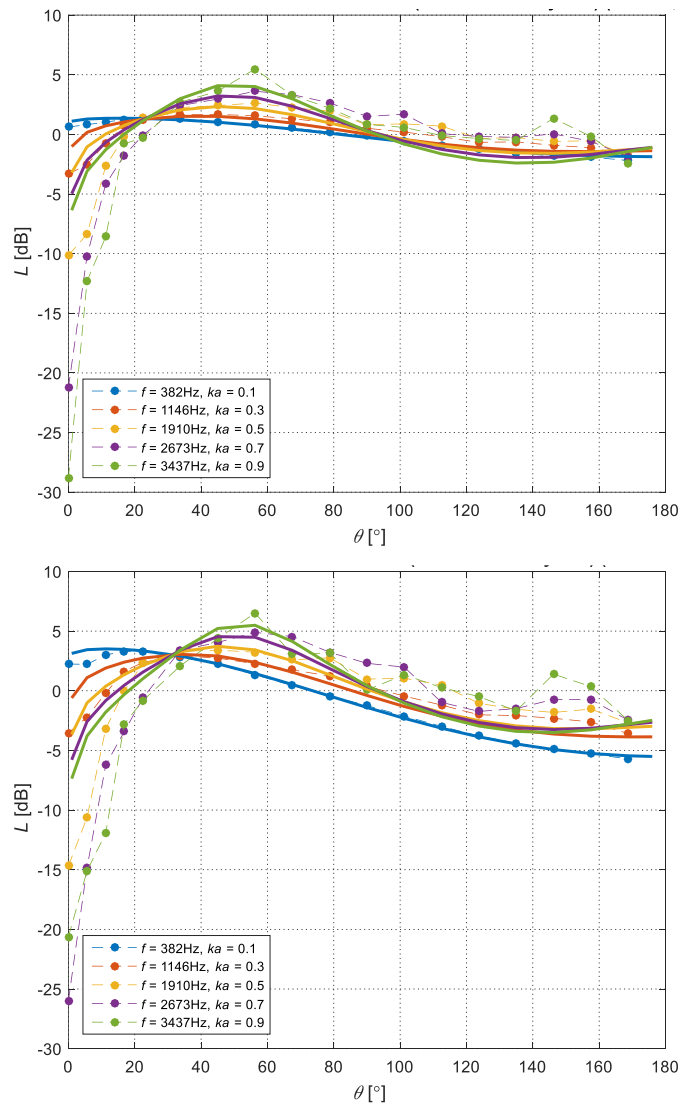


**Figure 3.7:** Radiation patterns in the hot-jet case ( $T = 300^\circ\text{C}$ ) for different values of Helmholtz number and (above)  $M = 0.1$  and (below)  $M = 0.25$ ; dots – measured, lines – calculated values according to [Mun77].

### 3.4 Discussion

Taking into account that the diameter of the end-pipe which was used for the measurements fits well with a typical size of a tail-pipe of an exhaust system of vehicles and that the considered ranges of the mean flow velocities and temperatures cover most of the common flow conditions in ducts of exhaust systems [Wal01], the obtained results can be most straightforwardly used for the estimation of (free-space) pass-by noise. With regard to this, the upper diagram in Figure 3.7 corresponds to a realistic case of the mean flow velocity of 48m/s (Mach number value equal to 0.1 relative to the sound speed around 480m/s) and the temperature of 300°C.

Even at the lowest frequencies, below 400 Hz ( $ka \approx 0.1$ ), the radiation pattern shows a sound pressure level gain up to 1.5dB downstream from the pipe opening and a drop of around 2dB in the opposite direction, compared to a practically omnidirectional directivity in the no-flow case (Figure 3.4). As discussed above, this effect on the directivity can be approximated well for low Mach number values with the amplification factor  $1 + M_{ac} \cos(\theta)$  of the far-field sound pressure, where  $M_{ac}$  is the so-called acoustic Mach number, which takes the sound speed in the ambient air at infinity as the reference, rather than the local sound speed in the jet, which varies with the temperature of the jet. Such low frequencies cover the lowest tones or engine orders. Towards the higher frequencies in the middle of the audible frequency range, the sound wavelength becomes comparable to the characteristic length scale of the mixing region in front of the pipe opening and the refraction effects becomes more evident. Already around 1kHz, sound pressure level is expected to drop around 3dB at the axis, relative to the omnidirectional case, and around 4dB relative to the no-flow case. The zone of relative silence around the axis expands up to around 20° to the axis and the radiation maximum is shifted from the axis to the angle around 35°. The refraction effects become more pronounced as the frequency increases and the wavelengths become comparable to the pipe diameter (but still long enough for the assumption of a plane wave inside the pipe to hold). The zone of relative silence expands further up to between 20° and 30° to the axis and can produce a drop of more than 20dB at the axis. At the same time, the sound energy which is deflected from the

axis builds the maximum around  $50^\circ$  to the axis, which is around 5dB higher compared to the omnidirectional radiation.

The experimental results presented here lead to two important conclusions regarding the far-field radiation pattern of the low-frequency sound emitted from an open cylindrical pipe with a hot low Mach number flow:

- the directivity at the lowest frequencies, for which  $ka \ll 1$ , or at higher angles to the axis are principally determined by the jet velocity, while the mean flow speed and temperature gradients in the mixing region (which lead to refraction) have no significant effect; this is very well captured by the analytical model of Munt [Mun77]; however, the angular dependence of the far-field sound pressure can also be estimated very simply and reasonably accurate with the factor  $1 + M_{ac} \cos(\theta)$ , where  $M_{ac}$  is the acoustic Mach number at the pipe axis; this is, for example, the most relevant case for the sound radiation from a tail-pipe of a vehicle exhaust system at the lowest engine orders or the low musical tones produced in wind instruments;
- for higher values of Helmholtz number, Mach number, and temperature, the refraction effects lead to the occurrence of the zone of relative silence downstream and at small angles to the pipe axis; this leads to the sudden drop of sound pressure level at the axis and the shift of the radiation maximum from the axis to around  $45^\circ$ ; this effect of the refraction is not well captured by the analytical solution, mainly due to the highly idealized top-hat profile of the mean flow; this case becomes relevant for high frequency tones.

The experimental data contained in this chapter will be used in the following primarily for the validation and comparison of different models of sound radiation from an open pipe with a hot mean flow with a low Mach number value. The systematic measurements of the radiation patterns allowed identification of the major contributions to the acoustic far-field and their relation with the independent parameters – mean flow velocity, temperature, and sound frequency. Apart from the improvement of the measurement accuracy at higher frequencies, possible future measurements could also include the sound field inside the pipe, in addition to the far-field measurements. This would allow the assessment of both total radiated sound

power and the power dissipated at the pipe edge, as well as the measurements of the incident sound intensity, reflection coefficient, and radiation impedance at the pipe opening. Expanding the frequency range could in addition allow characterisation of broadband aeroacoustic sources or higher acoustic modes inside the pipe. Lastly, different geometries of the pipe opening (nozzle) would bring the measurements closer to the particular engineering applications.



## **Chapter IV**

# **SIMPLE MODEL OF THE FAR-FIELD RADIATION**

In Chapter II, several analytical solutions for the problem of sound radiation from an open pipe with a mean flow were discussed. Among them, Munt's solution [Mun77] is probably the most referenced one in literature, due to its comprehensiveness and accuracy in wide range of scenarios. Nevertheless, certain drawbacks of the solution were also pointed out, such as the mathematical complexity of the derivation on one side, and the high degree of idealization of the jet properties on the other side. Therefore, this chapter will present an attempt to come up with a simple, analytical or semi-analytical model of the far-field sound radiation from an open pipe with a hot flow. The model should be able to capture the main sound propagation and vortex-sound interaction phenomena which determine the far-field radiation pattern outside the pipe in an approximate but physically transparent way, while keeping the accuracy comparable to Munt's solution. It should also be based on a simple empirical model of the jet, which would allow more accurate estimation of the refraction in the decaying region of the flow. In order to do so, the model will be valid only for low Mach number flows and at low frequencies (Helmholtz numbers) of the incident sound. These limitations make it more restrictive compared to Munt's solution (all subsonic Mach number values and broad frequency range). Nevertheless, many practical problems which are addressed in this work satisfy the given limitations, such as the ones associated with intake, exhaust, and ventilation systems in vehicles, pass-by noise, or low frequency tones of wind instruments.

In the following, the covered acoustic phenomena will be treated according to the order in which they appear on the path between the true source inside the pipe and the listener outside the pipe, located in the far acoustic field. These are, namely:

- incident sound inside the pipe,
- vortex-sound interaction at the pipe edge, and
- refraction in the mixing region of the jet.

In the end of the chapter, all three contributions will be combined and the estimated shapes of the radiation patterns will be compared to those obtained with Munt's solution and the experimental data from the previous chapter.

## 4.1 Incident sound

The incident sound inside the pipe is assumed to originate from any sound source which is located deep inside the pipe, far from the opening. At sufficiently low Helmholtz number  $ka < 1$ , with the pipe radius  $a$  as the reference geometrical length scale, the sound wave inside the pipe is a one-dimensional plane wave. The momentum equation (2.2) without sources and with negligible viscosity then reads:

$$\frac{\partial(\rho v)}{\partial t} + \frac{\partial p}{\partial x} + \frac{\partial(\rho v^2)}{\partial x} = 0, \quad (4.1)$$

with the pipe positioned along the  $x$ -axis and the only component of the velocity  $v$  is assumed to be parallel to it. Approximating the mean flow inside the pipe as a steady uniform flow, all three quantities can be split into a constant mean flow component (denoted here with index  $J$ , which implies the value of the jet) and a small, purely acoustic perturbation (denoted with the prime symbol). In such a case, the equation can be linearized by suppressing the second- and higher-order terms in the equation. Moreover, the acoustic perturbation quantities scale as (see the comments following the equation (2.109) and the equation (2.99)):  $p' \sim c_J^2 \rho' \sim \rho_J c_J v'$ , where  $c_J$  denotes the speed of sound inside the pipe. Assuming further low value of the Mach number  $M_J = v_J / c_J$ , the momentum equation simplifies to:

$$\frac{\partial p'}{\partial x} \approx -\rho_J \frac{\partial v'}{\partial t}. \quad (4.2)$$

Therefore, the incident sound wave contributes to the exterior radiation by the injection of its momentum, which is given on the right-hand side of the last equation, through the pipe's cross section. This radiation can be considered to be omnidirectional and represented with a point monopole source located at the centre of the pipe opening, for approximately any  $ka < 0.5$ , as shown by Levine and Schwinger in the no-flow case [LS48]. It is important to notice that the mean flow has no effect

on the far-field directivity of this contribution. Convective amplification is the property of the source, rather than a pure sound propagation phenomenon [Mas16], and takes place only at the location of the actual sound source, which is in this case inside the pipe far from the opening. Therefore, convection of the incident sound inside the pipe cannot cause any angularly dependent radiation outside the pipe. An analytical proof of this is practically omnidirectional radiation from an open pipe immersed in a mean flow, that is, when the mean flow velocity is equal inside and outside the pipe. Munt's solution [Mun77] at low frequencies in this case gives no pronounced radiation in any particular direction, similarly as in the absence of the mean flow. In contrast to this, a free-space monopole inside a uniform flow results in a pronounced convective amplification pattern compared to the no-flow case. It is interesting that many authors [Rib96, Bos13, How98] tend to explain the directivity of a pipe with a jet as the effect of convection, even at low frequencies when flow-induced sound generation by the free jet outside the pipe is negligible and the main source of sound is located inside the pipe. Instead, the pronounced far-field directivity at low frequencies is mainly a consequence of the vortex-sound interaction which governs the sound diffraction at the pipe edge. This will be discussed in more details in the next subsection.

Far-field sound pressure due to the monopole component can now be estimated as the solution of the classical wave equation (2.110), with the momentum of the incident sound wave from the equation (4.2) as the source of the perturbation, which is injected through a plane control surface inside the pipe normal to the axis of symmetry. The control surface can be shifted from the opening, in the region of uniform flow, in order to avoid the influence of the pipe opening. The acoustic pressure at the location defined with vector  $\mathbf{x}$ , which is outside the pipe and far from the opening (the centre of the pipe opening is at  $\mathbf{x} = 0$ ), is given by:

$$p_m'(\mathbf{x}, t) = -\frac{1}{4\pi|\mathbf{x}|} \iiint_V \frac{\partial}{\partial x} \left( \rho_J \frac{\partial v'}{\partial t} \right) dV = \frac{1}{4\pi|\mathbf{x}|} \iint_S \rho_J \frac{\partial v'}{\partial t} dS \approx \frac{\rho_J \omega v' (a^2 \pi)}{4\pi|\mathbf{x}|}, \quad (4.3)$$

where  $\omega$  denotes the angular frequency of the sound and  $a$  is the radius of the pipe. This also agrees with [How98] for the case of a cold jet ( $\rho_J = \rho_\infty$ , where the index  $\infty$  indicates the value at infinity, that is, far from the jet).

## 4.2 Vortex-sound interaction

When the incident sound wave reaches the thin trailing edge of the rigid pipe, it is diffracted in all directions and at all angles to the pipe axis. At low frequencies and without a mean flow, the resulting radiation is nearly omnidirectional [LS48], since the opening of the pipe acts as a compact source of the sound, as perceived by the listener in the far field outside the pipe ( $a$  is the only relevant geometric characteristic length scale and, since  $ka < 1$ , the radius of the pipe is much smaller than the wavelength of the sound). The contribution of the vortices which are shed from the pipe edge and only acoustically driven is of the second order and, therefore, negligible for small acoustic perturbations. However, this becomes substantially different when the pipe exhausts even a steady jet and even with low Mach number value. High mean flow speed gradient which is established at the sharp edge leads to the formation of an unstable shear layer of vortical flow, which ensures the finiteness of the flow parameters at the edge. This effect is well known in the theory of aerodynamics and often referred to as Kutta condition [How98] or Joukowski's hypothesis [Bat02]. The analogous phenomenon which is responsible for the formation of vortices in unsteady flows is treated in the aeroacoustic literature with the so-called unsteady Kutta condition [RH16]. In the presence of high gradients at the edge, the solenoidal perturbations in unsteady flows can easily become comparable and interact with the acoustic waves, which themselves consist an unsteady part of the flow.

At low frequencies and low Mach numbers, when the typical length scale of the vortices is much smaller than the acoustic wavelength, vortical flow is essentially silent [RH16], since the sound is the irrotational perturbation of the flow, as discussed in Chapter II. In such a case, vortices can generate sound only through the interaction with a solid body, which is typically the edge from which the vortices are shed. If the body is rigid and the Mach number of the flow is low, the aeroacoustic dipole [Cur55, FH69] is more efficient radiator than the quadrupole source due to the free jet [Lig52], since the powers of the two (compact) sources scale as  $M^2 : M^4$ , respectively. However, in most of the cases when a low frequency sound source exists inside the pipe (for example, an internal combustion engine at the beginning of the exhaust system) and acts as a monopole in the sense of the previous subsection, it will

dominate over both dipole and quadrupole contributions. For this reason, we will neglect any flow-induced sound in the same way as such contributions were suppressed during the laboratory measurements which were described in Chapter III.

On the other hand, sound waves, being an unsteady perturbation of the flow, can also provide the kinetic energy for the generation of vortices at the trailing edge. In such a process, the energy spent for the creation of vortices is lost for the sound waves and the vortices essentially act as an acoustic sink. This mechanism of sound attenuation is by far dominant over the flow-induced sound generation at low frequencies, due to the inefficiency of the latter one. However, the presence of the solid body also means that a part of the acoustic energy, which was lost inside the vortex, will ultimately be retrieved by the action of the vortices on the edge. Since the kinetic energy of the vortices in this case originates from the incoming acoustic wave, we cannot speak about a pure aeroacoustic source, although the mechanism of energy exchange is principally the same. It is actually this “secondary” dipole source at the edge of the pipe, which will have the major effect on otherwise omnidirectional radiation from the pipe at low frequencies. Its strength relative to the monopole source determines the overall shape of the far-field radiation pattern. In addition to this, the strength of the acoustic sink due to the prior vortex generation determines the total radiated power.

To quantify the dipole source, we start again with the inviscid form of the momentum equation (2.2), omitting all sources on the right-hand side:

$$\frac{\partial(\rho\mathbf{v})}{\partial t} + \nabla p + \nabla \cdot (\rho\mathbf{v}\mathbf{v}) = 0. \quad (4.4)$$

The momentum equation can be reshaped into a form which is more suitable for studying the effect of the vortex-sound interaction at the edge of the pipe by utilizing the vector identities:

$$\nabla \cdot (\rho\mathbf{v}\mathbf{v}) = \rho\mathbf{v} \cdot \nabla\mathbf{v} + \mathbf{v}\nabla \cdot (\rho\mathbf{v}) \quad (4.5)$$

and

$$\mathbf{v} \cdot \nabla\mathbf{v} = \frac{1}{2}\nabla v^2 + \boldsymbol{\omega} \times \mathbf{v}, \quad (4.6)$$

where  $\boldsymbol{\omega}$  denotes vorticity vector defined with  $\boldsymbol{\omega} = \nabla \times \mathbf{v}$ . Thus, we obtain:

$$\frac{\partial(\rho\mathbf{v})}{\partial t} + \nabla p + \frac{1}{2}\rho\nabla v^2 + \rho\boldsymbol{\omega} \times \mathbf{v} + \mathbf{v}\nabla \cdot (\rho\mathbf{v}) = 0. \quad (4.7)$$

Using the conservation of mass, the equation (2.1) with  $m = 0$ , the last term on the left-hand side of the equation (4.7) can be rewritten as  $-\mathbf{v}\partial\rho/\partial t$ , so the equation can be simplified to:

$$\rho \frac{\partial\mathbf{v}}{\partial t} + \nabla p + \frac{1}{2}\rho\nabla v^2 + \rho\boldsymbol{\omega} \times \mathbf{v} = 0. \quad (4.8)$$

As before, we assume small<sup>8</sup> unsteady perturbations of the mean flow and ignore the second-order terms to obtain (static pressure is assumed to be constant in the round jet, say, 101kPa everywhere):

$$\rho_0 \frac{\partial\mathbf{v}'}{\partial t} + \nabla p' = -\frac{1}{2}\rho'\nabla v_0^2 - \rho_0\nabla(\mathbf{v}_0 \cdot \mathbf{v}') - (\rho_0\boldsymbol{\omega} \times \mathbf{v}'). \quad (4.9)$$

For low Mach number values, the flow around the edge can be considered to be incompressible with  $\rho_0 = \rho_j$ . Using the uniform mean flow as the reference, we notice that the dominating term which involves the interaction of the forming vortex with the incoming acoustic wave has the form of the Coriolis force:  $(\rho_j\boldsymbol{\omega} \times \mathbf{v})'$  [Pow64]. In the first instance, it will represent an acoustic sink, as already discussed. However, we are interested here in estimating the dipole radiation as this force acts back on the pipe wall, the reaction of which (therefore, the change of the sign in the following equation, which is due to the change of the direction of the force vector) “regenerates” the sound. Thus, the resulting far-field pressure equals:

$$p_d'(\mathbf{x}, t) = \frac{1}{4\pi|\mathbf{x}|} \iiint_V \nabla \cdot (\rho_j\boldsymbol{\omega} \times \mathbf{v})' dV. \quad (4.10)$$

Next, we follow the approach of Hirschberg and Hoeijmakers [HH14], based on Howe’s Vortex Sound Theory [How79] and expect the axial component (denoted with the subscript  $_x$ ) of the Coriolis force per unit volume (represented by the term  $(\rho_j\boldsymbol{\omega} \times \mathbf{v})'_x$ ), to generate the vortex ring at the pipe edge. The volume integral in the equation (4.10) can then be estimated as:

$$\iiint_V \frac{\partial}{\partial x} (\rho_j\boldsymbol{\omega} \times \mathbf{v})'_x dV \approx \frac{\partial}{\partial x} \left( \rho_j \frac{d(S_\omega \Gamma')}{dt} \right), \quad (4.11)$$

---

<sup>8</sup> Only the perturbations of the acoustic amplitude are considered. Since only sound propagation is treated, nonlinear flow-induced noise generation is excluded from the consideration.

where  $\Gamma$  and  $S_\omega$  represent the circulation ( $\Gamma = \oint_C \mathbf{v} \cdot d\mathbf{l}$ ) and the surface of the vortex ring, respectively. When the edge of the pipe is sharp, the shear-layer has a very small thickness and we can approximate  $S_\omega \approx a^2 \pi$ .

The acoustic dipole which is parallel to the pipe axis is a result of the reaction force of the pipe wall to the axial force induced by the vortex. This is described with the relation:

$$\rho_J \frac{d(S_\omega \Gamma')}{dt} \approx -S_\omega p_{ic}', \quad (4.12)$$

where  $p_{ic}'$  denotes the incompressible pressure at the edge due to the vortex. This result will be used in Chapter VI for the formulation of the boundary condition at the edge, in order to include the effect of the vortex within the numerical solution of the irrotational acoustic perturbation. The amount of the circulation shed at the pipe edge is equal to:

$$\frac{d\Gamma'}{dt} = \left( \frac{d\Gamma}{dx} \frac{dx}{dt} \right)', \quad (4.13)$$

Here,  $dx/dt$  represents the convection velocity of vorticity perturbations, which can be roughly approximated as  $(v_J + v')/2$ , that is, the average velocity between the (uniform) jet and the still surrounding. Moreover,  $d\Gamma/dx \approx v_J + v'$ , which in the first-order approximation gives:

$$\frac{d\Gamma'}{dt} \approx \left( \frac{(v_J + v')^2}{2} \right)' \approx v_J v'. \quad (4.14)$$

Inserting this in the volume integral of the equation (4.11) and then the equation (4.10), the far-field sound pressure can be estimated as:

$$p_d'(\mathbf{x}, t) \approx \frac{\rho_J v_J v' (a^2 \pi) k_\infty}{4\pi |\mathbf{x}|} \cos(\theta) = \frac{\rho_J \omega v' (a^2 \pi)}{4\pi |\mathbf{x}|} M_J \frac{c_J}{c_\infty} \cos(\theta) = p_m' M_{ac} \cos(\theta), \quad (4.15)$$

where  $M_{ac} = v_J/c_\infty = M_J c_J/c_\infty$  is acoustic Mach number, which is equal to the local Mach number for cold jets and larger if the jet is heated. Additional multiplication with cosine function characterizes the radiation pattern of the dipole and is due to the orientation of the dipole and the force parallel to the pipe axis and the three-dimensional spatial derivative in the equation (4.10).

Unlike the monopole source at the pipe exit, which is not convected, the dipole source is located just outside the pipe and inside the jet, which leads to the convective amplification of this source contribution. If the flow around the edge is approximated as uniform, the convective amplification has an analytical solution [Del14] and the far-field sound pressure due to the dipole becomes:

$$p_d'(\mathbf{x}, t) \approx p_m' \frac{M_{ac}}{(1 - M_{ac}^2) \sqrt{1 - M_{ac}^2 \sin^2(\theta)}} \left( \frac{\cos(\theta)}{\sqrt{1 - M_{ac}^2 \sin^2(\theta)}} - M_{ac} \right). \quad (4.16)$$

Obviously, the convective amplification factor is then proportional to  $M_{ac}^2$ , which makes it negligible for low Mach number flows. In addition to this, certain effects of shadowing in the rear half-space by the opening of the pipe should also be expected at higher frequencies. Since these contributions scale roughly as  $\sim (ka)^2$  (for example, shadowing of a rigid sphere with the radius  $a$  [Kut07]) and we are interested in low Helmholtz numbers, we will neglect this effect.

It is interesting to note here that Howe in his work [How98] approximates the dipole contribution for a cold jet ( $M_J = M_{ac}$ ) as:  $p_d'(\mathbf{x}, t) \approx 2p_m' M_J \cos(\theta)$ , that is, two times higher value than the one obtained here. This seems to be the consequence of two additional effects which are taken into account by Howe:

- convective amplification of the incident sound inside the pipe, which is proportional to the Mach number, and
- Coriolis force acting on the pipe in the radial direction.

The first effect seems to be physically unjustified for the exterior sound radiation, when the main source of the sound is placed deep inside the pipe. On the other hand, it seems reasonable that the radial Coriolis force has a negligible contribution due to the axial symmetry of the problem and the acoustical compactness of the pipe opening. In fact, including the additional scaling factor of two leads to the significant overestimation of the dipole contribution, when compared with the measurement results presented here (see the graphs with the results below).

### 4.3 Refraction

Unlike convective amplification, refraction is a pure sound propagation phenomenon. It is a change of the direction of propagation of a sound inside an inhomogeneous medium. In steady flows, the inhomogeneity which leads to the spatially varying effective sound speed can be due to the non-uniformity of either temperature or mean flow velocity. In the case of an open circular pipe exhausting a round jet, the spatially distributed non-uniformity is limited to the mixing region of the jet, in front of the pipe opening, where the mean flow parameters spatially decay to meet the conditions inside the surrounding still gas far from the opening. As shown in the previous chapter, the effect of the refraction is significant only at small angles to the pipe axis, within the zone of relative silence, when the apparent thickness of the mixing region (which is at the axis typically of order  $\sim O(10a)$  [Wit74]) is comparable to the sound wavelength, at sufficiently high Helmholtz numbers, say,  $ka > 0.2$ . As the thickness of the mixing region decreases with the increase of the angle to the pipe axis (becoming as small as the thickness of the shear-layer at the pipe edge at  $\theta = 90^\circ$ ), the refraction effects become negligible.

Being a spatially distributed phenomenon, refraction is more difficult to approximate explicitly compared to the compact monopole and dipole sources which were treated so far. An obvious exception is the trivial case when the mixing region is acoustically compact and the refraction is negligible<sup>9</sup>. On the other hand, most of the analytical solutions for the refraction problems which can be found in literature, consider just the opposite extreme, when the flow characteristics change over space much “slower” than the acoustic variables, that is, when the sound wavelengths are much smaller than the typical length scales of the flow. This high-frequency approximation, known as “ray acoustics” or “geometrical acoustics” [OW16, CDF+92], is successfully used for modelling sound propagation at large distances, for example, in stratified atmosphere. However, it is not suitable for low frequencies which are considered in this work, or whenever the Helmholtz number does not satisfy inequality  $ka \gg 1$ . In fact, the basic ray acoustics approach implemented on the jet noise would inevitably

---

<sup>9</sup> Munt’s model of a uniform flow also assumes an infinitely thin shear-layer in the continuation of the pipe wall. This implies a vanishing mixing region, as well, and makes the estimation of the refraction very crude.

lead to the zero-radiation along the pipe axis and the overestimation of the zone of silence. Fortunately, this zone is very narrow in round jets and most of the applications in practice do not require very accurate estimation of the refraction effects. We will, therefore, take a very crude approach, by estimating the attenuation due to the refraction as originating from distributed artificial acoustic sinks in a similar way as Lighthill's aeroacoustic analogy is used for the estimation of free-space aeroacoustic sources.

Assuming small unsteady perturbations of the low Mach number mean flow with constant static pressure everywhere, including the mixing region, the inviscid and linearized momentum equation (2.8) can be written as ( $\mathbf{f} = 0$ ):

$$\frac{\partial \mathbf{v}'}{\partial t} + \frac{\nabla p'}{\rho_0} + (\mathbf{v} \cdot \nabla \mathbf{v})' = 0. \quad (4.17)$$

As with Lighthill's analogy, the reference flow is the cold quiescent fluid at infinity and the relevant "sound sources" are described by the terms:

$$-\left( \frac{\nabla p'}{\rho_0} - \frac{\nabla p'}{\rho_\infty} \right) - (\mathbf{v} \cdot \nabla \mathbf{v})' = -\frac{\nabla p' T_0 - T_\infty}{\rho_0 T_0} - (\mathbf{v} \cdot \nabla \mathbf{v})', \quad (4.18)$$

where the perfect gas equation (2.45) for a steady flow with constant static pressure was used for the last expression. The first term is then attributed to the refraction due to the temperature gradient and the second one due to the variations of the mean flow velocity. The contribution of the refraction to the far-field sound pressure is thus:

$$p_r'(\mathbf{x}, t) = -\frac{1}{4\pi|\mathbf{x}|} \iiint_V \rho_0 \nabla \cdot \left[ \frac{\nabla p' T_0 - T_\infty}{\rho_0 T_0} + (\mathbf{v} \cdot \nabla \mathbf{v})' \right] dV, \quad (4.19)$$

where the second term can be expanded as  $\nabla \cdot (\mathbf{v} \cdot \nabla \mathbf{v})' = \nabla \cdot (\boldsymbol{\omega} \times \mathbf{v})' + \nabla(\mathbf{v} \cdot \mathbf{v})'/2$ .

The influence of compact vortices on the sound propagation is neglected and in the first order approximation  $(\mathbf{v} \cdot \mathbf{v}/2)' \sim v_0 v'$ . We also approximate  $p' \sim \rho_0 c_0 v'$  in the first term in the parentheses and the two spatial derivatives we scale as  $\sim 1/\lambda^2$ . Assuming that the mixing region has only one relevant dimension, its thickness, which is a function of the angle to the axis, say,  $L(\theta)$ , we estimate the volume integral as  $a^2 \pi L(\theta)$ . For the mean flow variables we take the values of the uniform jet, that is,  $\rho_0 \rightarrow \rho_J$ ,  $v_0 \rightarrow v_J$ , and  $T_0 \rightarrow T_J$ . This very crude simplification should serve for a

rough estimation of the refraction effects in an integral sense. Furthermore, the parameter  $L(\theta)$ , seen as the path length of the sound, has already been used in the literature for characterisation of the zone of relative silence [Lus71]. As the pressure contribution is negative, refraction behaves as an “acoustic sink” distributed throughout the mixing region. Putting everything together in the equation (4.19) gives the following estimation of the attenuation inside the zone of relative silence:

$$\begin{aligned}
p_r'(\mathbf{x}, t) &\approx -\frac{(a^2 \pi) L(\theta) \rho_j v'}{4\pi |\mathbf{x}| \lambda^2} \left( c_j \frac{T_j - T_\infty}{T_j} + v_j \right) \\
&= -\frac{(a^2 \pi) \rho_j v' \omega}{4\pi |\mathbf{x}|} \frac{L(\theta)}{2\pi \lambda} \left( \frac{T_j - T_\infty}{T_j} + M_j \right) \\
&= -p_m' \left( \frac{T_j - T_\infty}{T_j} + M_j \right) \frac{L(\theta)}{(2\pi)^2 a} ka.
\end{aligned} \tag{4.20}$$

The introduced thickness of the mixing region has to be evaluated empirically. It should decay fast with the angle to the axis  $\theta$  and approach the thickness of the pipe wall at  $\theta = 90^\circ$ . In the following, we choose the exponential function  $L(\theta) = 100a \exp(-4.5\theta)$ , which at the pipe axis takes the value of 100 pipe radiuses. This length corresponds roughly to the decay of the maximum jet velocity at the axis to 10% of its value [Wit74] and covers the entire order of magnitude of the characteristic length scales of the jet, which are typically  $\sim 10a$ . Since  $L(\theta = \pi/2) \approx 1.7\text{mm}$ , the estimated thickness of the mixing region at the pipe edge reasonably approaches the thickness of the pipe wall, which was in the laboratory measurements (Chapter III) 0.5mm and in the numerical simulation (Chapter VI) set to 2mm.

The range of validity of the proposed refraction model is expected to be limited by the upper value of Helmholtz number. This limit is due to the fact that already at moderately high Helmholtz number values, such as  $ka > 0.3$ , the mixing region thickness at the axis becomes much larger than the sound wavelength and the approximation of the spatial derivatives based only on the wavelength,  $1/\lambda$ , as done here, becomes inappropriate. Sound propagation in such a case can be estimated using the ray acoustics theory.

## 4.4 Estimation of the far-field radiation

Summarizing the results above, that is, equations (4.3), (4.16), and (4.20), the shape of the radiation pattern outside a pipe with a hot mean flow can be approximated as:

$$RP(\theta) = 20 \log_{10} \left[ 1 + M_{ac} \cos(\theta) - \left( \frac{T_J - T_\infty}{T_J} + M_J \right) \frac{L(\theta)}{(2\pi)^2 a} ka \right], \quad (4.21)$$

or, including also the convection of the dipole source, equation (4.16):

$$RP(\theta) = 20 \log_{10} \left[ 1 + \frac{M_{ac}}{(1 - M_{ac}^2) \sqrt{1 - M_{ac}^2 \sin^2(\theta)}} \left( \frac{\cos(\theta)}{\sqrt{1 - M_{ac}^2 \sin^2(\theta)}} - M_{ac} \right) - \left( \frac{T_J - T_\infty}{T_J} + M_J \right) \frac{L(\theta)}{(2\pi)^2 a} ka \right]. \quad (4.22)$$

Figure 4.1 shows the radiation patterns estimated with the equation (4.22) for different mean flow conditions, Mach number and temperature values, and Helmholtz number values. The patterns are normalized according to their values at the angle  $\theta = 90^\circ$ , as done in [PB76], and compared with the measured values from the previous chapter and Munt's analytical solution. As in Chapter III, the Mach number values shown in the graphs refer to the maximum values at the pipe axis.

The value of the acoustic Mach number which is utilized by the simple model is also taken at the pipe axis and is, therefore, equal to the measured value. On the other hand, the value of the mean flow velocity which is averaged over the pipe's cross-section is, as before, used for Munt's solution. The former approach based on the maximum value does not agree with the model presented in [HH14], which is mainly concerned with the sound field inside the pipe, but rather with the model used in [BN03]. One of the reasons for this discrepancy could be the underestimation of the convection velocity of the vortices, as done in the equation (4.13), which is taken to be equal to  $(v_j + v')/2$ , that is, the average velocity between the jet and the motionless surrounding medium. This results then in the underestimation of the dipole contribution for a fixed value of Mach number.

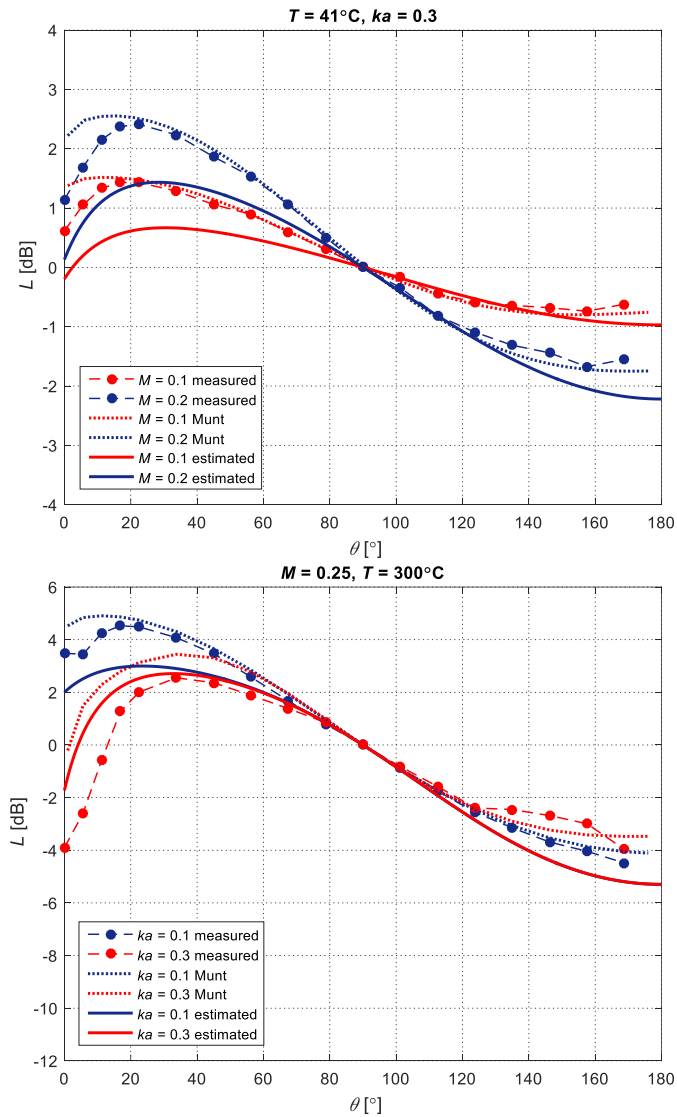


**Figure 4.1:** Comparison of the radiation patterns estimated with the simple model, Munt’s analytical solution, and the laboratory measurements: (above) cold jet, (below) hot jet; normalization for  $\theta = 90^\circ$ .

Still, it appears from Figure 4.1 that the contribution of the dipole according to the model is generally slightly weaker compared to the analytical and experimental results. The difference is around 1dB in the half-space in front of the pipe opening. However, if the normalization based on the total radiated energy is adopted, as in Chapter III, the differences become smaller, as shown in Figure 4.2. The largest discrepancies are now around the angle to the pipe axis  $\theta = 90^\circ$ , and they are below 1dB. On the other hand, the shape of the radiation patterns and the range of sound pressure values between the maximum and minimum radiation is captured very well by the simple model. As already discussed, the advantage of the first normalization,

based on the value at  $\theta = 90^\circ$ , is that the positions of the radiation patterns along the vertical axis do not depend on the accuracy of the estimation of the sound field inside the zone of relative silence. However, the normalization based on the total radiated energy again seems to be more appropriate, since it shows more clearly the ratio between the monopole and dipole contributions.

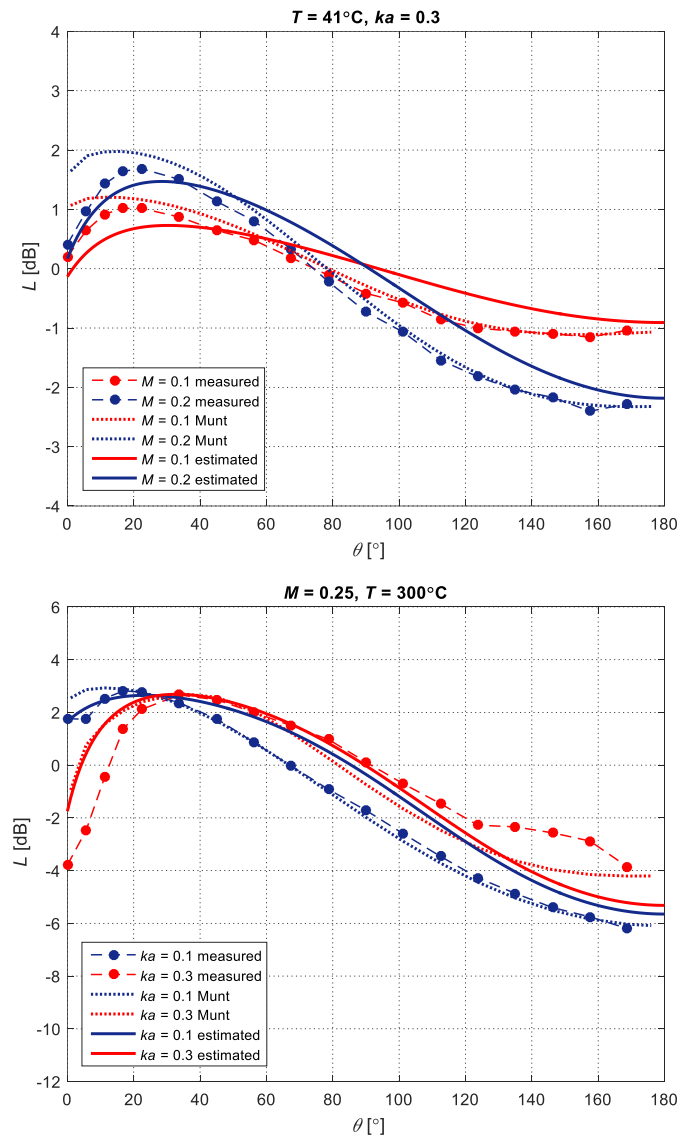


**Figure 4.2:** Comparison of the radiation patterns estimated with the simple model, Munt’s analytical solution, and the laboratory measurements: (above) cold jet, (below) hot jet; normalization based on the total radiated energy.

With regard to the refraction effects inside the zone of relative silence, we can conclude that the introduced model of the mixing region of the jet, which assumes an exponential decay of the mixing region thickness with the angle to the axis, fits

sufficiently well with the measurement results of the far-field radiation patterns. The differences at the lowest angles to the axis are somewhat increased at the highest analysed Mach number ( $M = 0.25$ ), and temperature ( $T = 300^\circ\text{C}$ ) values and for  $ka > 0.3$  (red curves in the lower graph in Figure 4.2), but this should not be of critical importance for the concerned applications.

Following Howe [How98], the simple model of the far-field radiation can also be used for the estimation of the acoustic energy which is lost inside the vortex. The acoustic power of the incoming wave which is transferred (dissipated) into the kinetic energy of the vortex at the pipe edge is given by:

$$P_{diss} \approx \rho_J \iiint_V (\boldsymbol{\omega} \times \mathbf{v}) \cdot \mathbf{v}' dV \approx \overline{\rho_J v_J v'} \iint_S \mathbf{v}' \cdot d\mathbf{S} \approx \rho_J v_J (a^2 \pi) \overline{v'^2}, \quad (4.23)$$

where  $\overline{(\cdot)}$  denotes time average over one period,  $\frac{1}{T} \int (\cdot) dt$ . On the other hand, the total

acoustic power which is radiated into the far field can be calculated by integrating the average acoustic intensity over a surface of a sphere with the radius  $|\mathbf{x}|$  and with the centre located at the centre of the pipe's opening:

$$P_{rad} = \iint_S \overline{p' \mathbf{v}' \cdot d\mathbf{S}} = \iint_S \frac{\overline{p'^2}}{\rho_\infty c_\infty} dS, \quad (4.24)$$

where the plane wave approximation  $p' = v' \rho_\infty c_\infty$  is used for the far field. If we, for simplicity, neglect the drop of the sound pressure in the zone of relative silence due to the refraction, as well as the convection of the dipole source at the edge, the far-field sound pressure is simplified to the sum of the compact monopole and dipole sources:

$$p' = p_m' + p_d' \approx \frac{\rho_J \omega v' (a^2 \pi)}{4\pi |\mathbf{x}|} (1 + M_{ac} \cos(\theta)). \quad (4.25)$$

Using the spherical coordinate system with the origin at the centre of the opening, the total radiated power equals:

$$\begin{aligned}
P_{rad} &= \iint_S \frac{\overline{p'^2}}{\rho_\infty c_\infty} dS \\
&= \int_0^{2\pi} \int_0^\pi \left[ \frac{\rho_J \omega v' (a^2 \pi)}{4\pi |\mathbf{x}|} (1 + M_{ac} \cos(\theta)) \right]^2 \frac{1}{\rho_\infty c_\infty} |\mathbf{x}|^2 \sin(\theta) d\theta d\varphi \\
&= \int_0^\pi \frac{\rho_J^2 \omega^2 \overline{v'^2} (a^2 \pi)^2}{8\pi \rho_\infty c_\infty} (1 + M_{ac} \cos(\theta))^2 \sin(\theta) d\theta \\
&= \frac{\rho_J^2 \omega^2 \overline{v'^2} (a^2 \pi)^2}{8\pi \rho_\infty c_\infty} \left[ \underbrace{\int_0^\pi \sin(\theta) d\theta}_{=2} + 2M_{ac} \underbrace{\int_0^\pi \cos(\theta) \sin(\theta) d\theta}_{=0} \right. \\
&\quad \left. + M_{ac}^2 \underbrace{\int_0^\pi \cos^2(\theta) \sin(\theta) d\theta}_{=2/3} \right] = \frac{\rho_J^2 \omega^2 \overline{v'^2} (a^2 \pi)^2}{8\pi \rho_\infty c_\infty} \left( 2 + \frac{2M_{ac}^2}{3} \right) \\
&= \frac{\rho_J^2 c_J^2 \overline{v'^2} (k_J a)^2 (a^2 \pi)}{\rho_\infty c_\infty} \frac{1}{4} \left( 1 + \frac{M_{ac}^2}{3} \right), \tag{4.26}
\end{aligned}$$

where  $\omega = k_J c_J$  was used for the last equality.

The ratio of the total radiated power and the sum of the total radiated power and the power dissipated by the vortex, which is, thus, the total power introduced by the incident sound wave, equals:

$$\begin{aligned}
\frac{P_{rad}}{P_{rad} + P_{diss}} &= \frac{\frac{\rho_J^2 c_J^2 \overline{v'^2} (k_J a)^2 (a^2 \pi)}{\rho_\infty c_\infty} \frac{1}{4} \left( 1 + \frac{M_{ac}^2}{3} \right)}{\frac{\rho_J^2 c_J^2 \overline{v'^2} (k_J a)^2 (a^2 \pi)}{\rho_\infty c_\infty} \frac{1}{4} \left( 1 + \frac{M_{ac}^2}{3} \right) + \rho_J v_J (a^2 \pi) \overline{v'^2}} \\
&= \frac{(k_J a)^2}{(k_J a)^2 + \frac{\rho_\infty c_\infty}{\rho_J c_J} \frac{4M_J}{1 + \frac{M_{ac}^2}{3}}}, \tag{4.27}
\end{aligned}$$

with  $M_J = v_J/c_J$ . For a perfect gas with constant static pressure, according to the equation (2.45),  $\rho \sim 1/c^2$ , so the ratio becomes (with  $M_{ac} = v_J/c_\infty$ ):

$$\frac{P_{rad}}{P_{rad} + P_{diss}} = \frac{(k_J a)^2}{(k_J a)^2 + \frac{4M_{ac}}{1 + \frac{M_{ac}^2}{3}}}. \tag{4.28}$$

If we further neglect the dipole radiation, as well, which is valid for very low Mach numbers when  $M \rightarrow 0$ , the ratio becomes:

$$\frac{P_{rad}}{P_{rad} + P_{diss}} \approx \frac{(k_J a)^2}{(k_J a)^2 + 4M_{ac}}. \quad (4.29)$$

We notice that, unlike the energy of the sound which is radiated from the pipe into the exterior (rather than reflected back at the opening of the pipe), the losses due to the vortex formation are frequency independent (within the limit of a thin shear layer) and proportional to the mean flow speed. This allows large attenuation of the radiated sound at low frequencies, as reported and experimentally confirmed in [Bec80].

The simple model of the low-frequency sound radiation from an open circular pipe with a low Mach number mean flow, which is presented in this chapter, gives a satisfactory match with the measurement results and mathematically much more involved Munt's solution. As such, it can be used for a quick estimation of the far-field directivity in engineering applications. Although less accurate than Munt's solution, it allows a reasonably accurate estimation, while giving a clear insight into the governing physical phenomena and the vortex-sound interaction at the edge. Moreover, the effect of the refraction within the zone of relative silence around the pipe axis is captured with more accuracy, with the aid of an empirical model of the jet.

A possible immediate application of the model is for the estimation of free-space directivity of a vehicle's tail-pipe as an apparent low-frequency sound source at the lowest orders of an internal combustion engine. With the supposed radius of the pipe  $a = 2\text{cm}$ , the shapes of the radiation patterns for the second order of a four-stroke, four-cylinder engine are shown in Figure 4.3. The normalization is according to the total radiated energy. The results are given for a full throttle constant acceleration from 1500rpm to 5500rpm in the steps of 1000rpm, whereas, the mean flow properties are estimated from the measurement results reported in [Wal01].

Helmholtz number values are well below 0.1 for all considered frequencies of the sound, so the refraction effects are negligible. Still, the directivity deviates strongly from the omnidirectional radiation as the engine speed increases, reaching up to

around 7dB of the difference between the sound pressure level downstream and upstream from the tail-pipe opening. Such pronounced directivity should be taken into account when estimating pass-by noise of a vehicle or transmission of the noise into the vehicle's interior. While the car body is expected to affect the directivity at higher frequencies, it is the mean flow of the exhausted gasses which can be the most prominent cause of a dipole-like directivity even at the lowest frequencies and engine orders. At the same time, the expected reflections from the ground should not have a strong effect on the directivity at low frequencies, when the distance of the pipe's opening from the ground is much smaller than the wavelength of the sound.

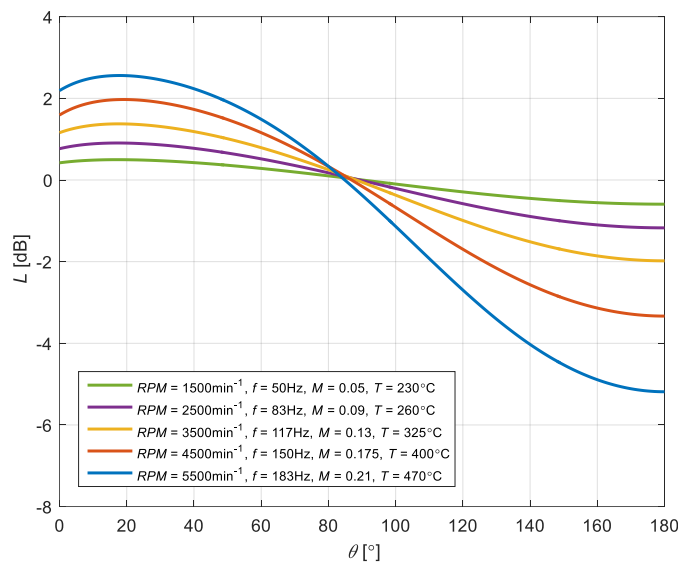


**Figure 4.3:** Estimated shapes of the radiation patterns of the second engine order, during a full throttle constant acceleration, based on the derived model of sound radiation.

## **Chapter V**

# **EQUATION FOR A BODY IN AN INHOMOGENEOUS FLOW**

In this chapter, we derive an equation which is suitable for estimation of the sound field around a moving solid body in an inhomogeneous flow. A non-linear aeroacoustic equation is first derived using a combination of the Ffowcs-Williams and Hawkings (FW-H) equation for a moving body and a quiescent fluid as the reference flow and Phillips' equation for an inhomogeneous flow in free space, without a body. Exact as the other two equations, it should both account for the effects of the body inside the flow and, at least partially, separate the sound propagation effects from the source terms. In fact, the obtained equation represents a convective form of the FW-H equation, which does not imply any type of the mean flow and allows more appropriate treatment of sound propagation phenomena, convection, and refraction, as well as more accurate characterization of the actual sound sources. On the other hand, it introduces the Kirchhoff-like solution for a solid body in Phillips equation, based on the Heaviside function.

Similarly as the other two equations, the non-linear equation cannot be solved without further simplifications of the flow. Therefore, a simplified, linearized version will also be given, which is appropriate for describing the sound propagation outside an open circular pipe with a flow. The linearized equation will point to the key sound propagation and vortex-sound interaction effects in this specific case. However, the linearization will necessarily make the equation less appropriate for describing aeroacoustic sources of essentially non-linear nature, as discussed in Chapter II.

The attempts to obtain the so-called convected Ffowcs Williams and Hawkings equation have been already made in literature [WGW+10, WH95], using the known Green's function for the specific case of a uniform mean flow, such as in wind tunnels. Here, however, we take an approach analogous to the derivation of Phillips' equation, without any assumptions regarding the character of the flow. This leads to a more general formulation which is valid even in highly non-uniform and hot flows.

As a consequence, the obtained differential operator on the left-hand side of the equation does not have a corresponding analytical Green's function, but can be solved numerically. As similar aeroacoustic formulations, possible applications of the equation include fan noise, such as in HVAC systems of vehicles, trailing edge noise of airfoils and helicopter blades, as well as noise generated around solid objects in low Mach number flows, for example, in ducts with mean flow.

## 5.1 Derivation of the equation

We start with the primitive forms of the momentum equations (2.121) and (2.126) and the combination of the equation of state and the energy equation, that is, equations (2.122) and (2.127), for an inviscid flow of a perfect gas ( $\gamma p = \rho c^2$ ) without external sources of mass, force or heat and with negligible heat conduction (isentropic flow):

$$\frac{D\mathbf{v}}{Dt} = -\frac{1}{\rho}\nabla p = -c^2\nabla\Pi \quad \text{and} \quad (5.1)$$

$$\nabla \cdot \mathbf{v} = -\frac{1}{\rho c^2} \frac{Dp}{Dt} = -\frac{D\Pi}{Dt}. \quad (5.2)$$

As before, the differential operator  $D/Dt$  represents the total derivative and  $\Pi$  is the Phillips' dimensionless parameter defined with the equation (2.123). Following the approach of Ffowcs Williams and Hawkings, we multiply both equations with Heaviside function  $H(f)$  to obtain:

$$H \frac{D\mathbf{v}}{Dt} + c^2\nabla(H\Pi) = \Pi c^2\nabla H \quad \text{and} \quad (5.3)$$

$$\frac{D(H\Pi)}{Dt} + H\nabla \cdot \mathbf{v} = \Pi \frac{DH}{Dt}. \quad (5.4)$$

Then we subtract the divergence of the first equation from the total derivative of the second equation and rearrange the terms to obtain:

$$\begin{aligned} & \frac{D^2(H\Pi)}{Dt^2} - \nabla \cdot [c^2\nabla(H\Pi)] \\ &= \nabla \cdot \left( H \frac{D\mathbf{v}}{Dt} \right) - \frac{D}{Dt} (H\nabla \cdot \mathbf{v}) - \nabla \cdot (\Pi c^2\nabla H) + \frac{D}{Dt} \left( \Pi \frac{DH}{Dt} \right). \end{aligned} \quad (5.5)$$

Using the product rule for the expansion of the first two terms on the right-hand side of the equation gives:

$$\begin{aligned}
\frac{D^2(H\Pi)}{Dt^2} - \nabla \cdot [c^2 \nabla(H\Pi)] &= H \left[ \nabla \cdot \left( \frac{D\mathbf{v}}{Dt} \right) - \frac{D}{Dt} (\nabla \cdot \mathbf{v}) \right] \\
&\quad + \frac{D\mathbf{v}}{Dt} \cdot \nabla H - (\nabla \cdot \mathbf{v}) \frac{DH}{Dt} - \nabla \cdot (\Pi c^2 \nabla H) + \frac{D}{Dt} \left( \Pi \frac{DH}{Dt} \right) \\
&= H \left[ \nabla \cdot (\mathbf{v} \cdot \nabla \mathbf{v}) - \mathbf{v} \cdot \nabla \nabla \cdot \mathbf{v} \right] + \frac{D\mathbf{v}}{Dt} \cdot \nabla H - (\nabla \cdot \mathbf{v}) \frac{DH}{Dt} \\
&\quad - \nabla \cdot (\Pi c^2 \nabla H) + \frac{D}{Dt} \left( \Pi \frac{DH}{Dt} \right).
\end{aligned} \tag{5.6}$$

Now we can use the equality  $DH/Dt = \partial H/\partial t + \mathbf{v} \cdot \nabla H = (\mathbf{v} - \mathbf{v}_B) \cdot \nabla H$ , where  $\mathbf{v}_B$  is the velocity of the body, to obtain:

$$\begin{aligned}
\frac{D^2(H\Pi)}{Dt^2} - \nabla \cdot [c^2 \nabla(H\Pi)] &= H \left[ \nabla \cdot (\mathbf{v} \cdot \nabla \mathbf{v}) - \mathbf{v} \cdot \nabla \nabla \cdot \mathbf{v} \right] \\
&\quad + \left[ \frac{D\mathbf{v}}{Dt} - (\nabla \cdot \mathbf{v})(\mathbf{v} - \mathbf{v}_B) \right] \cdot \nabla H - \nabla \cdot (\Pi c^2 \nabla H) + \frac{D}{Dt} \left[ \Pi (\mathbf{v} - \mathbf{v}_B) \cdot \nabla H \right]
\end{aligned} \tag{5.7}$$

This non-linear equation is exact for any inviscid and isentropic flow of a perfect gas. However, to make it solvable, more information on the flow is needed. If the static value of the pressure is constant everywhere,  $p_0 = p_\infty$ , such as in the parallel shear flow exhausted from the pipe, the steady value of Phillips' parameter is equal to zero and the equation (2.133) gives  $\Pi = \Pi' \approx p' / (\gamma p_\infty)$ , within the first-order approximation. The linearized equation for small acoustic perturbations of the flow, thus, becomes:

$$\begin{aligned}
\frac{D_0^2(Hp')}{Dt^2} - \nabla \cdot [c_0^2 \nabla(Hp')] &= \gamma p_\infty \left\{ H \left[ \nabla \cdot (\mathbf{v} \cdot \nabla \mathbf{v}) - \mathbf{v} \cdot \nabla \nabla \cdot \mathbf{v} \right] \right\}' \\
&\quad + \gamma p_\infty \left\{ \left[ \frac{D\mathbf{v}}{Dt} - (\nabla \cdot \mathbf{v})(\mathbf{v} - \mathbf{v}_B) \right] \cdot \nabla H \right\}' - \nabla \cdot (p' c_0^2 \nabla H) \\
&\quad + \frac{D_0}{Dt} [p' (\mathbf{v} - \mathbf{v}_B) \cdot \nabla H],
\end{aligned} \tag{5.8}$$

with  $D_0/Dt = \partial/\partial t + \mathbf{v}_0 \cdot \nabla$ . Such linearization of the equation (5.7) inevitably leads to the loss of potentially significant sources of flow-induced noise and is in general not acceptable for the estimation of pure aeroacoustic sources. However, the equation (5.8) is still suitable for assessment of the linear vortex-sound interaction at the trailing edge of a pipe with a mean flow (see Chapter 4).

The first term on the right-hand side of the equation represents the remaining (linearized) free-space source, which was contained inside the Reynolds stress contribution ( $\rho \mathbf{v}\mathbf{v}$ ) in the classical formulation of FW-H. Other parts of the Reynolds stress, which are associated solely with sound propagation, are now shifted to the left-hand side of the equation. As with the FW-H equation or Lightill's analogy, if this term is relevant, it has to be estimated before the calculation of the sound field. However, the equation (5.8) allows more insight into its nature, after noticing that:

$$\begin{aligned} \mathcal{P}_\infty \{H[\nabla \cdot (\mathbf{v} \cdot \nabla \mathbf{v}) - \mathbf{v} \cdot \nabla \nabla \cdot \mathbf{v}]\}' \\ = \rho_\infty c_\infty^2 \{H[\nabla \cdot (\boldsymbol{\omega} \times \mathbf{v} + \nabla(v^2/2)) - (\mathbf{v} \cdot \nabla^2 \mathbf{v} + \mathbf{v} \cdot \nabla \times \boldsymbol{\omega})]\}', \end{aligned} \quad (5.9)$$

where  $\boldsymbol{\omega} = \nabla \times \mathbf{v}$  is the vorticity vector. Here, we recognize the divergence of the linearized Coriolis force per unit volume,  $\rho_\infty \nabla \cdot (\boldsymbol{\omega} \times \mathbf{v})'$ , which is the dominating component of the free-space term for low Mach number flows [Pow64], as also pointed out in the previous chapter.

If the body does not vibrate, the rest of the terms on the right-hand side of the equation (5.8) can also be interpreted as scattering of the sound, which originates from the free-space source, from the body's surface [Pow60]. It is interesting to note that within the linear approximation, the main source of "loading" noise of a motionless rigid body ( $\mathbf{v} = \mathbf{v}_B = 0$  at the surface), which is due to the pressure force acting on the body,  $-\nabla \cdot (p' c_0^2 \nabla H)$ , remains almost identical as in the classical formulation of FW-H, equation (2.146). However, the latter one assumes constant reference value of the sound speed,  $c_\infty$ , while in the equation (5.8), more general  $c_0$  can have any spatial distribution, which makes it more appropriate for inhomogeneous hot flows.

Although the derived equation separates sound sources from sound propagation effects in the moving and/or inhomogeneous medium outside the control surface, the split is not complete, as some of the propagation effects are still contained in the free-space source term. This is a proven limitation of Phillips' equation [Doa72], as well, which has motivated more accurate Lilley's formulation of the free-space analogy for parallel shear flows [Lil74]. Lilley's approach results in a potentially unstable third-order wave operator on the left-hand side of the equation. Simpler second-order wave

operator of Phillips' equation, which is obtained here, does not involve linear instabilities as a solution, which makes it more robust and efficient for numerical calculations. It also reduces to the wave operators of classical and convected wave equations in quiescent fluids and uniform flows, respectively, which is not the case with the operator of Lilley's equation.

In its non-linear, exact form, the equation is not easier to solve than any other aeroacoustic analogy, such as the classical FW-H equation. However, compared to FW-H, it represents more accurately the mechanisms of free-space aeroacoustic sound generation, convective amplification, refraction, and other sound propagation effects in inhomogeneous flows, within the applicability of Phillips' formulation. In order to arrive at a solvable acoustic pressure formulation, the linearization had to be introduced. The following subsection will demonstrate on a simple example the advantage of such obtained wave operator.

## **5.2 A simple example of a point dipole in a non-uniform hot flow**

The following example should briefly illustrate the key advantage of the equation (5.8) over the classical FW-H equation in capturing sound propagation effects in moving and inhomogeneous media. With regard to that, the focus is on the convective left-hand side operator of the derived equation, which presents a more appropriate choice when the propagation effects are not negligible. The right-hand side contains a simple point dipole, which can, for example, represent a source of loading noise due to the unsteady aerodynamic force  $\mathbf{f}' = p' \nabla H$ , which is acting on the surface of an acoustically compact rigid and motionless body. If the control surface is chosen to match the body's surface, the equations (2.146) and (5.8) reduce outside it to:

$$\frac{1}{c_\infty^2} \frac{\partial^2 p'}{\partial t^2} - \nabla^2 p' = -\nabla \cdot \mathbf{f}', \text{ and} \quad (5.10)$$

$$\frac{D_0^2 p'}{Dt^2} - \nabla \cdot (c_0^2 \nabla p') = -\nabla \cdot (\mathbf{f}' c_0^2), \quad (5.11)$$

respectively, where  $p' = c_\infty^2 \rho'$  (see Chapter II) is used for the former equation. While the first equation is equal to the classical wave equation (2.110) with constant sound speed and the dipole source, the second equation has a form of a convected wave equation in an inhomogeneous medium. To illustrate the difference, we assume a unidirectional mean flow directed along the horizontal  $x$ -axis, with the constant amplitude of the velocity given with  $v_0 = M_\infty c_\infty$ , where  $M_\infty = 0.25$  and  $c_\infty = 343\text{m/s}$ . The temperature is assumed to be non-uniform with the spatial distribution of the sound speed  $c_0$  given in Figure 5.1. The spatially varying sound speed has an exponential decay from the centreline of the domain in the positive and negative directions of the vertical axis. Such a narrow profile should represent a highly inhomogeneous medium, such as in a hot jet exhausted from an open pipe.

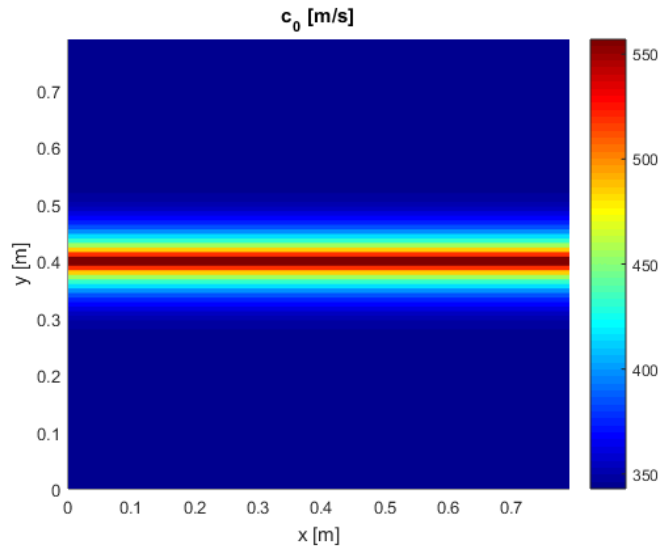


**Figure 5.1:** Sound speed profile used for the estimation of sound propagation in an inhomogeneous flow with equations (5.10) and (5.11).

The numerical solutions of both equations are shown in Figure 5.2 for the plane domain with the point source located at the centre of the domain. The unsteady force is assumed to have a sinusoidal time dependency  $\sim \sin(2\pi ft)$ , with the frequency  $f = 1000\text{Hz}$ . Finite Element Method is used for the calculations with simple linear shape functions and square elements. Spatial and temporal resolutions of the calculations are, respectively, 8mm and  $3\mu\text{s}$ . Both graphs in Figure 5.2 represent the acoustic pressure distribution at the time instance  $t = 0.72\text{ms}$ . The fine rippling in the otherwise silent part of the calculation domain is due to the numerical error.

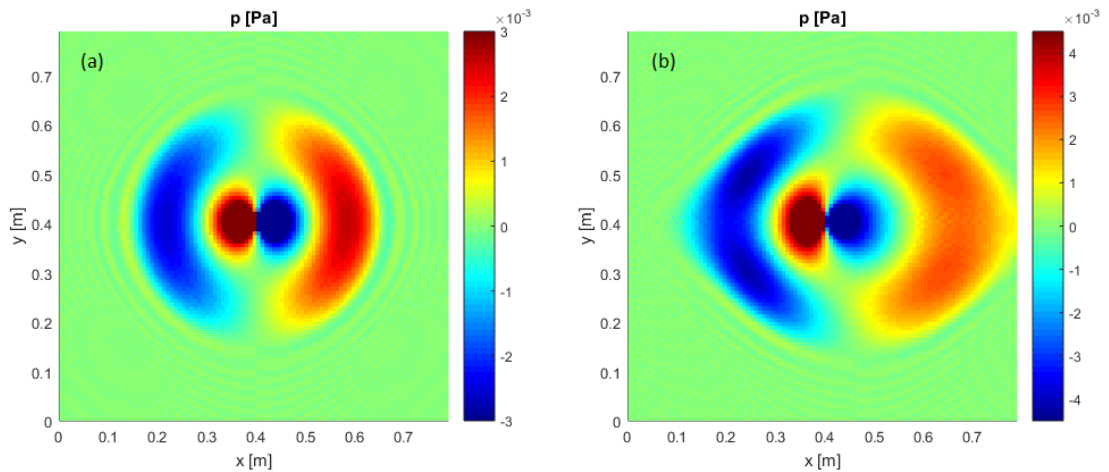


**Figure 5.2:** Solution of the (a) classical and (b) convected wave equation in plane with a point dipole source in the centre of the domain.

Both convective amplification and refraction due to the non-uniform speed of sound can be observed only in Figure 5.2 (b). The convective amplification is recognized as the gain of the sound pressure in the upstream direction (decreasing values at the  $x$ -axis) and the attenuation in the opposite downstream direction. The ratio of the upstream and downstream amplitudes at the centreline, left and right from the source, is close to the value  $(1+M)/(1-M)$ , where  $M$  denotes the Mach number value of the flow relative to the local speed of sound. Another observable effect of the mean flow is the change of the angle to the  $x$ -axis at which the dipole has a zero-radiation, compared to the radiation in a quiescent fluid shown in Figure 5.2 (a). Additional attenuation of sound pressure at the centreline of the domain in Figure 5.2 (b) is due to the refraction inside the hot region of the flow, with high gradient of the sound speed. Finally, spatial expansion of the wave downstream and contraction upstream are due to the apparent wavelength of the sound, which depends on the effective local mean flow speed.

### 5.3 Discussion

One of the main points of this chapter is to show that classical Ffowcs Williams and Hawkings equation is not suitable for (aero)acoustic problems in which sound

propagation effects in moving and inhomogeneous media may significantly affect the far-field radiation. Alternatively, the linearized equation (5.8), although to be solved only numerically, gives much better approximation of the resulting acoustic field, when all the sound sources are known.

With regard to the sound radiation from a rigid and motionless pipe with a hot mean flow, the equation showed that apart from the incident sound, the main contribution to the far-field radiation is due to the distribution of the unsteady pressure at its wall, which originates from the vortex shed at the pipe edge. Together with the findings from the previous chapter, it follows that the corresponding unsteady Coriolis force is mainly due to the incompressible pressure at the pipe edge, which is initially induced by the incoming plane sound wave inside the pipe. This conclusion will be used in the next chapter for numerical solution of the pipe problem with a single convected wave equation of the same form as the equation (5.11).

# Chapter VI

## NUMERICAL ESTIMATION OF THE SOUND FIELD

Although physically based and very simple, the model of sound radiation from an open pipe with a flow which is presented in Chapter IV has its stringent limits. Axial symmetry of the geometry and the formation of the vortex rings within a very thin shear layer assume a simple straight-cut opening and a very thin wall of a circular pipe, that is, a sharp trailing edge of the pipe<sup>10</sup>. Even in such circumstances, the approximations hold only for low values of the Mach number of the uniform mean flow inside the pipe and at the opening, as well as low values of the Helmholtz number of the incident sound (with the pipe radius as the reference geometric length scale). It is evident that many practical problems with complex geometries and flow conditions do not satisfy these requirements. For this reason, industrial applications most often necessarily involve numerical calculations of the sound fields in such flows.

Computational efforts which are needed for the numerical calculations of sound radiation in flows, usually given in terms of the processing power and memory requirements, can vary significantly, even several orders of magnitude, depending on the complexity of the equations which are solved. Naturally, it is preferable to solve the simplest possible acoustic equations (or, ideally, a single equation), which at the same time capture all the relevant flow-acoustic interaction effects. These two conflicting requirements are negotiated by a careful choice of the equation(s) for the particular scenario of the flow-acoustic coupling. Table 6.1 summarizes roughly the most common approaches for the numerical treatment of different types of aeroacoustic problems. The complexity of the governing equations and, thus, the computational resources which will be needed, are directly related to the level of the coupling between the acoustic waves and the main flow of the fluid. The table is, of

---

<sup>10</sup> More precisely, the radius of the curvature of the pipe edge (not the thickness of the pipe wall) should be sufficiently small, so that the shear layer of the separated flow is negligibly thin at the edge.

course, not comprehensive, but should give a brief overview of the state of the art and the typical approaches.

**Table 6.1:** Common numerical approaches for flow-acoustic interaction problems.

<b>flow-acoustic interaction</b>	<b>CFD</b>	<b>CA</b>
weak coupling with negligible sound generation	steady RANS	LEE (CWE)
aerodynamically-dominated sound generation	unsteady LES/DES	
strong bidirectional coupling with acoustic feedback	DNS (compressible LES/DES)	

If the geometry of the problem is such that the flow is confined (for example, inside a cavity), the body which confines the flow sometimes behaves as an acoustic resonator, as well (for example, Helmholtz resonator). The unsteady flow in such cases supports the occurrence of acoustic modes, which in return can modulate the original flow. Such back reaction of the acoustic waves is called acoustic feedback. If hydrodynamic and acoustic modes have similar amplitudes, the flow-acoustic coupling is strong and bidirectional. From the computational aspect, this interaction can be accurately solved only with the use of compressible fluid simulations, for example, Direct Numerical Simulations (DNS) or, somewhat less demanding, compressible Large Eddy Simulations (LES) or Detached Eddy Simulations (DES). In any case, the part of the computational domain in which the strong coupling takes place has to be resolved including simultaneously acoustic and hydrodynamic modes, which are both governed by the system of Navier-Stokes equations (Chapter II). Such calculations are computationally very expensive, primarily due to the several orders of magnitude large differences between the common amplitudes of the main flow and acoustic perturbations, as well as their characteristic length scales. Consequently, the hybrid approach, which assumes separate execution of computational fluid dynamics (CFD) and computational acoustics (CA) is always preferable when possible, that is, when the acoustic feedback is weak. This becomes even more important in the industrial context, when the product development time is short. Outside the domain of strong flow-acoustic coupling, sound propagation can be calculated independently from the main flow.

Fortunately, in many practical problems of interest, the acoustic waves have a negligible influence on the main flow and the hybrid approach gives satisfactory results. This is usually the case with free flows or even confined flows, as long as the sound generation is dominated by the hydrodynamic fluctuations, such as in wake modes [Roe07], rather than the occurrence of acoustic resonance. CFD and CA can then be fully decoupled in the entire computational domain. Unsteady CFD, LES or DES, are then used in the first step for the estimation of aeroacoustic sources. Turbulence models used by LES/DES significantly lower the computational efforts compared to DNS, although the total requirements for the CFD are normally still significantly higher compared to the CA. When all the sources of noise are estimated, the acoustic field is calculated in the second step.

As explained in Chapter IV, low frequency sound radiated from an open unflanged pipe is mainly affected by the attenuation and diffraction at the trailing edge due to the vortex-sound interaction and by the refraction in the mixing region of the jet, even at quite low mean flow velocities. Although the coupling between the acoustic waves and the main flow are generally weak, the vortices which are shed from the pipe edge are partly energized by the incoming sound wave and, thus, act as an acoustic sink. The sound energy is then partially regenerated through the action of the vortex on the edge and the dipole radiation. Both sound attenuation and “generation” are driven by the incoming acoustic wave, while the main flow of fluid contributes only with its abrupt but steady spatial changes close to the edge, as well as inside the mixing region. Therefore, steady properties of the main flow are sufficient for the estimation of sound propagation at low frequencies in this particular case study. Indeed, the combination of steady Reynolds-averaged Navier-Stokes (RANS) equations and Linearized Euler Equations (LEE) has been successfully used in literature for solving this type of problems [HRD11, HGB16, DIA12]. The largest benefit with regard to the cases discussed above is in the very low computational costs of steady RANS calculations compared to both LES/DES and DNS.

Whenever the amplitudes of the sound inside the computational domain of CA are small enough to justify the linearization of the equations (neglecting the higher-order terms of the perturbations), sound field can be accurately resolved by solving the

system of Linearized Euler Equations, such as the equations (2.72)-(2.74) or (2.95)-(2.97). This holds both for acoustic and non-acoustic modes, such as vorticity, which might occur, for example, at the trailing edge. Still, it is very often desirable to refer to a simpler system of equation, or, ideally, a single wave equation, in order to further save the computational efforts. Existing CFD solvers, mostly based on the low-order Finite Volume Method [FP02], are well optimized for the solution of Navier-Stokes equations and show remarkable efficiency and robustness. On the other hand, less common calculations of the acoustic propagation based on LEE are often associated with difficulties, such as large computational time and instability of the solution. Alternatively, one can try with solving a simpler system of equations, such as Acoustic Perturbation Equations [ES03, MDR07], or a single equation, for example, Convected Wave Equation (CWE). In the latter case, a simplified model of the main flow is most often needed for the estimation of sound propagation (left-hand side of the equation), such as uniform mean flow in the classical CWE (2.109), or a parallel shear flow in Lilley's equation [Lil74]. The accuracy of the obtained solution then depends on the importance of all the sound propagation phenomena which are omitted through the simplification of the equations.

Another alternative is solving some sort of aeroacoustic analogy. As explained in Chapter II, the problem which frequently arises when an aeroacoustic analogy is implemented is that the sound propagation effects are at least partly pushed to the right-hand side of the wave equation and treated as artificial sources of sound. Such non-physical sound sources inherently depend on the solution of the entire acoustic problem. As a result, the analogy requires the following:

- expansion of the source region over the entire region of space in which the critical sound propagation effects take place, which can lead to very distributed “sound sources” and larger computational requirements, and
- appropriate modelling of the flow and flow-acoustic effects on the sound propagation in this region, which would allow the assessment of such source terms.

Both prerequisites limit the accuracy of aeroacoustic analogies in highly inhomogeneous flows. Still, the analogies remain essential for characterisation of different mechanisms of aerodynamic sound generation and, when used appropriately,

can lead to very efficient calculations by means of a single-unknown acoustic wave equation.

In the following, we implement the hybrid approach for estimation of the sound field around a circular pipe with a hot jet. In the first step, the computational fluid dynamics is based on the solution of steady Reynolds-averaged Navier-Stokes equations. In the second step, the acoustic field is calculated as the solution of both Linearized Euler Equations and a form of Convected Wave Equation.

## **6.1 Computational fluid dynamics**

This subsection describes the computational fluid dynamics calculations of a hot jet exhausted from an unflanged circular pipe with a thin rigid wall. The calculations of Reynolds-averaged Navier-Stokes equations are done in the open-source CFD package OpenFOAM [Ope17], which is Reynolds-averaged Navier-Stokes based on the low-order Finite Volume Method.

### **6.1.1 Calculations setup**

The axisymmetric computational domain is created in OpenFOAM as a three-dimensional volume in the form of a narrow wedge, the ridge of which aligns with the pipe axis. Angle of the ridge is set to  $4^\circ$  and only one volume element fits within the thickness of the wedge. The mesh, which is shown in Figure 6.1, consists of hexahedrons, with two rectangular faces at the sides of the wedge. The size of the rectangular faces is 4mm x 4mm, except within the continuation of the pipe wall, where the radial dimension is 2mm, to match the specified pipe wall thickness of 2mm. The inner radius of the pipe is 2cm and its length is 1m. In order to keep the computational domain small, yet include the majority of the mixing region, the part of the domain which is exterior to the pipe is 1 meter long (in the axial direction), and extends 20cm behind the plane of the pipe opening, 80cm downstream from it, and 20cm in the radial direction from the pipe axis. The entire mesh consists of 46264

elements and 63921 nodes. Such a mesh is, nevertheless, too coarse for capturing the details of the flow at the edge of the pipe. Still, since aeroacoustic sound generation is not considered in this work, a general estimate of the time-averaged spatial distribution of the flow velocity and temperature is assumed to be sufficient for the calculation of sound propagation in the second step involving computational acoustics. In return, the coarse mesh allows fast CFD calculations.

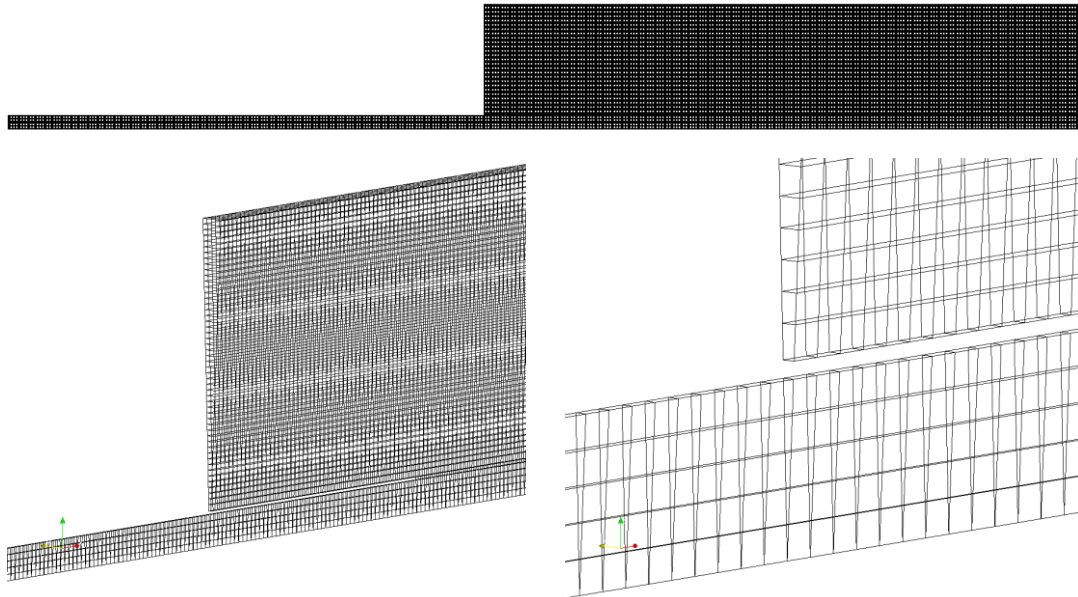


**Figure 6.1:** The CFD mesh: (above) the entire computational domain, (below) the details of the three-dimensional wedge volume elements.

The inlet boundary condition, which is set at the inlet end of the pipe opposite to the opening, allows the specification of the mean flow velocity and temperature values at the central region of the flow, towards the pipe axis. The values inside the boundary layer at the wall of the pipe, which is set to be rigid (motionless), are estimated with the aid of a wall function. Still, due to the rather coarse mesh with only 5 elements within the pipe radius, certain fitting of the inlet values of the mean flow velocity is necessary to agree with the values which were measured at the pipe axis (Chapter III) and, thus, allow better comparison of the obtained acoustic radiation patterns with the measurements. Namely, around 20% lower values of those measured at the axis are used for the uniform boundary conditions at the inlet, which fits well with the data given in the literature for fully developed flows [Rus11]. The estimated Reynolds number with the mean flow speed of 120m/s and the diameter of the pipe as the

characteristic length scale is approximately  $Re \approx 3 \cdot 10^5$ . Normal gradient of pressure at the inlet and at the wall of the pipe is set to zero. In order to maintain the numerical stability close to the wall, the temperature of the wall is set to be equal to the temperature of the jet, which itself matches the measured value.

The outlet conditions at the outer boundaries of the computational domain, as well as the initial conditions in the interior of the domain are given as for motionless air, namely  $p = 101\text{kPa}$ ,  $T = 293\text{K}$ ,  $\rho = 1.2\text{kg/m}^3$ . Dynamic viscosity of a perfect and Newtonian gas, which is a function of temperature, is calculated using Sutherland's law:

$$\mu = \frac{A_s \sqrt{T}}{1 + T_s/T}, \quad (6.1)$$

with constant  $A_s = 1.5 \cdot 10^{-6} \text{ kg}/(\text{msK}^{1/2})$  and Sutherland temperature  $T_s = 116\text{K}$ . Specific heat at constant pressure is considered to be constant,  $c_p = 1005\text{J}/(\text{kgK})$ , and the molecular weight equals  $M = 29\text{g/mol}$ .

Steady-state CFD calculations are performed in three stages:

1. potential flow – estimation of the potential flow which is to be used as the initial conditions for RANS calculations,
2. incompressible RANS of the cold flow, and
3. compressible RANS, including the thermal effects.

The last two calculations are done using the SIMPLE (Semi-Implicit Method for Pressure-Linked Equations) iterative algorithm [FP02], with 500 iterations for the second calculation and 1000 iterations for the third calculation, in order to suppress the effect of the temporal fluctuations of the flow. The eddy-viscosity turbulence model which is used is SST (Shear Stress Transport)  $k-\omega$ , although  $k-\varepsilon$  model has also been tested with small differences in the results. The computations are done in parallel, on a 4-processor workstation and the average total execution time for each set of the mean flow conditions is around 80 seconds.

## 6.1.2 Results

Figure 6.2 shows the mean flow velocity (its dominant axial component) and temperature profiles at the exit of the pipe and in the mixing region of the jet. The results are presented for the maximum value of Mach number at the pipe axis  $M_{max} = 0.25$  and the temperature  $T_{max} = 300^\circ\text{C}$ . The two profiles have almost identical shapes. The mixing region gradually expands from the pipe edge, thus, limiting the potential core region of nearly uniform flow just in front of the pipe opening. The temperature profile also reveals certain diffusion of heat from the wall of the pipe into the cold and still environment, which can be neglected in the acoustic calculations.

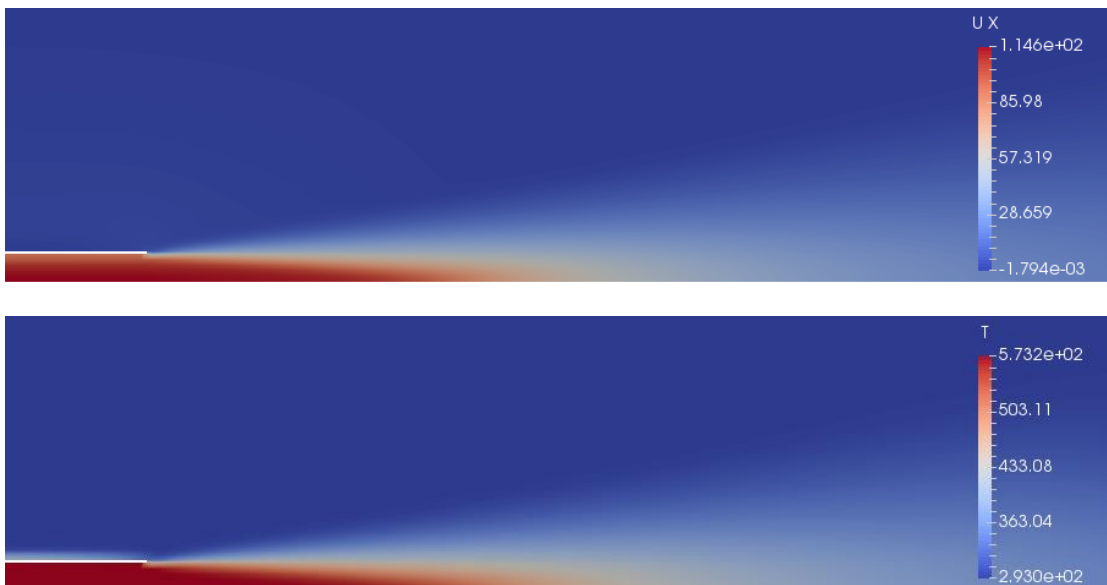


**Figure 6.2:** Mean flow profiles for  $M_{max} = 0.25$  and  $T_{max} = 300^\circ\text{C}$ : (above) axial component of mean flow velocity and (below) temperature in Kelvin degrees.

Figure 6.3 (left) gives a comparison between the axial mean flow velocity calculated at the pipe axis and the values estimated according to Witze [Wit74], where  $x = 0$  lies at the plane of the pipe opening. Due to the too coarse mesh close to the pipe edge, the CFD results do not replicate accurately the size of the potential core of the jet, which corresponds to the initial flat parts of the curves. Similarly, the velocity profile of the fully developed mean flow inside the pipe is captured only roughly, as demonstrated in Figure 6.3 (right). The radial dimension of the elements at the wall of the pipe is only 4mm, which is much larger than the thickness of the turbulent boundary layer.

Nevertheless, the calculations of the mean flow seem to be reasonably accurate for the estimation of sound propagation in the next step, since the spatial decay of the velocity, which is relevant for sound refraction, follows well the curve of Witze. On the other hand, the inaccuracies at the edge of the pipe might reflect on the estimation of sound diffraction and vortex shedding within the acoustic calculations. Therefore, the accuracy of the CFD calculations which is required for the acoustic calculations has to be negotiated in practice, since additional mesh refinement close to the edge inevitably leads to higher computational costs.

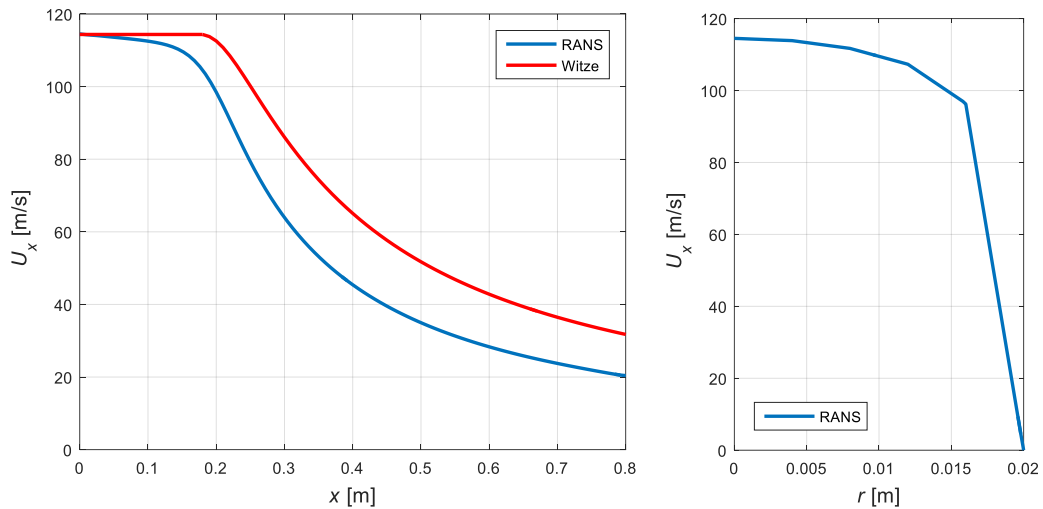


**Figure 6.3:** Axial component of the mean flow velocity: (left) along the axis in front of the pipe opening and compared with [Wit74], (right) inside the pipe, at the axial distance 10cm from the opening.

## 6.2 Computational acoustics

When mean flow properties and all acoustic sources are known, the problem of small-amplitude sound propagation in a moving and inhomogeneous medium can be approached by both solving the system of Linearized Euler Equations or some form of a single-unknown convected wave equation. While the first approach is more accurate, since it is based on the more general approximation of the perturbed flow, the second approach is computationally much more efficient. In the following, both

approaches will be demonstrated and their performances will be compared on the example of sound radiation from a pipe with a sharp trailing edge.

### **6.2.1 Solution of Linearized Euler Equations**

The system of Linearized Euler Equations in the conservative form, the equations (2.95)-(2.97), and in cylindrical coordinates is discretized and solved in time domain. The classical Finite Element Method (FEM), which is commonly used for acoustic calculations, involves globally defined basis and test functions. Consequently, the entire system matrices of the problem have to be inverted during the calculation [HW08], which is frequently computationally the most demanding part of the calculation. Furthermore, the basis functions of FEM are symmetric in space, which makes the method less suitable for problems which involve an asymmetric flow of information, that is, flows which favorize certain directions, such as in convection-dominated problems and conservation laws. The introduction of the so-called upwinding, which addresses this problem, is more natural in the Discontinuous Galerkin Method (DGM) and the Finite Volume Method (FVM). The former one will be used here for the solution of LEE.

Through the calculation of the numerical fluxes at the interfaces between elements, DGM negotiates the discontinuities of the basis functions in a manner similar to FVM. The discontinuities between the elements make the elements mutually independent in time domain calculations and the matrices of DGM truly local. The inversion of such small matrices is computationally much faster compared to the system matrices of FEM. Moreover, the problem-specific numerical fluxes allow greater flexibility in setting up the upwinding scheme, which makes DGM especially favourable for solving conservation laws and the equations based on them. At the same time, higher-order accuracy of the calculations is achievable in the same manner as with FEM and in contrast to the basic FVM. This comes at the price of duplicating the degrees of freedom at all interface nodes between the elements, compared to the classical FEM. However, this difference diminishes with the order of accuracy, since the additional internal nodes in higher-order calculations are not multiplied. In conclusion, DGM scheme is preferred here over FEM for solving the Linearized Euler

Equations in time domain. In contrast to this, a convected wave equation will be solved later using the low-order FEM.

The two-dimensional triangular mesh shown in Figure 6.4 is used for the axisymmetric calculations. Typical dimension of the elements varies between 2mm (which is equal the thickness of the pipe wall) within the extension of the pipe wall, around 1cm inside the pipe (with the inner radius 2cm) and its extension, up to around 8cm far from the edge of the pipe. The adapted mesh takes the advantage of the higher-order DGM and provides higher accuracy in the region of vortical flow, close to the edge. The total length of the pipe is 30cm, while the external propagation region extends 50cm in radial and both axial directions from the pipe opening. The mesh consists of 570 elements with  $(N + 1)(N + 2)/2 = 10$  interior and interface nodes, where  $N = 3$  is the order of accuracy.

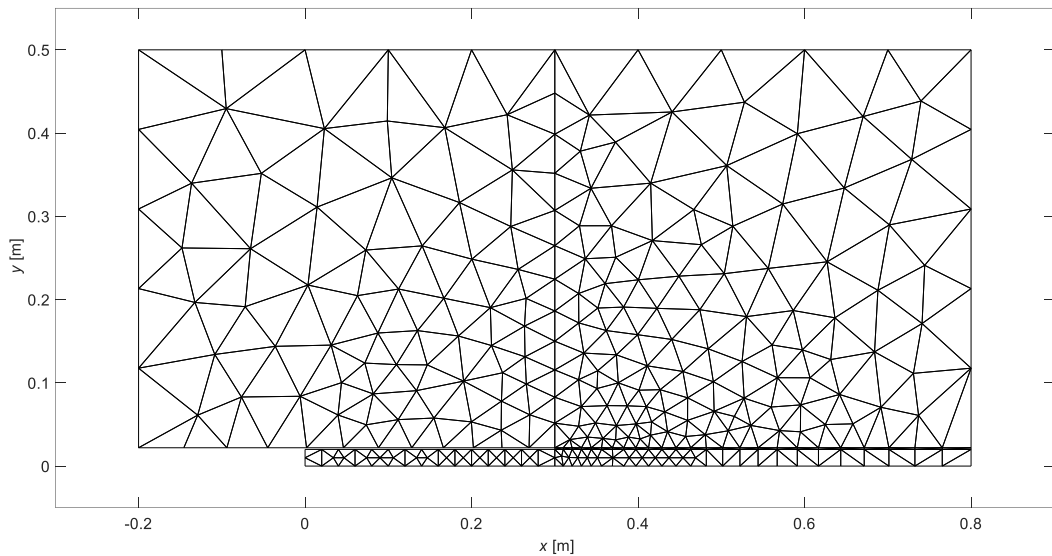


**Figure 6.4:** Mesh used for the solution of Linearized Euler Equations with Discontinuous Galerkin Method.

Source of the plane acoustic wave inside the pipe is introduced with a time varying pressure boundary condition at the upstream end of the pipe. Although a broadband excitation can be applied to simultaneously acquire the radiation patterns at different frequencies, a sine wave is used for simplicity. Assuming constant static pressure

$p_0 = p_\infty \Rightarrow p_{c0} = (p_0/p_\infty)^{1/\gamma} = 1$  and the uniform flow inside the pipe, the boundary conditions at the inlet are:

$$p_c' = p' / (\gamma p_0) = p' / (\rho_J c_J^2) \sim \sin(2\pi f t), \quad (6.2)$$

$$\rho' = p' / c_J^2 = \rho_J p_c', \quad (6.3)$$

$$(\rho v_x)' = \rho_J \frac{p'}{\rho_J c_J} + \frac{p'}{c_J^2} v_{0x} = \frac{p'}{c_J} (1 + M_J) = \rho_J c_J p_c' (1 + M_J), \text{ and} \quad (6.4)$$

$$(\rho v_r)' = 0. \quad (6.5)$$

All other boundary conditions are set to the rigid-wall boundary condition, that is, normal components of the pressure and density gradients equal zero and both axial and radial component of the momentum are zero. The exception is the axial component of the momentum at the pipe axis, which is in general non-zero. Local Lax–Friedrichs flux is applied as the numerical flux at the interfaces between the elements [DIA12], in order to support the discontinuity of the basis functions between the elements. In order to suppress the growing linear instability due to the formation of vortex at the edge, artificial dissipation is added in the form of a two-dimensional exponential filter [HW08], which does not distort noticeably the propagating acoustic wave.

Since no absorbing boundary conditions are applied at the boundaries of the computational domain, the time-domain simulations are interrupted before the first reflections reach the control points where the radiation patterns are estimated. In total 176 equidistant points are set along a semi-circle with the radius 25cm and the centre matching the centre of the pipe opening. The radiation patterns are estimated from the mean square values of the pressure perturbation during one half of the period of the signal which is acquired at each measurement point. The total simulated time is 2.8ms with the time step of around 0.25 $\mu$ s. The computations are done using the Matlab [Mat17] programming language, on a 4-processor workstation. The average total execution time of a single calculation with one set of mean flow data is around 32 minutes, which is around 0.17s per time step. Figure 6.5 shows the spatial distribution of the pressure quantity  $p_c'$  at one time instant and the estimated radiation pattern shape from the same calculation, compared with the measured one.

Mean flow properties are interpolated from the results of the CFD simulations. The maximum Mach number value at the pipe axis equals 0.25 and the temperature is 300°C. Frequency of 1146Hz corresponds to the Helmholtz number  $ka = 0.3$ .

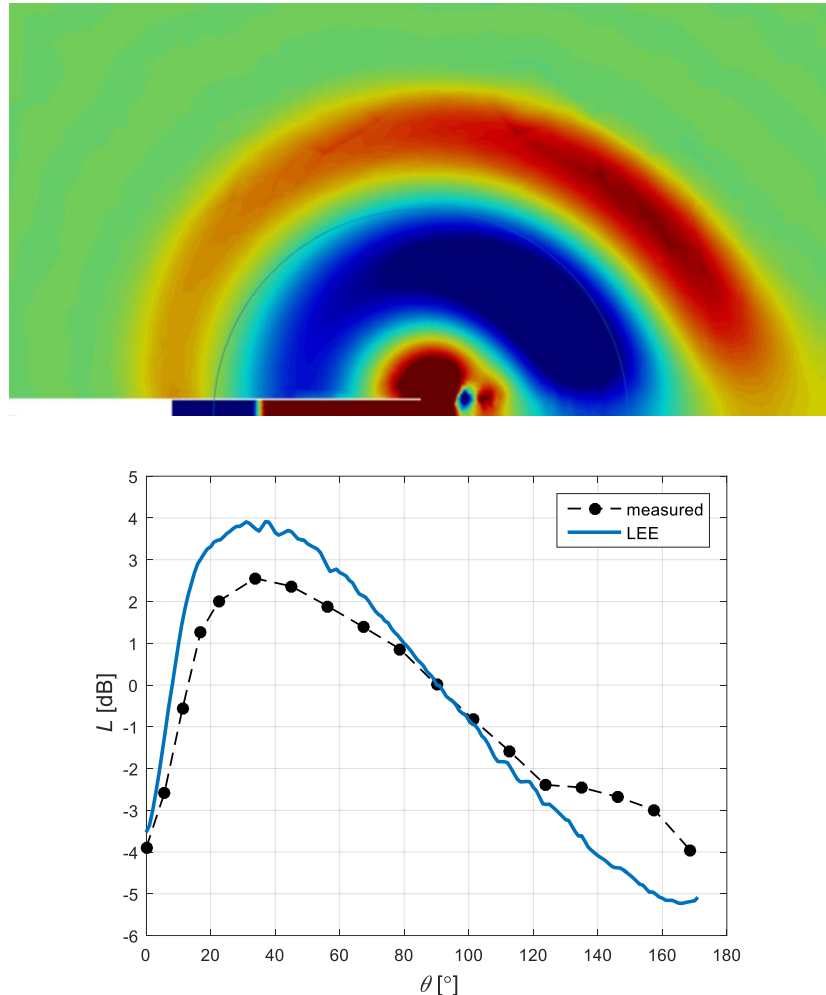


**Figure 6.5:** Solution of Linearized Euler equations: (above) spatial distribution of the pressure perturbation  $p_c'$  at one moment of time and (below) comparison of the estimated and measured radiation patterns; the blue line in the upper diagram connects the points at which the radiation pattern is acquired.

Upper diagram in Figure 6.5 clearly reveals pressure perturbations with small characteristic length scale, which are due to the shed vortices. The vortices are successively generated and convected from the sharp edge of the pipe by the mean flow. Apart from them, the acoustic wave with a large wavelength propagates into the far-field in all directions. The obtained radiation pattern, normalized at the angle  $\theta = 90^\circ$ , shows a fairly good match with the measurement results, with a somewhat

more pronounced directivity. This discrepancy is probably due to the inaccuracy of the mean flow profiles obtained from the CFD calculations. Abrupt changes of the mean flow values in the very thin shear layer at the pipe edge are expected to be sensitive to the coarseness of the mesh. Nevertheless, by the inclusion of vorticity modes, Linearized Euler Equations are capable of capturing accurately the far-field sound radiation from the pipe, although with high computational costs.

### 6.2.2 Solution of convected wave equation

In the following, we will attempt to estimate the far-field radiation pattern of an open pipe with a flow by solving a single convected wave equation, which is in general computationally more efficient than solving a system of coupled equations, such as LEE. Classical convected wave equation (2.110) holds only for a simple uniform mean flow. In order to come up with a form of convected wave equation which allows more complex mean flows, we start with Phillips' equation without mass, force, or heat sources and neglect the effects of viscosity and heat conduction. The flow is then isentropic ( $Ds/Dt = 0$  according to the equation (2.24)) and the equation (2.130) becomes:

$$\frac{D^2 \Pi}{Dt^2} - \nabla \cdot (c^2 \nabla \Pi) = \nabla \cdot (\mathbf{v} \cdot \nabla \mathbf{v}) - \mathbf{v} \cdot \nabla (\nabla \cdot \mathbf{v}), \quad (6.6)$$

with

$$\Pi = \frac{1}{\gamma} \ln \left( \frac{p}{p_\infty} \right). \quad (6.7)$$

Assuming only small unsteady acoustic pressure perturbation  $p'$  around a constant steady value  $p_0 = p_\infty$ , Phillips' equation simplifies to the equation (2.135):

$$\frac{D_0^2 p'}{Dt^2} - \nabla \cdot (c_0^2 \nabla p') = \rho_\infty c_\infty^2 [\nabla \cdot (\mathbf{v} \cdot \nabla \mathbf{v}) - \mathbf{v} \cdot \nabla (\nabla \cdot \mathbf{v})]. \quad (6.8)$$

The same equation also follows from the equation (5.8), which was derived in Chapter 5, everywhere outside the control surface, where the Heaviside function equals 1 and its gradient vanishes. After the expansion of the right-hand side of the equation (6.8):

$$\begin{aligned} & \rho_\infty c_\infty^2 [\nabla \cdot (\mathbf{v} \cdot \nabla \mathbf{v}) - \mathbf{v} \cdot \nabla (\nabla \cdot \mathbf{v})] \\ & = \rho_\infty c_\infty^2 \left[ \nabla \cdot \left( \nabla \frac{\mathbf{v} \cdot \mathbf{v}}{2} + (\nabla \times \mathbf{v}) \times \mathbf{v} \right) - \mathbf{v} \cdot \nabla (\nabla \cdot \mathbf{v}) \right], \end{aligned} \quad (6.9)$$

we again recognize the term  $c_\infty^2 \nabla \cdot [\rho_\infty (\nabla \times \mathbf{v}) \times \mathbf{v}] = c_\infty^2 \nabla \cdot (\rho_\infty \boldsymbol{\omega} \times \mathbf{v})$ , which is the dominant cause of the acoustic sink at the pipe edge for low Mach number flows and low frequencies of the sound. Since this term contains the acoustic velocity, which is part of the sought for solution, its calculation is not straightforward. On the other hand, disregarding it and making the right-hand side of the convected equation equal to zero cancels the effect of the shed vortices and leads to the inaccuracy.

Alternatively, one can attempt to estimate the vorticity term prior to the acoustic calculation in a similar manner as done in Chapter IV. There, we estimated the relation between the monopole and dipole radiation according to the equation (4.15) as:  $p_d' \approx p_m' M_{ac} \cos(\theta)$ . Since the dipole radiation is due to the action of the linearized axial component of the Coriolis force on the pipe edge, where the unsteady pressure perturbation is of essentially incompressible type (solenoidal flow), we can estimate the incompressible pressure at the edge of the pipe from:

$$\frac{\partial p_{ic}'}{\partial x} \approx -\rho_J (\boldsymbol{\omega} \times \mathbf{v})'_x \approx -\frac{\partial}{\partial x} \left( \rho_J \frac{d\Gamma'}{dt} \right) \approx -\frac{\partial}{\partial x} (\rho_J v_J v_{ac}') \quad (6.10)$$

as:

$$p_{ic}' \approx -\rho_J v_J v_{ac}' \approx -\rho_J v_J \frac{2p_{ac}'}{\rho_J c_J} = -2M_J p_{ac}', \quad (6.11)$$

where  $p_{ac}'$  and  $v_{ac}'$  are the acoustic perturbations of pressure and axial velocity component at the pipe opening, respectively, due to the incoming plane sound wave. Here, the approximation  $v_{ac}' \approx 2p_{ac}' / \rho_J c_J$  was used, since the reflection coefficient at the pipe opening is close to -1 at low frequencies and for low Mach numbers, so both incoming and reflecting waves contribute nearly equally to the resulting velocity perturbation. The same relation follows from the equations (4.12) and (4.14) when  $S_\omega = a^2 \pi$ .

The resulting incompressible pressure has the opposite sign of the initial acoustic pressure at the pipe opening. This suggests that in compressible acoustic calculations

(for example, the solution of the equation (6.8) when the pressure perturbation on the left-hand side is assumed to be purely acoustic and, therefore, the right-hand side equal to zero), the sink located at the pipe edge can be modelled with an additional pressure component equal to:

$$p' = (-1 - 2M_J) p_{ac}'. \quad (6.12)$$

In other words, the sink at the computational nodes at the edge cancels the acoustic pressure due to the incoming sound wave and replaces it with the incompressible contribution. The incompressible pressure of the opposite sign results in the force acting on the pipe edge. Since the reaction force of the edge is the cause of the far-field dipole radiation, the positive lobe of the radiation is at the pipe axis downstream. However, such approximation holds only when the amplitude of the incompressible pressure perturbation at the edge is not negligible. Consequently, the model is not appropriate for very low Mach number flows which approach the no-flow case, when the generated vortices are entirely due to the acoustic wave and, therefore, of the second-order. Naturally, no additional constraint regarding the incompressible pressure component should be introduced in such cases.

The equation (6.8) is solved using the first-order Finite Element Method. Compared to the basic Finite Difference Method (FDM), FEM allows greater flexibility in creating the mesh for complex geometries [HW08], which becomes important for more involved engineering applications. The advantage over the Finite Volume Method (FVM), which is still commonly used for computational fluid dynamics, is that it incorporates relatively easily higher-order accuracy even with irregular, unstructured meshes, by increasing the order of the basis functions of the elements and, thus, introducing more degrees of freedom per element. Due to its robustness and computational efficiency, FEM is still the most frequently used scheme in computational mechanics and especially suitable for solving single-unknown wave equations such as the convected wave equation which is solved here.

The two-dimensional mesh which is created for the calculations is very simple. It consists of quadrilateral elements with the dimensions 1cm x 1cm everywhere, except within the extension of the pipe wall, where the dimensions are 0.02cm x 1cm, to match the thickness of the pipe wall, which is 2mm. The length of the pipe is 68cm.

The computational domain extends outside the pipe 50cm in radial and both axial directions from the centre of the pipe opening. As a result, the mesh consists of 5086 elements and 5306 nodes. Small size of the elements compared to the analysed wavelengths justifies the implementation of simple linear basis functions. The time step is 50 $\mu$ s. Rather than a boundary condition at the inlet, the acoustic monopole source is placed at the half-length of the pipe, 1cm from the axis in the radial direction. The excitation signal is a sine wave. Similarly as with the solution of Linearized Euler Equations, all boundaries are treated as rigid walls, with normal component of the pressure gradient equal to zero. The time-domain simulation is interrupted at the time  $t = 2.5$ ms in order to avoid the contribution of the reflections from the outer boundaries of the computational domain. The radiation patterns are estimated from the mean square values of the pressure within one half of the signal's period at the distance 34cm from the opening of the pipe. The computations are implemented using the Matlab programming language and the average computation time on the 4-processor workstation is 30s, that is, around 0.6s per time step. As before, the mean flow properties are interpolated from the results of the CFD RANS simulations.

For each set of the mean flow values, two calculations are executed. In the first calculation, the right-hand side of the equation (6.8) is neglected and, therefore, the effect of the vortex at the pipe edge is suppressed. In the second calculation, the acoustic sink is approximated using the equation (6.12). In the FEM solver, this is achieved with the modification of the entries of the stiffness matrix which refer to the nodes at the pipe edge. This is done in the following way. The matrix equation which corresponds to the equation (6.8) is of the type:

$$\underline{M}\ddot{\underline{p}} + \underline{C}\dot{\underline{p}} + \underline{K}\underline{p} = \underline{f}_\omega, \quad (6.13)$$

where  $\underline{M}$ ,  $\underline{C}$ , and  $\underline{K}$  denote mass, damping, and stiffness matrices, respectively,  $\underline{p}$  is the unknown vector of sound pressure, and  $\underline{f}_\omega$  represents the right-hand side vector due to the vortex (the acoustic sink). Operators  $(\dot{\quad})$  and  $(\ddot{\quad})$  are the first and the second derivative with respect to time, respectively. According to the equation (6.12), vector  $\underline{f}_\omega$  has non-zero values proportional to  $(-1 - 2M_i)p_i$  only for the elements  $i$ , where  $i$  denotes the order number of the calculation nodes which are located at the edge of the

pipe. Since these values depend on the solution vector  $\underline{p}$ , the right-hand side vector has to be shifted to the left-hand side of the equation. Therefore, the vector can be represented as a product of matrix  $\underline{\underline{K}}_\omega$  and vector  $\underline{p}$ :

$$\underline{f}_\omega = \underline{\underline{K}}_\omega \underline{p}, \quad (6.14)$$

where matrix  $\underline{\underline{K}}_\omega$  has all the entries equal to zero, except for the elements  $(i,i)$ , which take the values  $(-1-2M_i)K_{i,i}$  and, therefore, depend only on the local Mach number value for the nodes  $i$ , which are interpolated from the CFD data, and the corresponding entries in the original stiffness matrix  $\underline{\underline{K}}$ . Vector  $\underline{f}_\omega$  can now be shifted to the left-hand side of the matrix equation (6.13) to give:

$$\underline{\underline{M}}\ddot{\underline{p}} + \underline{\underline{C}}\dot{\underline{p}} + (\underline{\underline{K}} - \underline{\underline{K}}_\omega)\underline{p} = 0. \quad (6.15)$$

In practice, the elements  $(i,i)$  of the original stiffness matrix  $\underline{\underline{K}}$  can be simply modified as:  $K_{i,i} = (2 + 2M_i)K_{i,i}$ , to avoid the storage of the additional matrix  $\underline{\underline{K}}_\omega$ .

Figure 6.6 shows the spatial distribution of the pressure perturbation  $p'$  at one moment of time for both calculations – with the right-hand side equal to zero and with the approximated acoustic sink. The maximum Mach number of the flow at the pipe axis is  $M = 0.25$  and the temperature is  $T = 300^\circ\text{C}$ . Frequency of the emitted sound is 1146Hz which gives Helmholtz number value  $ka = 0.3$ .

The estimated radiation patterns are given in Figure 6.7 for the first (blue line) and the second calculation (red line) and for two sets of the mean flow values:

- $M = 0.15, T = 41^\circ\text{C}, ka = 0.5$  and
- $M = 0.25, T = 300^\circ\text{C}, ka = 0.3$ .

In both cases, the results are compared with the measurements after the normalization of the radiation patterns according to the value at the angle  $\theta = 90^\circ$ . Inclusion of the effect of the vortices improves the prediction of the far-field directivity even though a single-unknown convected wave equation is used with the differential operator on the left-hand side which does not support vorticity modes. Hence, the introduced additional condition at the pipe edge can be used for more accurate estimation of sound diffraction at the trailing edge. This becomes more evident in Figure 6.8, when

the radiation pattern shapes are normalized according to the total radiated energy. The implemented approximations provide a good accuracy of the resulting far-field for low Mach number values. The accuracy drops as the mean flow velocity increases. This is expected since the low Mach number assumption is used for the characterization of the acoustic sink, which is based on the Vortex Sound Theory (Chapter IV). The increasing difference can also be associated with the dropped terms from the equation (6.9).

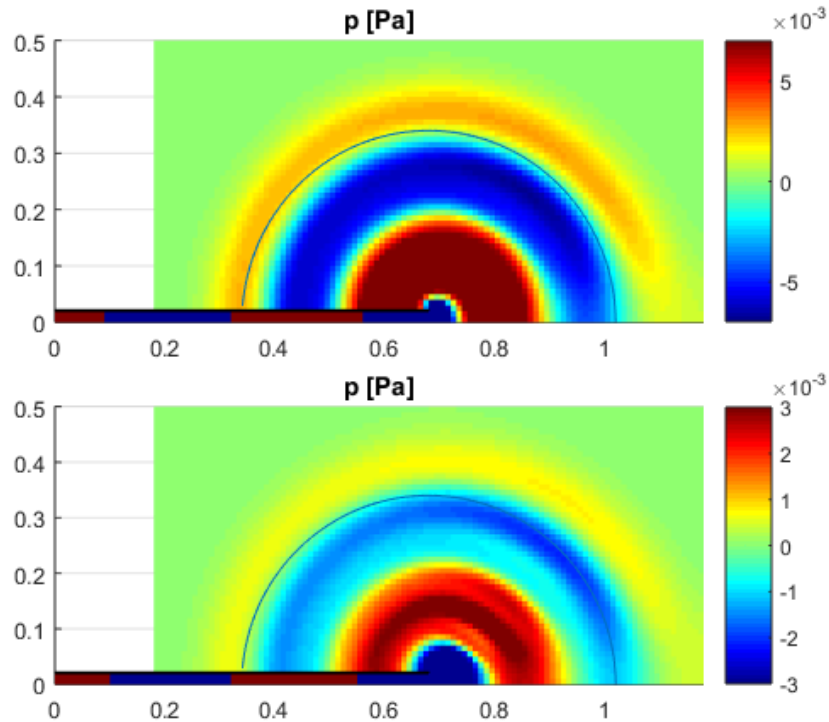


**Figure 6.6:** Spatial distribution of pressure perturbation  $p'$  obtained with solving convected wave equation (6.8) at one moment of time: (above) with neglected effect of the acoustic sink and (below) with the sink approximated using the equation (6.12); the blue lines connect the points at which the radiation pattern is acquired.

Although the obtained results look promising, the approximation of the vortex effect and the associated acoustic sink has some obvious limitations inherited from the Vortex Sound Theory on which it rests. It is expected to fail at higher Mach numbers or Helmholtz numbers. Its application for more complex geometries of the pipe opening, such as the ones of tail-pipes of vehicle exhaust systems or horns of wind instruments, which can lead to a significant increase of the thickness of the shear-layer, should also be further investigated.

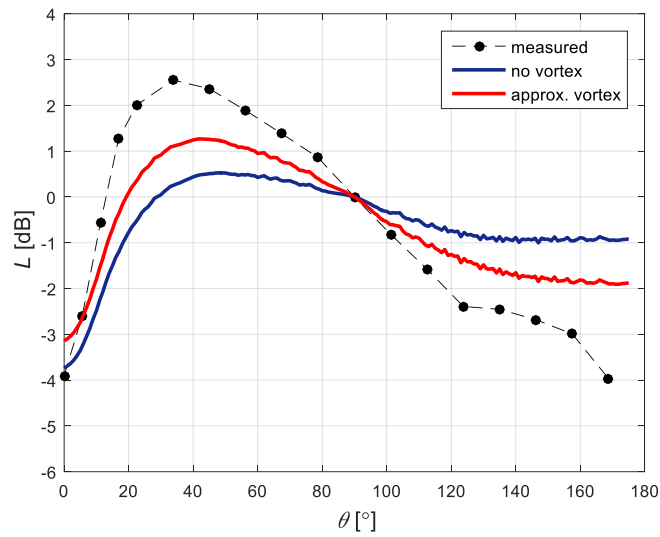
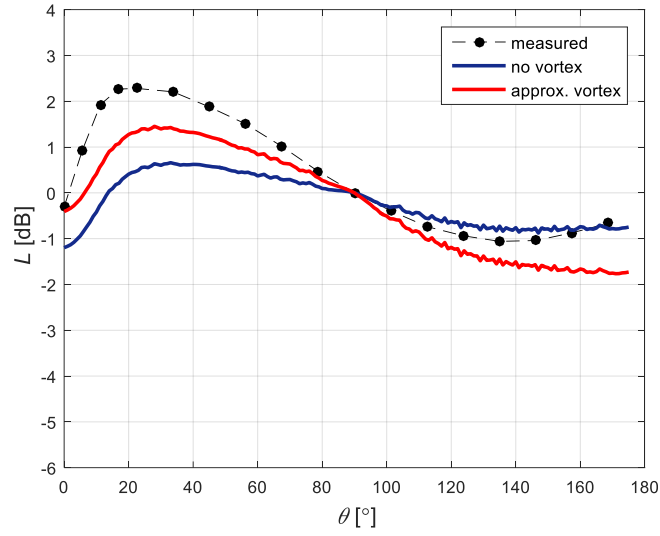


**Figure 6.7:** Estimated and measured shapes of the radiation patterns for: (above)  $M = 0.15$ ,  $T = 41^\circ\text{C}$ ,  $ka = 0.5$  and (below)  $M = 0.25$ ,  $T = 300^\circ\text{C}$ ,  $ka = 0.3$ ; blue lines represent the results with neglected effect of the acoustic sink, red lines represent the results with the sink approximated using the equation (6.12); normalization according to the values at  $\theta = 90^\circ$ .

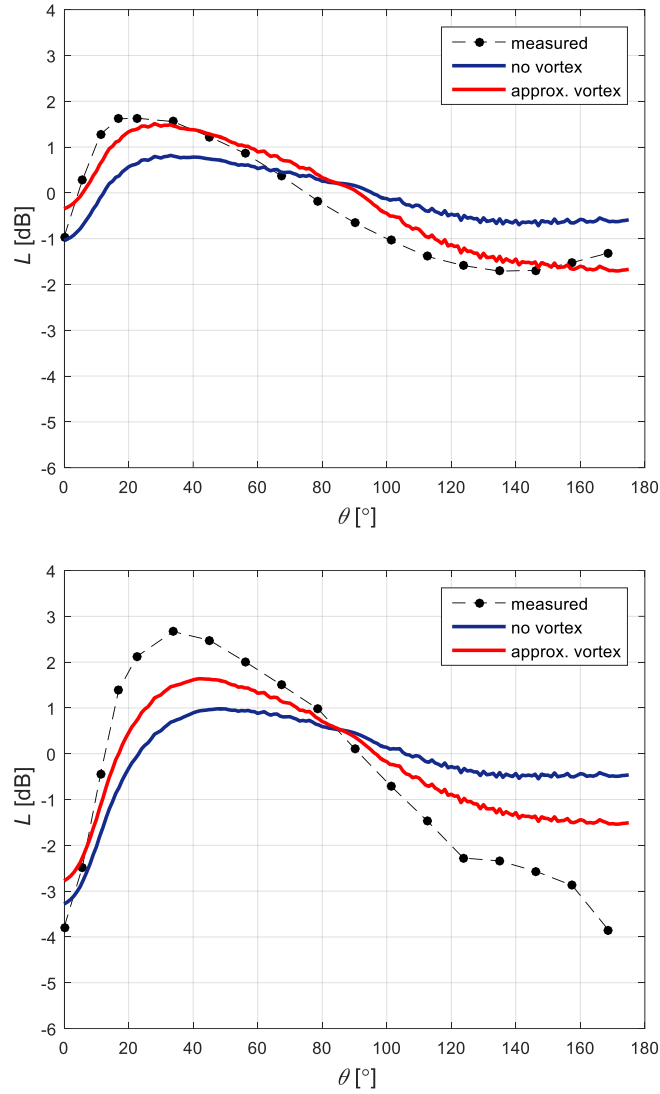


**Figure 6.8:** Estimated and measured shapes of the radiation pattern for: (above)  $M = 0.15$ ,  $T = 41^\circ\text{C}$ ,  $ka = 0.5$  and (below)  $M = 0.25$ ,  $T = 300^\circ\text{C}$ ,  $ka = 0.3$ ; blue lines represent the results with neglected effect of the acoustic sink, red lines represent the results with the sink approximated using the equation (6.12); normalization based on the total radiated energy.



## **Chapter VII**

# **CONCLUSIONS AND OUTLOOK**

The focus of the work was sound propagation outside an open circular pipe with a mean flow at low frequencies. After providing the detailed derivations of some of the main equations of sound propagation in moving and inhomogeneous media, the first major contribution of the work is in the reported results of the laboratory measurements of the far-field radiation patterns. Although certain experimental results can be found in the existing literature, they are most often scattered over many different measurement conditions, possible scenarios, and applications. Especially rare are measurements of the exterior sound field, outside the pipe, in contrast to the measurements of the one-dimensional sound field inside the pipe and the acoustic characterisation of the pipe termination in terms of impedance and reflection coefficient. Chapter III of this work contains results of the systematic measurements of far-field radiation pattern shapes for the case of a low Mach number hot flow and low Helmholtz number sound. The results are then used for the separated analyses of the effects of the mean flow velocity, temperature, and sound frequency on the angular dependence of the far-field sound.

Possible future measurements would greatly benefit from the combination of interior and exterior measurements. The used setup or a similar one can be complemented with the two- or three-microphone wave decomposition technique for capturing the one-dimensional sound field inside the pipe. This would allow not only the estimation of duct-acoustics parameters, such as the radiation impedance at the pipe opening, but also the attenuation of radiated sound energy, which is due to the shed vortices at the trailing edge of the pipe. The latter phenomenon is critical, for example, for the estimation of the efficiency of exhaust systems in suppressing noise coming from the engine of a vehicle. Possible extensions could also include more realistic and application-oriented end-pipes and nozzles, as well as higher frequencies of the radiated sound, especially in the context of musical acoustics.

The goal of the subsequent Chapter IV was to derive a simple semi-empirical model of the far-field radiation based on the Vortex Sound Theory and a rough estimate of the refraction effects. The model provides a means to quickly estimate the directivity of the pipe opening as an apparent sound source in a free field. Equally important, it points to the key flow and acoustic phenomena which govern the far-field sound radiation. Such an insight into the physical phenomena allows one to efficiently predict and possibly control the sound radiation from a pipe exhausting a jet. The discussion in this chapter and the derived conclusions are valid for both analytical and numerical treatment of this type of problems. However, it should be emphasized once again that the used model is established on a simple geometry and based on the assumptions of low Mach number flow, low frequency sound. This might limit its practical use, which should be investigated for every particular application. Still, the problems such as exhaust system tail-pipe noise or low-to-middle frequency sound of simple wind instruments with a straight cut comply with these conditions. Whether the model can be adapted to more complex geometries, such as wind instruments with bells or chambers with sudden expansion, such as in mufflers, should be an object of further research.

Although the primary goal of aeroacoustic analogies is to allow estimation of aerodynamic sources of sound, it is of great importance that they are able to explicitly and accurately capture all the relevant sound propagation phenomena, including the interaction with a solid body in the flow. This becomes critical in inhomogeneous flows and mean flows with non-negligible value of Mach number. With regard to that, an equation which is derived in Chapter V is supposed to include both effects of a moving body and sound propagation in a generally inhomogeneous flows. In order to do so, a combination of well-established Phillips' and Ffowcs Williams and Hawkings equations is used to derive an exact non-linear form of the equation, as well as more practical linearized form. The latter formulation, however, cannot be used for the estimation of essentially non-linear sources of flow-induced noise, such as turbulences. Nevertheless, it is valid for the problem in the focus here, which is dominated by the linear propagation of low-amplitude sound. The equation is able to capture both convection and refraction effects explicitly, rather than inside artificial spatially distributed sources. An open question remains whether the propagation part

(left-hand-side) of the equation can be used in combination with non-linear source terms for aeroacoustic calculations.

Accurate prediction of sound fields in more involved problems which include complicated geometries and flows can be done only with the aid of numerical solvers. If flow-acoustic coupling is weak, as in the case study which is treated here, such that the aeroacoustic sound generation can be neglected, a hybrid approach can be utilized, meaning that the flow and acoustic computations can be performed independently. Furthermore, the results of fast time-averaged mean flow calculations are sufficient as an input for the acoustic calculations. On the other hand, vortex-sound interaction at the trailing edge of the pipe presents a great challenge for the computational acoustics solver. Most of the commonly used acoustic equations, typically second-order wave equations, are not able to capture this interaction and fail in the prediction of the far-field directivity in the presence of a sharp trailing edge. Chapter VI demonstrates the successful solution of Linearized Euler Equations using Discontinuous Galerkin Method. However, the accuracy of the calculations is achieved with large computational costs. Since the critical vortex-sound interaction is limited to the very limited region at the edge of the pipe, an alternative approach is tested, which compensates for the effect of the incompressible flow at the edge within the solution of convected wave equation. The additional constraint on the computational nodes at the edge is derived using the model of Chapter IV and, thus, also based on the Vortex Sound Theory. The first results in terms of the far-field radiation patterns look promising within the limitations of the theory. Still, the physical justification of the applied acoustic sink at the edge, as well as the range of the applications of such an approach for other geometries should be verified in much more details.



## REFERENCES

- [ASG+65] J. Atvars, L. K. Schubert, E. Grande, and H. S. Ribner, “Refraction of sound by jet flow or jet temperature,” UTIAS Technical Note No. 109, 1965.
- [ASL96] E. J. Avital, N. D. Sandham, and K. H. Luo, “Sound generation using data from direct numerical simulations of mixing layers,” 2<sup>nd</sup> AIAA/CEAS Aeroacoustics Conference, State College, Pennsylvania, 1996.
- [Bat02] G. K. Batchelor, *An Introduction to Fluid Dynamics*, pp. 21, 24, 43, 438, Cambridge University Press, 2002.
- [Bec80] D. W. Bechert, “Sound absorption caused by vorticity shedding, demonstrated with a jet flow,” *Journal of Sound and Vibration*, vol. 70, no. 3, pp. 389-405, 1980.
- [BF03] K. S. Brentner and F. Farassat, “Modeling aerodynamically generated sound of helicopter rotors,” *Progress in Aerospace Sciences*, vol. 39, pp. 83-120, 2003.
- [Bie02] J. Bierkens, “Calculation of the reflection coefficient of a jet pipe with subsonic jet flow,” project report, Eindhoven University of Technology, 2002.
- [BN03] S. Boij and B. Nilsson, “Reflection of sound at area expansions in a flow duct,” *Journal of Sound and Vibration*, vol. 260, pp. 477-498, 2003.
- [Bos13] T. Bose, *Aerodynamic Noise – An Introduction for Physicist and Engineers*, pp. 81-82, Springer, New York, 2013.
- [Car82] A. M. Cargill, “Low-frequency sound radiation and generation due to the interaction of unsteady flow with a jet pipe,” *Journal of Fluid Mechanics*, vol. 121, pp. 59-105, 1982.

- [CDF+92] D. G. Crighton, A. P. Dowling, J. E. Ffowcs Williams, M. Heckl, and F. G. Leppington, *Modern Methods in Analytical Acoustics*, pp. 222-232, Springer-Verlag Berlin GmbH, 1992.
- [Cur55] N. Curle, “The influence of solid boundaries upon aerodynamical sound,” in *Proceedings of the Royal Society of London, Series A*, vol. 231, pp. 505-514, 1955.
- [Del14] J. Delfs, *Grundlagen der Aeroakustik (Basics of Aeroacoustics)*, pp. 16, 40-42, 64-72, 103-104, Technische Universität Braunschweig, Braunschweig, 2014.
- [DFW83] A. P. Dowling and J. E. Ffowcs Williams, *Sound and Sources of Sound*, pp. 199-204, Ellis Horwood Limited, Chichester, 1983.
- [DIA12] R. Della Ratta Rinaldi, A. Iob, and R. Arina, “An efficient Discontinuous Galerkin Method for aeroacoustic propagation,” *International Journal for Numerical Methods in Fluids*, vol. 69, pp. 1473–1495, 2012.
- [Doa72] P. E. Doak, “Analysis of internally generated sound in continuous materials: 2. A critical review of the conceptual adequacy and physical scope of existing theories of aerodynamic noise, with special reference to supersonic jet noise,” *Journal of Sound and Vibration*, vol. 25, no. 2, pp. 263-335, 1972.
- [ES03] R. Ewert and W. Schröder, “Acoustic perturbation equations based on flow decomposition via source filtering,” *Journal of Computational Physics*, vol. 188, pp. 365-398, 2003.
- [FH69] J.E. Ffowcs Williams and D. L. Hawkings, “Sound generation by turbulence and surfaces in arbitrary motion,” *Philosophical Transactions of the Royal Society of London, Series A*, vol. 264, pp. 321-342, 1969.
- [FP02] J. H. Ferziger and M. Peric, *Computational Methods for Fluid Dynamics*, 3<sup>rd</sup> edition, pp. 36, 175-176, 293, Springer-Verlag Berlin, 2002.

- [Gol76] M. E. Goldstein, *Aeroacoustics*, pp. 253, McGraw-Hill Inc., New York, 1976.
- [Ham16] K. Hamiche, *A High-Order Finite Element Model for Acoustic Propagation*, thesis, University of Southampton, 2016.
- [HGB16] K. Hamiche, G. Gabard, and H. Bériot, “A high-order Finite Element Method for the Linearised Euler Equations,” *Acta Acustica United with Acustica*, vol. 102, pp. 813-823, 2016.
- [HH14] A. Hirschberg and M. Hoeijmakers, “Comments on the low frequency radiation impedance of a duct exhausting a hot gas,” *Journal of the Acoustical Society of America – Express Letters*, vol. 136, no. 2, pp. EL84-EL89, 2014.
- [How79] M. S. Howe, “Attenuation of sound in a low Mach number nozzle flow,” *Journal of Fluid Mechanics*, vol. 91, no. 2, pp. 209-229, 1979.
- [How98] M. S. Howe, *Acoustics of Fluid-Structure Interactions*, pp. 93, 120, 174, 337-338, Cambridge University Press, 1998.
- [HRD11] M. Hornikx, W. De Roeck, and W. Desmet, “Flow and geometrical effects on radiated noise from exhausts computed by a hybrid extended Fourier PSTD method,” *17<sup>th</sup> AIAA/CEAS Aeroacoustics Conference (32<sup>nd</sup> AIAA Aeroacoustics Conference)*, Portland, Oregon, June 5-8, 2011, AIAA Paper No. 2011-2844.
- [HW08] J. S. Hesthaven and T. Warburton, *Nodal Discontinuous Galerkin Methods – Algorithms, Analysis, and Applications*, pp. 1-10, 186-187, Springer Science+Business Media, LLC, New York, 2008.
- [IKP06] M. Ihme, M. Kaltenbacher, and H. Pitsch, “Numerical simulation of flow- and combustion-induced sound using a hybrid LES/CAA approach,” *Proceedings of the Summer Program 2006*, Stanford, 2006.
- [Kut07] H. Kuttruff, *Acoustics – An introduction*, pp. 121-123, Taylor & Francis, Oxon, 2007.
- [Lig52] M. J. Lighthill, “On sound generated aerodynamically, I. General theory,” in *Proceedings of the Royal Society of London, Series A*, vol. 211, pp. 564-586, 1952.

- [Lil74] G. M. Lilley, “On the noise from jets. Noise mechanisms,” *AGARD-CP-131*, 13.1-13.12 (1974).
- [Loc00] D. P. Lockard, “An efficient, two-dimensional implementation of the Ffowcs Williams and Hawkings equation,” *Journal of Sound and Vibration*, vol. 229, no. 4, pp. 897-911, 2000.
- [LS48] H. Levine and J. Schwinger, “On the radiation of sound from an unflanged circular pipe,” *Physical Review*, vol. 73, no. 4, pp. 383-406, 1948.
- [Lus71] P. A. Lush, “Measurements of subsonic jet noise and comparison with theory,” *Journal of Fluid Mechanics*, vol. 46, part 3, pp. 477-500, 1971.
- [Mas16] D. Masovic, “Comments on convective amplification of sound sources in flows,” *ASRO Journal of Applied Mechanics*, vol. 1, no. 1, pp. 20-23, 2016.
- [Mat17] Matlab <https://de.mathworks.com/products/matlab.html>
- [MDR07] C.-D. Munz, M. Dumbser, and S. Roller, “Linearized acoustic perturbation equations for low Mach number flow with variable density and temperature,” *Journal of Computational Physics*, vol. 224, pp. 352-364, 2007.
- [Mey09] J. Meyer, *Acoustics and the performance of music*, 5<sup>th</sup> edition, pp. 133-148, Springer Science+Business Media, LLC, New York, 2009.
- [MNR+17a] D. Masovic, E. Nijman, J. Rejlek, and R. Höldrich, “A simple model of the far-field directivity of an open circular pipe with a hot flow,” in *Proceedings of DAGA 2017*, Kiel, pp. 1222-1225, 2017.
- [MNR+17b] D. Masovic, E. Nijman, J. Rejlek, and R. Höldrich, “Towards a boundary condition for convective wave equation and sound diffraction at a trailing edge inside a flow,” in *Proceedings of DAGA 2017*, Kiel, pp. 1301-1304, 2017.
- [Moo77] C. J. Moore, “The role of shear-layer instability waves in jet exhaust noise,” *Journal of Fluid Mechanics*, vol. 83, no. 4, pp. 609-640, 1977.

- [Mun77] R. M. Munt, “The interaction of sound with a subsonic jet issuing from a semi-infinite cylindrical pipe,” *Journal of Fluid Mechanics*, vol. 83, no. 4, pp. 609-640, 1977.
- [Mun90] R. M. Munt, “Acoustic transmission properties of a jet pipe with subsonic jet flow: I. The cold jet reflection coefficient,” *Journal of Sound and Vibration*, vol. 142, no. 3, pp. 413-436, 1990.
- [Mus07] R. E. Musafir, “On the source terms in Lilley’s equation,” *Acta Acustica united with Acustica*, vol. 93, pp. 263-274, 2007.
- [MZN+16] D. Masovic, F. Zotter, E. Nijman, J. Rejlek, and R. Höldrich, “Directivity measurements of low frequency sound field radiated from an open cylindrical pipe with a hot mean flow,” *9<sup>th</sup> ISNVH Congress*, Graz, Austria, June 22-24, 2016, SAE Technical Paper 2016-01-1822, 2016.
- [Ope17] OpenFOAM <http://openfoam.org/>
- [OW16] V. E. Ostashev and D. Keith Wilson, *Acoustics in Moving Inhomogeneous Media*, 2<sup>nd</sup> edition, pp. 6-7, CRC Press, Boca Raton, FL, 2016.
- [PB76] R. A. Pinker and W. D. Bryce, “The radiation of plane-wave duct noise from a jet exhaust, statically and in flight,” *3<sup>rd</sup> AIAA Aero-Acoustics Conference*, Palo Alto, California, July 20-23, 1976, AIAA Paper No. 76-581.
- [Phi60] O. M. Phillips, “On the generation of sound by supersonic turbulent shear layers,” *Journal of Fluid Mechanics*, vol. 9, pp. 1-28, 1960.
- [PHR+93] M. C. A. M. Peters, A. Hirschberg, A. J. Reijnen, and A. P. J. Wijnands, “Damping and reflection coefficient measurements for an open pipe at low Mach and low Helmholtz numbers,” *Journal of Fluid Mechanics*, vol. 256, pp. 499-534, 1993.
- [PKJ+11] A. Pradera-Mallabiarrena, G. Keith, F. Jacobsen, A. Rivas, and N. Gil-Negrete, “Practical computational aeroacoustics for compact surfaces in low Mach number flows,” *Acta Acustica united with Acustica*, vol. 97, pp. 14-23, 2011.

- [Pow60] A. Powell, "Aerodynamic noise and the plane boundary," *Journal of the Acoustical Society of America*, vol. 32, no. 8, pp. 982-990, 1960.
- [Pow64] A. Powell, "Theory of vortex sound," *Journal of the Acoustical Society of America*, vol. 36, no. 1, pp. 177-195, 1964.
- [Pur17] Pure Data <https://puredata.info/>
- [Ray78] J. W. S. Rayleigh, *The theory of sound*, Vol. II, Macmillan and Co., London, 1878.
- [Rey95] O. Reynolds, "On the dynamical theory of incompressible viscous fluids and the determination of the criterion," *Philosophical Transactions of the Royal Society of London, Series A*, vol. 186, pp. 123-164, 1895.
- [RH16] S. W. Rienstra and A. Hirschberg, *An Introduction to Acoustics*, pp. 2, 50-52, 216, Eindhoven University of Technology, 2016
- [Rib96] H. S. Ribner, "Effects of jet flow on jet noise via an extension to the Lighthill model," *Journal of Fluid Mechanics*, vol. 321, pp. 1-24, 1996.
- [Rie83] S. W. Rienstra, "A small Strouhal number analysis for acoustic wave-jet flow-pipe interaction," *Journal of Sound and Vibration*, vol. 86, no. 4, pp. 539-556, 1983.
- [Roe07] W. De Roeck, *Hybrid Methodologies for the Computational Aeroacoustic Analysis of Confined, Subsonic Flows*, pp. 240-242, Katholieke Universiteit Leuven, Leuven, 2007.
- [RRV14] M. P. Rumpfkeil, D. K. Robertson, and M. R. Visbal, "Comparison of aerodynamic noise propagation techniques," *52<sup>nd</sup> Aerospace Sciences Meeting, AIAA SciTech*, AIAA 2014-0021, National Harbor, Maryland, 2014.
- [Rus11] G. P. Russo, *Aerodynamic Measurements, From Physical Principles to Turnkey Instrumentation*, pp. 58, Woodhead Publishing Limited, Cambridge, UK, 2011.

- [SSS13] Y. Shi, A. da Silva, and G. Scavone G, “Numerical analysis of the mean flow effect on the sound directivity pattern of cylindrical ducts,” in Proceedings of SMAC 2013, Stockholm, July 30 – August 3, 2013, pp. 458-464.
- [TLR+14] H. Tiikoja, J. Lavrentjev, H. Rämmal, and M. Åbom, “Experimental investigations of sound reflection from hot and subsonic flow duct termination,” *Journal of Sound and Vibration*, vol. 333, no. 3, pp. 788-800, 2014.
- [Wal01] D. C. Van Der Walt, “Measurement technique to assess the acoustic properties of a silencer component for transient engine conditions,” *Journal of Sound and Vibration*, vol. 243, no. 5, pp. 797-821, 2001.
- [WGW+10] C. Weckmüller, S. Guérin, J. Wellner, and U. Michel, “Ffowcs Williams & Hawkings formulation for the convective wave equation and permeable data surface,” *16<sup>th</sup> AIAA/CEAS-Aeroacoustics Conference*, Stockholm, Sweden, 2010.
- [WH95] V. L. Wells and A. Y. Han, “Acoustics of a moving source in a moving medium with application to propeller noise,” *Journal of Sound and Vibration*, vol. 184, no. 4, pp. 651-663, 1995.
- [Wit74] P. O. Witze, “Centerline velocity decay of compressible free jets,” *AIAA Journal*, vol. 12, no. 4, pp. 417-418, 1974.





Institute of Electronic Music and Acoustics  
University of Music and Performing Arts Graz